

**PIEZOCATALYTIC AND PIEZOELECTRIC  
PROPERTIES OF P(VDF) AND ITS  
COPOLYMER/TERPOLYMER FILMS**

**A Thesis Submitted to  
the Graduate School of Engineering and Sciences of  
İzmir Institute of Technology  
in Partial Fulfillment of the Requirements for the Degree of  
MASTER OF SCIENCE  
in Materials Science and Engineering**

**by  
Ceren TENGİZDENİZ**

**July 2023  
İZMİR**

We approve the thesis of **Ceren TENGİZDENİZ**.

Examining Committee Members:

**Assoc. Prof. Dr. Umut ADEM**

Department of Materials Science and Engineering/ İzmir Institute of Technology

**Assoc. Prof. Dr. Aylin ALBAYRAK**

Department Of Metallurgy and Materials Engineering / Dokuz Eylül University

**Prof. Dr. Mustafa Muammer DEMİR**

Department of Materials Science and Engineering/ İzmir Institute of Technology

**18/07/2023**

**Assoc. Prof. Dr. Umut ADEM**

Supervisor, Materials Science  
and Engineering Department/  
İzmir Institute of Technology

**Assoc. Prof. Dr. Aziz GENÇ**

Co-Supervisor, Materials  
Science and Engineering  
Department / İzmir  
Institute of Technology

**Prof. Dr. Sedat AKKURT**

Head of Materials Science  
and Engineering Department

**Prof. Dr. Mehtap EANES**

Dean of the Graduate  
School of Engineering and  
Sciences

## ACKNOWLEDGEMENT

First of all, I would like to thank my thesis advisor, Assoc. Prof. Dr. Umut ADEM, for sharing his valuable experiences, guidance, and endless support, also for his motivation throughout my thesis study with his sincerity and kindness.

I would also like to thank Aziz Genç for sharing his guidance and endless support, and also his laboratory with us during piezocatalytic measurements. In addition, I would like to thank IZTECH Materials Research Center and special thanks to Mutlu Devran Yaman for his support and assistance throughout the SEM analysis.

I'd like to thank Tuğçe Irmak and Research Assistant Dr. Merve Günnar Karakaya for their valuable support and dedicating their precious time. I would like to thank them for the information they have taught me and the advice they have given me. Also, I'd like to thank my laboratory friend Simay Dindar for her support during thesis experiments and measurements.

My family is the foundation of my personality and morality. My special thanks go to my family. I would like to thank my mother Ebru Tengizdeniz, my father Mustafa Tengizdeniz, my sister Cemre Naz Tengizdeniz, and my better half, love and soul mate Okan Gökalp. The biggest reason why I have come to these days successfully and with high motivation is that these 4 people are always by my side. I would like to thank them for their valuable support and for always being behind me.

# ABSTRACT

## PIEZOCATALYTIC AND PIEZOELECTRIC PROPERTIES OF P(VDF) AND ITS COPOLYMER/TERPOLYMER FILMS

Nowadays, the release of colored organic pollutants such as Rhodamin B dye, resulting from industrial activities endanger the people, animals, and plants. Many methods have developed to destroy these harmful pollutants. Piezocatalysis, a newly used environmentally friendly method, takes advantage of the piezoelectric effect, and uses mechanical vibration to produce active species on opposite surfaces of matter for degradation of dye. In this study, piezocatalytic and piezoelectric properties of P(VDF) based homopolymer, copolymer and terpolymers were investigated. With the addition of 2<sup>nd</sup> and 3<sup>rd</sup> monomer to the homopolymer, observation of change in piezoelectric and piezocatalytic properties and removal efficiency of pollution in water, were aimed. P(VDF) homopolymer, P(VDF-TrFE) copolymers with composition of 55/45 and 50/50 mol%, and P(VDF-TrFE-CTFE) terpolymer with 62/31/7 mol% were synthesized by solution casting method.

It was observed that the 2<sup>nd</sup> and 3<sup>rd</sup> monomer added to the homopolymer enhanced the piezoelectric properties and strain characteristics of the polymers. Maximum polarization and strain of terpolymer was observed as 11  $\mu\text{C}/\text{cm}^2$  and 5.6 %, respectively. Due to the increase in piezoelectricity, a noticeable increase in piezocatalytic properties was observed. Terpolymer exhibited the highest and most efficient piezoelectric and piezocatalytic performance. P(VDF) homopolymer was reached 27% dye degradation efficiency. While copolymers with mol% 55/45 and 50/50, dye degradation efficiencies were 40% and 47%, respectively, terpolymer efficiency was 54%. From the dielectric measurements, within the transition region ( $49 \text{ mol}\% \leq C_{\text{VDF}} \leq 55 \text{ mol}\%$ ) of P(VDF-TrFE), both normal-ferroelectric and relaxor characteristics were observed. Terpolymer showed relaxor properties as expected.

## ÖZET

### P(VDF)'İN VE KOPOLİMER/TERPOLİMER FİLMLERİNİN PIEZOKATALİTİK VE PIEZOELEKTRİK ÖZELLİKLERİ

Son zamanlarda, endüstriyel faaliyetlerden kaynaklanan Rodamin B boyar maddesi gibi renkli organik kirleticilerin salınımı, canlılar için bir tehlike oluşturmaktadır. Bu zararlı kirleticileri yok etmek için birçok yöntem geliştirilmiştir. Yeni kullanılmaya başlanan ve çevre dostu bir yöntem olan piezokataliz, piezoelektrik etkiden yararlanır ve boyanın bozunması için maddenin zıt yüzeylerinde aktif türler üretmek için mekanik titreşim kullanır. Bu çalışmada P(VDF) bazlı homopolimer, kopolimer ve terpolimerlerin piezokatalitik ve piezoelektrik özellikleri incelenmiştir. Homopolimere 2. ve 3. monomer eklenerek, piezoelektrik ve piezokatalitik özelliklerdeki değişimin ve sudaki kirliliği giderme etkinliğinin gözlenmesi amaçlanmıştır. P(VDF) homopolimer, molce %55/45 ve %50/50 bileşimine sahip P(VDF-TrFE) kopolimer ve molce %62/31/7 bileşimine sahip P(VDF-TrFE-CTFE) terpolimer, solüsyon döküm yöntemi ile sentezlenmiştir.

Homopolimere eklenen 2. ve 3. monomerin, polimerlerin piezoelektrik özelliklerini ve gerinim özelliklerini arttırdığı gözlenmiştir. Böylece terpolimerin maksimum polarizasyonu  $11 \mu\text{C}/\text{cm}^2$ , gerilimi %5.6 olarak ölçülmüştür. Piezoelektrik özellikteki artış ile piezokatalitik özelliklerde de gözle görülür bir gelişim meydana gelmiştir. Terpolimer, en yüksek ve en verimli piezoelektrik ve piezokatalitik performansı sergilemiştir. P(VDF) homopolimerinde %27 boya bozunma verimine ulaşılmıştır. Molce %55/45 ve 50/50 olan kopolimerlerin boya bozunma verimleri sırasıyla %40 ve %47 iken, terpolimerin bozunma verimi %54 olmuştur. Ayrıca dielektrik ölçümlerinden, P(VDF-TrFE)'nin geçiş bölgesinde (molce  $\%49 \leq \text{CVDF} \leq \%55$ ) içinde hem normal-ferroelektrik hem de relaxör ferroelektrik özellikler gözlenmiştir. Terpolimer beklendiği gibi relaxör özellikler göstermiştir.

# TABLE OF CONTENTS

LIST OF FIGURES.....	vii
LIST OF TABLES .....	ix
CHAPTER 1.INTRODUCTION .....	1
1.1. Piezoelectricity .....	1
1.2. Piezoelectric Materials, Polymers and Their Applications.....	5
1.3. PVDF Polymers and Their Properties .....	8
1.4. Copolymer and Terpolymer of PVDF .....	11
1.5. Piezocatalytic Property and Mechanisms .....	15
1.6. Literature Review .....	23
1.7. Research Objectives.....	28
CHAPTER 2.EXPERIMENTAL.....	30
2.1. Fabrication of Polymer Thick Films.....	30
2.2. Characterization of Materials .....	32
CHAPTER 3.RESULTS AND DISCUSSION .....	38
3.1. X-Ray Diffraction (XRD) of Polymer Films.....	38
3.2. Scanning Electron Microscopy (SEM) of Polymer Films.....	41
3.3. Differential Scanning Calorimetry (DSC) of Polymer Films.....	44
3.4. Dielectric Properties of Polymer Films .....	46
3.5. Ferroelectric and Piezoelectric Properties of Polymer Films .....	51
3.6. Strain Characteristics of Polymer Films.....	54
3.7. Piezocatalytic Properties of Polymer Films.....	56
3.8. Discussion of Results.....	61
CHAPTER 4.CONCLUSION .....	63
REFERENCES .....	65

# LIST OF FIGURES

<b><u>Figure</u></b>	<b><u>Page</u></b>
Figure 1.1. Classification according to point group symmetry.....	1
Figure 1.2. Relationship between piezoelectric, pyroelectric and ferroelectric materials.	2
Figure 1.3. Hysteresis loop and domain switching.....	3
Figure 1.4. External force acting on a crystal a) with/ b) without inversion symmetry ...	3
Figure 1.5. Schematic representation of direct/converse piezoelectric effect .....	4
Figure 1.6. Main phases of polyvinylidene fluoride (PVDF) .....	8
Figure 1.7. Processes used experimentally to produce the different PVDF phases.....	9
Figure 1.8. Publications (1980-2022) containing the keywords.....	11
Figure 1.9. P(VDF-TrFE) phase diagram .....	12
Figure 1.10. Structure of VDF-TrFE .....	12
Figure 1.11. Hysteresis loops/ domains for ferroelectric and dielectric materials .....	14
Figure 1.12. The absorbance ratio of dye with time for 3 kinds of catalysis type.....	16
Figure 1.13. Charge carriers arising from mechanical excitation or material defects ....	19
Figure 1.14. Material band structure and redox potentials of ROS generation .....	19
Figure 1.15. Principle of piezocatalysis based on the screening charge effect.....	20
Figure 1.16. Mechanism of the piezocatalytic degradation .....	23
Figure 1.17. Piezocatalytic dye degradation performance (C/Co-t) for composites .....	24
Figure 1.18. UV-visible spectrums of 5 and 10 wt. % BCZTO/PVDF composites .....	25
Figure 1.19. Piezocatalytic degradation curves for polymer/ceramic composites .....	26
Figure 1.20. Piezocatalytic performances of PVDF, LN-PVDF and Ag/LN-PVDF.....	27
Figure 1.21. Piezocatalytic degradation w/ultrasonic vibration with of BaTiO <sub>3</sub> .....	28
Figure 2.1. Diagram of synthesis method used for polymer films .....	30
Figure 2.2. Polymer sample with silver paste for electrical measurements.....	33

<b><u>Figure</u></b>	<b><u>Page</u></b>
Figure 2.3. Phase difference between the applied voltage and the resulting current.....	34
Figure 2.4. Experimental water circulation set-up for the sonicator. ....	37
Figure 3.1. X-ray diffraction patterns of homopolymer, copolymers and terpolymer. ..	39
Figure 3.2. X-ray diffraction patterns of polymer films between 15-25°. ....	40
Figure 3.3. $\beta$ -phase intensities at different annealing temperatures for copolymers. ....	41
Figure 3.4. SEM images of homopolymer PVDF. ....	42
Figure 3.5. SEM images of terpolymer P(VDF-TrFE-CTFE) (61/32/7). ....	42
Figure 3.6. SEM images of copolymer P(VDF-TrFE) (55/45). ....	43
Figure 3.7. SEM images of copolymer P(VDF-TrFE) (50/50). ....	43
Figure 3.8. Cross section SEM images of polymer films ....	43
Figure 3.9. The DSC heating curves of homopolymer, terpolymer and copolymers ....	46
Figure 3.10. Relaxor ferroelectricity and ferroelectricity with VDF content ....	47
Figure 3.11. Dielectric constant- temperature at different frequencies for polymers. ....	49
Figure 3.12. Dielectric constant for polymers at 10 kHz. ....	50
Figure 3.13. Dielectric loss versus temperature graphs for synthesized polymers. ....	50
Figure 3.14. Hysteresis loops (P-E) for homopolymer, terpolymer and copolymers ....	51
Figure 3.15. Terpolymer hysteresis loops at 90 Hz (3 kV and 4.5 kV electric fields) ...	53
Figure 3.16. Terpolymer hysteresis loops at 3 kV, (10 Hz and 90 Hz) ....	53
Figure 3.17. Strain characteristics of homopolymer, terpolymer and copolymers. ....	55
Figure 3.18. Dye degradation performance (%) of polymers. ....	56
Figure 3.19. Piezocatalytic dye degradation kinetic rate and rate constants. ....	57
Figure 3.20. Absorbance-wavelength graphs of RhB solutions at 105 min. ....	58
Figure 3.21. Absorbance versus wavelength graphs of RhB solutions. ....	59

# LIST OF TABLES

<b><u>Table</u></b>	<b><u>Page</u></b>
Table 1.1. Examples of piezoelectric material categories.....	5
Table 1.2. Piezoelectric materials for engineering applications .....	6
Table 1.3. Physical and electrical properties of PVDF polymers.....	15
Table 1.4. Difference between energy band theory and screening charge effect .....	21
Table 3.1. Approximate estimated crystallinity percentage for each polymer .....	45
Table 3.2. Piezocatalytic performance for different materials from literature. ....	60

# CHAPTER 1

## INTRODUCTION

This section provides information on piezoelectricity, piezoelectric polymers, and their applications, and piezocatalytic property.

### 1.1. Piezoelectricity

A class of materials with the interesting property of directly converting electrical and mechanical energy into one another is said to exhibit piezoelectric property. The piezoelectric property was first discovered in 1880 by the famous French physicist Curie brothers, but the rapid increase in existing products developing in this market was noticed a century later. Its name is taken from the *piezo* which is Greek word, is used frequently in science to refer to mechanical stress, such as pressure <sup>1,2</sup>.

For the piezoelectricity to occur, a crystal must meet certain conditions. These type of crystals are non-centro-symmetric crystals. 21 of the 32 crystallographic point groups are non-centrosymmetric. 20 point groups exhibit piezoelectricity (except 432 point group). The 10 polar (polar materials do not have inversion symmetry) and 10 non-polar piezoelectric point groups can be further subdivided. Pyroelectrics are polar. Pyroelectrics which exhibit reversible polarization are called ferroelectric. This classification can be seen in Figure 1.1 below.

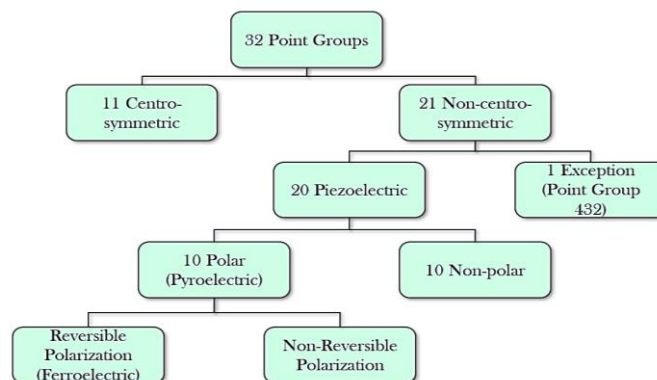


Figure 1.1. Classification according to point group symmetry <sup>1</sup>

The relationship between piezoelectric, pyroelectric and ferroelectric materials is shown schematically in the Figure 1.2 below. Dielectric materials can be polarized under the influence of an electric field, and they are electrical insulators. Piezoelectrics, on the other hand, are a group of dielectrics that exhibit strain or stress change when an external electric field is applied, or, conversely, a change in polarization with mechanical excitation. A sub-class of piezoelectrics known as pyroelectrics can exhibit a change in polarization in response to a change in temperature. Ferroelectric materials have both piezo- and pyroelectric properties, and their outstanding character is the reversibility of the permanent polarization under the influence of electric field.

Hysteresis loop and domain switching shown in Figure 1.3 below, are the terms used to describe this phenomenon. Domains are the crystal regions with uniformly oriented spontaneous polarization<sup>3</sup>. There are important terms to understand this process: remanent polarization, coercive field and saturation polarization. The remanent polarization, or  $P_r$ , is the polarization value at the zero field (point E). The coercive field, or  $E_c$ , is the field required for depolarizing the material to zero polarization. The maximum polarization that can be achieved is saturation polarization,  $P_{sat}$ <sup>4</sup>. The situation where the polarization direction of all domains is the same as the electric field is called saturation polarization.

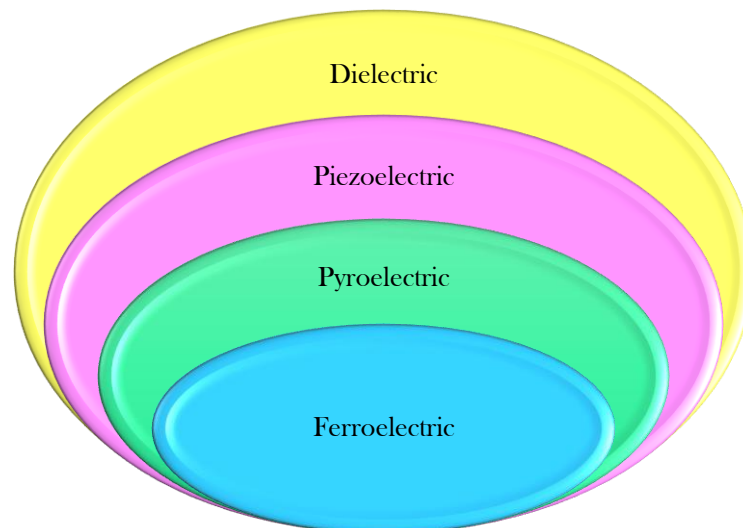


Figure 1.2. Relationship between piezoelectric, pyroelectric and ferroelectric materials.

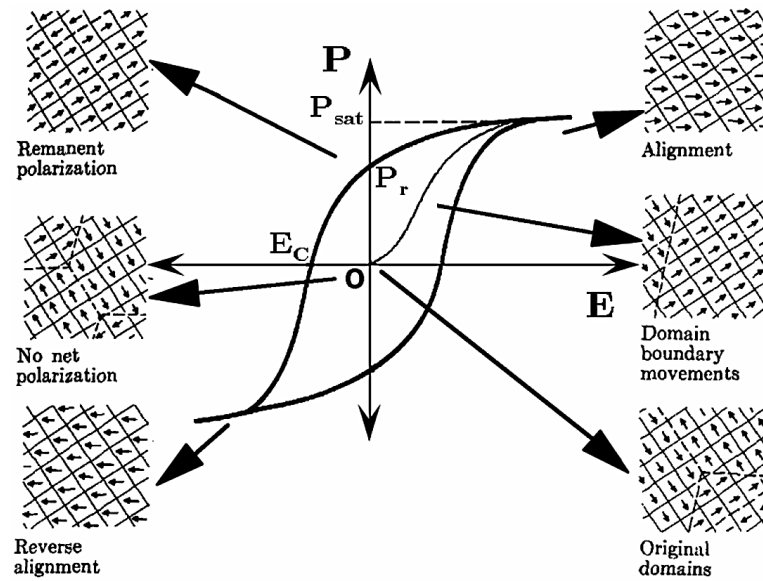


Figure 1.3. Hysteresis loop and domain switching <sup>5</sup>.

Additionally, it can be compared that the response of a crystal based on inversion symmetry to an external force, to understand the importance of symmetry for piezoelectricity. When a crystal with inversion symmetry is subjected to a mechanical stress, there will be no change is observed in the charge locations, as seen in Figure 1.4.a. This type of material does not show electrical response to a mechanical force and so is not piezoelectric. However, when a material without inversion symmetry (polar) as shown in Figure 1.4.b is deformed mechanically, the average charge locations are different. So, this material is piezoelectric, meaning it responds to mechanical force with an electrical response and vice versa, as seen in Figure 1.4.b <sup>6</sup>.

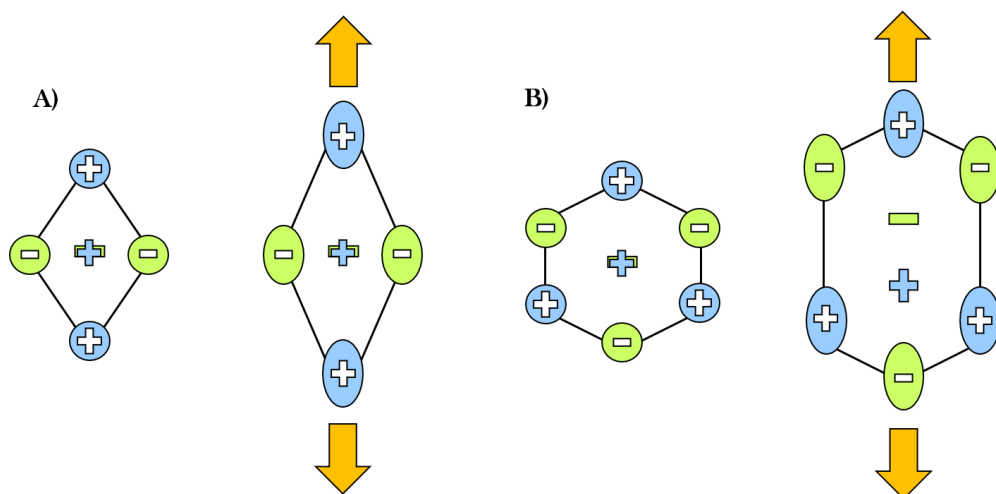


Figure 1.4. External force acting on a crystal a) with/ b) without inversion symmetry.

Piezoelectric effect is a reversible process. So, the piezoelectric materials can exhibit direct and converse piezoelectric effect. In Figure 1.5, there is a schematic explanation of the direct and converse piezoelectric effect. Direct piezoelectric effect means creation of electric charge under mechanical stress, while converse piezoelectric effect is to create strain under an applied electric field. In other words, it can also be called the electromechanical interaction between electrical and mechanical states. The piezoelectric constant ( $d_{33}$ ) is called the constant of this linear relationship. This constant is a 3<sup>rd</sup>-rank tensor ( $i, j, k = 1, 2, 3$ ). The first-rank tensor represents electrical displacement or field, the second-rank tensor represents stress or strain. The piezoelectric equations can be written as following form:

$$D_k = d_{kij} T_{ij} \quad (1.1)$$

$$S_{ij} = d_{kij}^* E_k \quad (1.2)$$

where  $D_k$  is electric displacement ( $C/m^2$ ),  $E_k$  is electric field component ( $V/m$ ),  $S_{ij}$  is strain component,  $T_{ij}$  is stress component ( $N/m^2$ ),  $d_{kij}$  or  $d_{kij}^*$  is component of the piezoelectric charge or strain constant <sup>7</sup>.

$$d_{ij} = \left( \frac{\partial D_i}{\partial T_j} \right)_E = \left( \frac{\partial S_j}{\partial E_i} \right)_T \quad (1.3)$$

Above equation indicates that piezoelectric charge coefficient or piezoelectric strain coefficient. This piezoelectric constant is defined as partial derivatives evaluated at constant electrical field (subscript E), constant stress (subscript T) <sup>7</sup>.

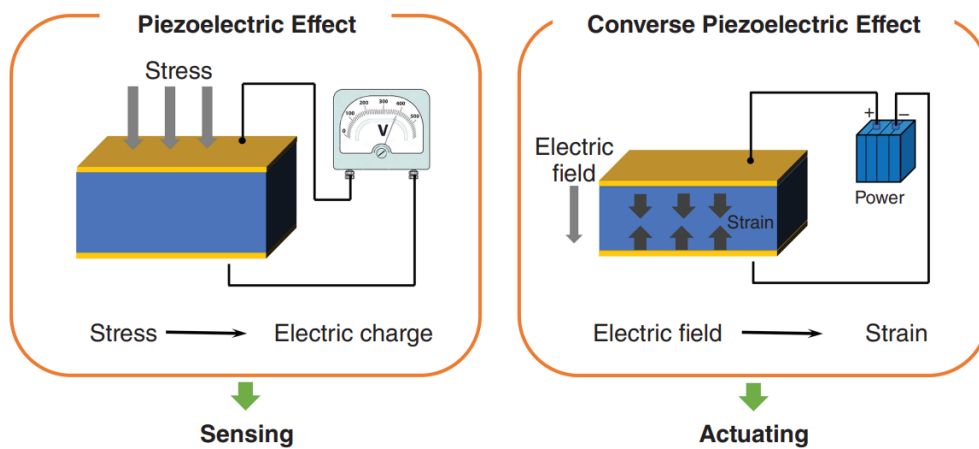


Figure 1.5. Schematic representation of direct/converse piezoelectric effect <sup>7</sup>.

Piezoelectric properties of materials can be compared according to their  $d_{33}$  coefficients. In piezoelectric polymers (e.g., PVDF and its copolymers/terpolymers), evaluation of their properties can be considered by looking at their  $d_{33}$ . For example, piezoelectric coefficients of P(VDF-TrFE) copolymers with the compositions of 70/30, 55/45 and 50/50, are -22.3 pC/N, -26.8 pC/N, and -61.4 pC/N, respectively <sup>8</sup>. According to the literature, high longitudinal piezoelectric performance of 50/50 copolymer can be attributed to its low Young's modulus, and large dielectric constants <sup>8</sup>.

## 1.2. Piezoelectric Materials, Polymers and Their Applications

Ceramics, polymers, and polymer composites are three main groups of piezoelectric materials. The Table 1.1. below, shows typical examples for each category. Piezoelectric material selection is not only related to piezoelectric properties, but also depends on the application area and sector. Therefore, it should be evaluated from a very broad perspective.

Piezoelectric ceramics are polycrystalline materials. They have perovskite crystal structure composed of many numbers of single crystal "grains" which have similar chemical composition <sup>9</sup>. Piezoelectric polymers, which have long polymer chains and are made of carbon, are differentiated from single crystals and ceramics by their superior flexibility <sup>10</sup>. It is hard to process the ceramics because of their brittleness and high stiffness. Piezoelectric polymers have low density, and they are flexible, easy to process, and biocompatible. Although they have low piezoelectric coefficients compared to ceramics, they are often preferred for certain applications due to such properties <sup>11</sup>.

Table 1.1. Examples of piezoelectric material categories <sup>9</sup>

<b>Ceramics</b>	<b>Polymers</b>	<b>Polymer Composites</b>
Barium Titanate	PVDF& Copolymers	PVDF-ZnO
Lead-Zirconate-Titanate (PZT)	PLA (polylactic acids)	Cellulose-BaTiO <sub>3</sub>
KNbO <sub>3</sub>	Cellulose& Derivatives	Polyamides-PZT

There are about 200 piezoelectric materials, especially for energy harvesting applications, and of these, piezoceramics (mainly PZT and BaTiO<sub>3</sub>) have received great attention as they have better piezoelectric properties compared to other ceramics. However, some disadvantages (toxicity, rigidity, lack of design flexibility, etc.) limit its use in applications. For energy-based applications, good piezoelectricity alone is not sufficient, so the design flexibility, frequency of application and volume available are important parameters. Piezoelectric polymers emerge as better types of material for related applications that meet most of the above-mentioned criteria and are currently receiving intense interest <sup>9</sup>.

Some known piezoelectric polymers are polyvinylidene fluoride (PVDF), polyvinylidene fluoride-trifluoroethylene (PVDF-TrFE) copolymer, polyamides (PA), cellulose and its derivatives, polylactic acids (PLA). The best known and most extensively studied polymer is PVDF. It is a suitable polymer for most applications. For example, it is used in applications such as ultrasonic transducers, sound transducers, imaging devices, vibrometers, sensors <sup>12,13</sup>. PVDF has the best piezoelectric properties compared to other piezoelectric polymers. According to a literature, d<sub>33</sub> of PVDF homopolymer is between -24 and -34 pC/N, while d<sub>33</sub> of polyamide and celluloses are 5.7 and 4 pC/N, respectively <sup>9</sup>. So, by looking their d<sub>33</sub> coefficients, PVDF has better piezoelectric property.

Piezoelectric materials have many important applications in engineering, as they have energy conversion in two directions, such as converting mechanical energy to electrical energy (direct effect) or electrical energy to mechanical energy (converse effect). Such properties make piezoelectric materials highly suitable for the design of smart systems. Piezoelectric materials for several engineering applications are summarized in Table 1.2. <sup>14</sup>.

Table 1.2. Piezoelectric materials for engineering applications

<b>Piezoelectric effect</b>	<b>Energy conversion</b>	<b>Applications</b>
Direct effect	Input: Mechanical Output: Electrical	Pressure sensor, Gas Lighter, Accelerometer, Energy harvesting
Converse effect	Input: Electrical Output: Mechanical	Actuators, Piezoelectric pump, Piezoelectric motor, Ultrasonic cleaner
Both direct and converse effects	Input: Electrical/ Mechanical Output: Mechanical/ Electrical	Piezoelectric transformer, Structural health monitoring, Quartz crystal AFM probe

A gas lighter is used to generate electric sparks by utilizing the direct piezoelectric effect. In a gas lighter, a high voltage pulse must be generated across a narrow electrode gap. With a spring mechanism, the PZT cylinder is put under tension by stress impact. This stress causes a high voltage to be produced. This voltage is so high that a spark is generated, causing the air gap between the electrode to break down <sup>14</sup>.

Piezoelectric pressure sensors also benefit from the direct piezoelectric effect. The measured pressure is designed to fall on the piezoelectric membrane, which generates an electrical voltage proportional to the applied pressure. Thin films of quartz, PZT, ZnO are used in piezoelectric pressure sensors. This type of sensor is very sensitive. It is used to measure absolute pressures <sup>14</sup>.

Accelerometers are used in many areas: measurement of impact levels of vehicles in collisions, vibrations in mining operations, seismic vibrations during earthquakes, testing the shock resistance of packaged products, etc. Essentially, a piezoelectric disc is clamped between a base plate and a seismic mass to form a piezoelectric accelerometer. The acceleration has a direct relationship with the output voltage <sup>14</sup>.

Piezoelectric microphones convert sound vibrations into electrical signals. These microphones are designed from thin plate quartz crystals or PZT thin film sheets. The sizes of these films are selected according to the sensitive output signals in the audible frequency range.

Numerous innovative piezoelectric actuators have been created as a result of the converse piezoelectric effect for a variety of applications. The benefits of piezoelectric actuators are that they don't need complicated designs and can produce significant forces with quick response for low-voltage input. A typical actuator would include a tube actuator, a bimorph actuator, a multilayer actuator, and an amplified actuator. Typical actuators only offer a limited range of motion that is proportional to the applied voltage. Due to the demand for wide-range precision motion, piezoelectric motors were created. These motors typically use conventional actuators as the drive source and provide motion over a wide range thanks to sophisticated actuation mechanisms <sup>14,15</sup>.

Due to the merits of ease of processing because of flexibility and low fabrication cost, ferroelectric polymers are preferred for the next-generation applications like memory applications, actuation applications, energy harvesting devices, etc. In some cases, the use of piezoelectric polymers in applications is hampered by their low piezoelectric coefficients and low elastic modulus. But often, the acoustic impedance of

polymers (such as PVDF) is quite compatible with that of water. That is, hydrophones or ultrasonic transducers made of PVDF can be used without quarter-wave coupling. The compatibility of PVDF also means that highly flexible strain sensors can be produced and are used commercially as films and cables <sup>16</sup>.

### 1.3. PVDF Polymers and Their Properties

Even though piezoelectric property is frequently associated with ceramic materials, many polymers exhibit piezoelectric behavior. Polymer-based piezoelectric materials, like PVDF or its copolymer poly- (vinylidene fluoride)-trifluoroethylene (PVDF-TrFE), despite having lower piezoelectric coefficients, are frequently preferred for some applications due to their flexibility, easy processing, biocompatibility, and chemical stability. The ferroelectric, piezoelectric, pyroelectric, and enhanced dielectric properties of these polymers make them multifunctional <sup>16</sup>.

Furukawa et al. established PVDF ferroelectricity for the first time by showing a hysteresis loop in the electric field dependency of the dielectric displacement,  $D(E)$  <sup>17</sup>. Most properties of PVDF, especially piezoelectricity, are related to the strong electric dipole moment of the PVDF monomer unit ( $\text{CH}_2\text{-CF}_2$ -), due to the electronegativity difference between fluorine and hydrogen atoms. PVDF is a semi-crystalline with several different crystal structures ( $\alpha$ ,  $\beta$ ,  $\gamma$  and  $\delta$ ) due to their different chain conformations. Main phases of polyvinylidene fluoride (PVDF) are illustrated in Figure 1.6 <sup>18</sup>.

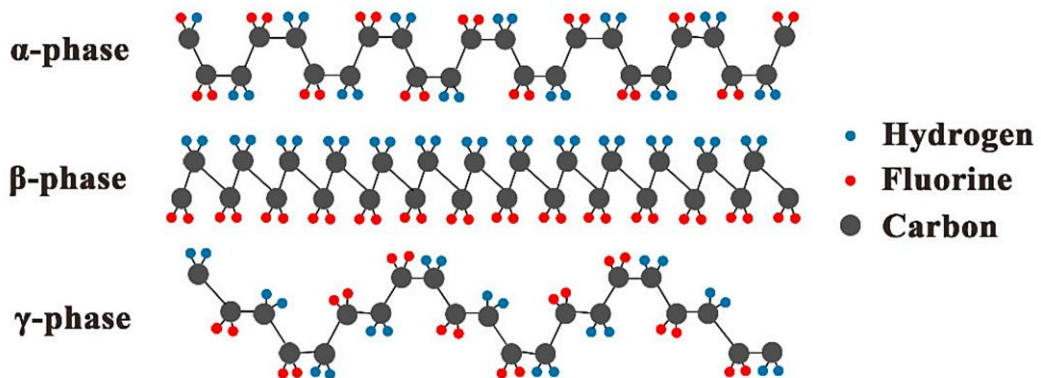


Figure 1.6. Main phases of polyvinylidene fluoride (PVDF) <sup>18</sup>.

Since it has the highest effective dipole moment per unit cell and so exhibits the highest piezoelectricity, the beta-phase ( $\beta$ ) with all trans (TTT) planar zigzag configuration is crucial in this case for piezoelectric applications. In other words, all hydrogens and fluorine atoms are in the same direction within themselves. So,  $\beta$ -phase has highest molecular dipole moment, and it has high net electrical polarization. The  $\alpha$  phase is the most stable phase if the polymer is processed under ambient pressure but this phase does not have ferroelectric properties. This can be understood from the carbon and fluorine atomic positions. By using different processing methods,  $\alpha$ ,  $\beta$ ,  $\gamma$  and  $\delta$  phases of PVDF can be obtained as illustrated Figure 1.7 below <sup>17,18</sup>.

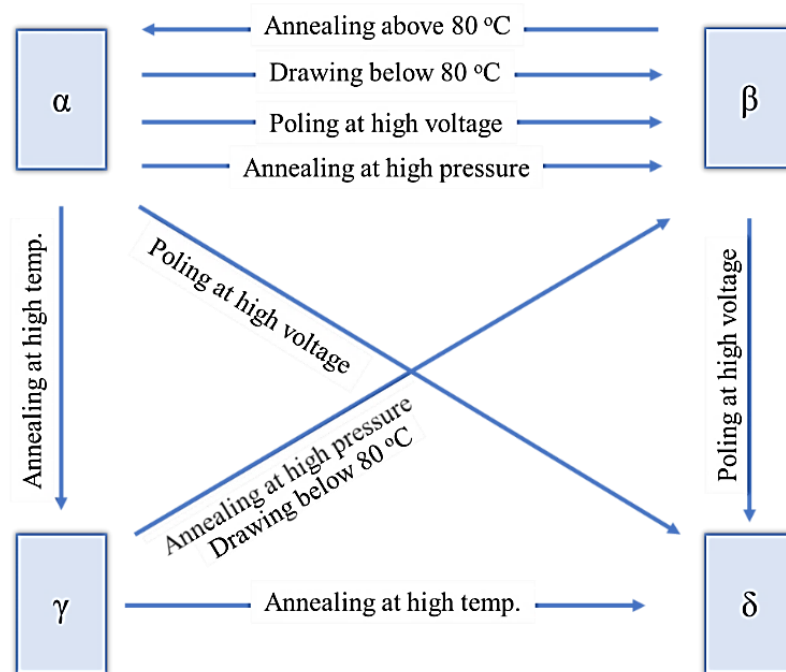


Figure 1.7. Processes used experimentally to produce the different PVDF phases <sup>19</sup>.

Moreover, explaining the piezoelectric effect mechanism in polymers is a difficult task due to the semi-crystalline complex structure of polymers. There are different theories regarding the role of crystallinity in the piezoelectric behavior of polymers. The name of a theory is "Dimensional Model". This model explains the piezoelectric effect in PVDF/ its copolymers and is a very popular theory. In this model, the molecular dipoles in polymer chains are rigid and do not change with an external force. As a result of the material being deformed, the surface charges are moved within the field produced by

these rigid dipoles, causing changes in the charge accumulated at each electrode. Dipoles are assumed to be rigid and fixed. This material deformation is also accommodated by the amorphous matrix. Therefore, the piezoelectric effect can be attributed to the amorphous fraction of the material <sup>20-23</sup>.

On the other hand, some models argue that the piezoelectric effect can be fully explained by considering only the changes in the lattice constants of the unit cell. Accordingly, only the crystalline regions are responsible for the piezoelectric effect, and the amorphous matrix is just a matrix. Thus, the piezoelectric mechanism in polymers most likely lies somewhere between these two limiting situations.

According to these arguments, piezoelectricity of PVDF can be due to change in volume of the amorphous part, or changes in the lattice constants of the unit cell. Although piezoelectric coefficients are positive for all piezoelectric materials, PVDF and its copolymer/terpolymer exhibit negative longitudinal piezoelectric coefficient ( $d_{33}$ ). This is due to contraction with applied electric field of both the crystalline and the amorphous part of the semicrystalline polymers. To analyze these contradictory situations, Katsouras et.al. <sup>24</sup> performed 'In-Situ Dynamic X-ray Diffraction' measurements on PVDF-TrFE. They found that piezoelectric effect is dominated by lattice constant change. However, this situation could not be explained by electrostrictive contribution of crystalline regions of polymers alone. The reason for this situation was thought to be due to an electromechanical connection between intermixed crystal lamellae and amorphous regions. In other words, the situation is due to the composite internal microstructure of polymers.

In conclusion, electrostriction, the dipole-induced piezoelectricity, causes the crystalline lamellae to contract when an electric field is applied to PVDF or its copolymers. The lattice constant decreases. At the same time, the amorphous regions in between the polar lamellae also contract. As a result of this contraction in the lamellae, an additional internal compressive stress will occur, which will cause the lattice constant to decrease further. <sup>24</sup>. The tandem contraction caused by the relative orientation of polarization and electric field correspond to a negative piezoelectric coefficient.

Figure 1.8 shows searching for "PZT", "PVDF", "Piezoelectric polymer" and "Lead-free Ceramics" in the Scopus database. Graph for number of publications between 1980-2022 containing these keywords which is constructed in May 2023, is shown in this Figure 1.8. If the graph is examined, while the publications about lead-free ceramics and

polymers with piezoelectric properties are increasing, the publications about lead containing PZT ceramics have decreased from year to year although it is the most common piezoceramics in industry due to toxicity of lead. Considering only these data, environmentally friendly PVDF seems to be a potential piezoelectric material of the future. In addition, as mentioned earlier, PVDF is also gaining attention due to its remarkable chemical properties.

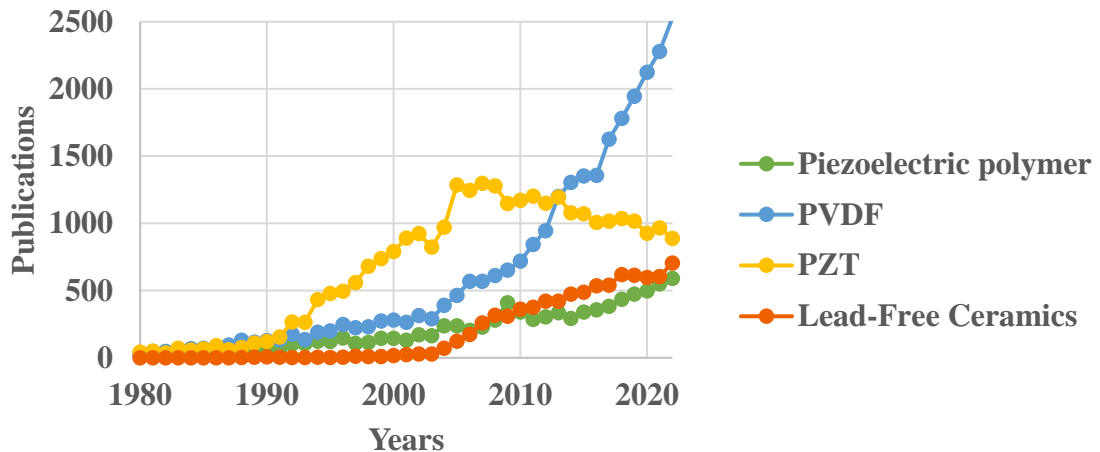


Figure 1.8. Graph for number of publications between 1980-2022 containing the keywords Piezoelectric polymer, PVDF, PZT and Lead-free ceramics from Scopus database (accessed on 2023, May 15).

#### 1.4. Copolymer and Terpolymer of PVDF

PVDF monomers are usually combined with other monomers to modify the crystal structure, strengthen, and stabilize the piezoelectric properties. It was discovered approximately 40 years ago that adding a certain quantity of trifluoroethylene (TrFE, CFH-CF<sub>2</sub>) to VDF causes direct crystallization from the melt or solution to the ferroelectric  $\beta$ -phase<sup>25,26</sup>. It is a major advantage for integration of these polymer layers in technical devices. When trifluoroethylene (TrFE) is used, the generated piezoelectric phase, known as the " $\beta$ -phase," can generally account for more than 50% of the overall volume. Since it is ferroelectric without mechanical stretching, P(VDF-TrFE) has an advantage over pure PVDF<sup>27</sup>. The increase in crystallinity is another beneficial impact. TrFE is incorporated to promote the growth of crystalline regions.

In addition, because of the interchain distance in copolymer is larger due to big and bulky TrFE group, dipole moments can easily rotate in copolymers. So, piezoelectric coefficient ( $d_{33}$ ) for copolymers is higher than that of homopolymers, which is expected to cause a better transfer performance between mechanical and electrical energy. While the piezoelectric coefficient ( $d_{33}$ ) for the PVDF homopolymer is approximately 30 pC/N, the piezoelectric coefficient for the copolymer varies between approximately 45-65 pC/N<sup>28,29</sup>. Structure and polymerization of PVDF and PVDF-TrFE can be seen from Figure 1.10. Also, due to addition of TrFE (mol%), phase transitions can be observed in Figure 1.9 below. According to this graph, as VDF content increases, Curie Transition temperature increases. In homopolymer PVDF, Curie temperature is higher than the melting point of PVDF<sup>30</sup>. It melts before the ferroelectric-paraelectric phase transition occurs. In addition, this property of homopolymer also can be seen from the dielectric measurements.

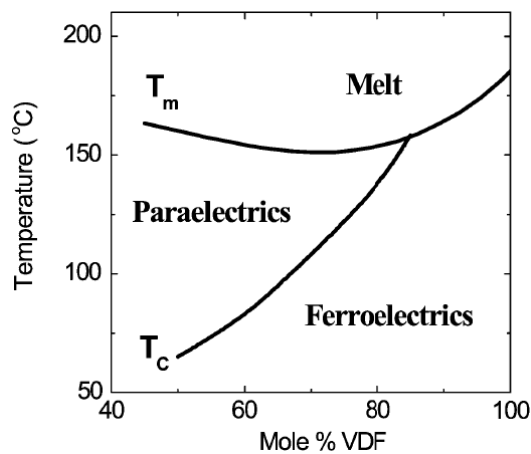


Figure 1.9. P(VDF-TrFE) phase diagram<sup>31</sup>.

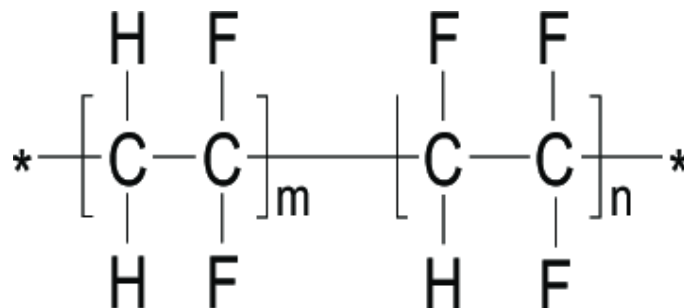


Figure 1.10. Structure of VDF-TrFE<sup>32</sup>.

The addition of a third monomer to the co-polymer to shorten the long-range order created by the second monomer is a relatively recent approach. This addition creates nanopolar regions and decreases ferroelectricity. These nanopolar regions improve polarizability of terpolymers. So, PVDF-based terpolymers are usually relaxors. In the below paragraph, difference between normal and relaxor ferroelectric is described. The addition of a third monomer can increase the inter-chain distance, which encourages the flipping of the dipole, as well as reduce the length of VDF-TrFE chain segments and change the crystal size <sup>29</sup>.

The modified copolymers exhibit numerous characteristics typical of ferroelectric relaxors and have a relatively high room-temperature dielectric constant. These findings show how adding "defect" structures can significantly alter and enhance the qualities of PVDF-TrFE based polymers. An irradiated sample was used to study the first copolymer derivative <sup>33</sup>. Electron irradiation introduces random defects such as large pendant groups and crosslinks into the crystallite regions. Thus, it stabilizes the trans-gauche conformation at room temperature and leads to a significant change in the microstructure. It transforms the ferroelectric copolymer system into a relaxor ferroelectric state <sup>34</sup>. Figure 1.11 (A, B, C) is the schematic hysteresis loops for (A) normal ferroelectric, (B) relaxor ferroelectric, and (C) dielectric materials. From dielectrics to normal ferroelectrics, dielectric nonlinearity increases. The bottom section of this Figure 1.11 (D, E, F) shows the ferroelectric domain structures of (D) normal ferroelectric, (E) relaxor ferroelectric, and (F) dielectric polymers. Domain size increases towards ferroelectrics <sup>35</sup>.

If there are no ferroelectric domains (when dipoles cancel each other out), the materials show linear electric polarization. The dielectric behavior results from only atomic and electronic polarizations rather than dipolar orientation and interfacial/ionic polarizations. In addition, reducing the ferroelectric domain size to accommodate a few dipoles [i.e., nanodomains in relaxor ferroelectrics (RFE)] significantly reduces cooperative coupling between ferroelectric domains. As a result, spontaneous polarization is reduced, resulting in narrow single hysteresis loops <sup>35</sup>.

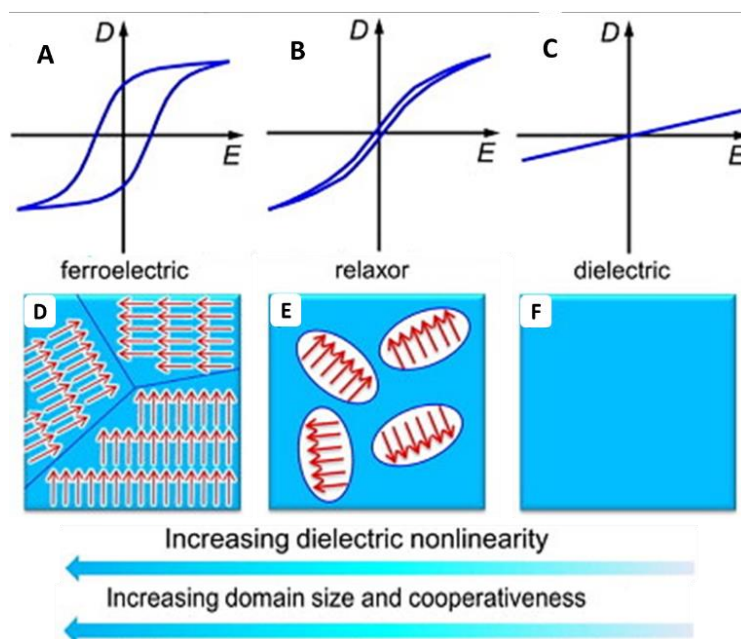


Figure 1.11. Schematic hysteresis loops and domains for normal ferroelectric, relaxor ferroelectric, and dielectric materials <sup>35</sup>.

A third monomer was added to the polymer chain to achieve similar levels of strain without the need to irradiate polymers. The terpolymer technique has the benefits of considerably simplifying the processing of the polymers and completely removing the unfavorable side effects to the polymer created via irradiation, such as radical formation, chain scission, and crosslinking. Both the broad dielectric constant peak and reasonable electrostrictive strain responses can be produced by such terpolymer systems, which were also shown in samples of irradiation copolymers. The termonomer used affects the performance of the terpolymer. CTFE (chlorotrifluoroethylene) and CFE (chlorofluoroethylene) are generally used as termonomer in PVDF-TrFE polymer systems <sup>34</sup>.

Table 1.3, shows physical and electrical properties of these most used homopolymer, copolymer and terpolymer of PVDF from the literature. Piezoelectric coefficients ( $d_{33}$ ) of terpolymers are higher compared to homopolymer and copolymer. Dielectric constant ( $\epsilon_r$ ) exhibits similar trend with piezoelectrics coefficient.

Table 1.3. Physical and electrical properties of homopolymer, copolymer and terpolymer of PVDF.

Polymers	T <sub>melting</sub> (°C)	P <sub>maximum</sub> ( $\mu\text{C}/\text{cm}^2$ )	$\epsilon_r$ (at 25 °C and 10 Hz)	d <sub>33</sub> (pC/N) or (pm/V)
Pure PVDF	160.9 28	6.8 28	15 36	-34 37
P(VDF-TrFE) (55/45 mol%)	159.1 28	10.9 28	16 30	-52 37
P(VDF-TrFE) (50/50 mol%)	162.3 28	9.6 28	18 30	-66.67 38
P(VDF-TrFE-CTFE) (80/12/2 mol%)	120 –140 28	5.2 39	47 39	-81.64 40
P(VDF-TrFE-CFE) (58.3/34.2/7.5 mol%)	130 39	8.5 39	55 39	-

## 1.5. Piezocatalytic Property and Mechanisms

In today's world, the release of colored organic pollutants such as dye resulting from activities such as agriculture, industry, papermaking, food production, causes environmental pollution and endangers the lives of people, animals, plants, constitutes a major obstacle for sustainable development<sup>41,42</sup>. For example, the most used one among these dyestuffs is Rhodamine B (RhB). It is an organic pigment with a bright red color. It is widely used as a colorant in the food and textile industries due to its high solubility in water and cost-effectiveness. It is also known to be used for the determination of water flow direction and velocity. According to some studies, it has been found to be carcinogenic in animals and humans<sup>43</sup>.

As a result of developing industrial activities, people have developed many methods such as filtration, adsorption, separation by gravity and so on to destroy these harmful pollutants. However, these physical methods transfer organic and inorganic pollutants from wastewater to another solution medium. Since these methods can cause secondary pollution, they cannot be used as a permanent solution method most of the time

<sup>44,45</sup>. In chemical methods, non-reusable reactive materials need to be transferred to water again, and these chemical methods cause secondary pollution like physical methods. In addition, most biological methods cannot be applied due to the high toxicity of polluting dyestuffs <sup>46,47</sup>.

Photocatalysis, an advanced oxidation process, generates active species and stimulates redox reactions to enable and increase the rate of degradation. A large amount of light source is required for photocatalysis. The efficiency of this process depends on the physical and chemical properties of the photocatalyst. In addition, photocatalytic activity is dependent on the transport-separation efficiency of the electron-hole pairs, thus hampering the practical application of photocatalysis. Therefore, as an alternative to photocatalysis, environmentally friendly piezocatalysis can be given as an example. It has recently been used for the treatment of wastewater. Piezoelectric catalysis takes advantage of the piezoelectric effect and uses mechanical vibration to produce active species on opposite surfaces of matter for degradation of dye. Piezoelectric materials might benefit from a built-in electric field because of their inherent non-centrosymmetric property, which help to separate and transfer electron-hole pairs and improved its own catalytic activity <sup>48-55</sup>.

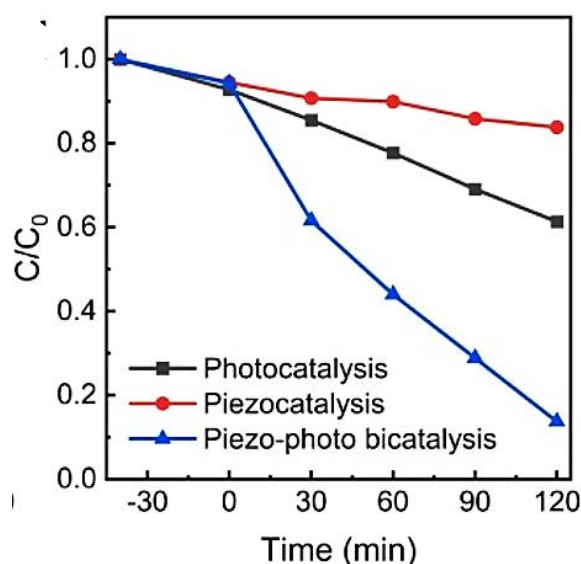


Figure 1.12. The absorbance ratio of dye with time for 3 kinds of catalysis type <sup>56</sup>.

In addition, piezocatalysis and photocatalysis have been used simultaneously in the literature as bicatalysis. The joint use of solar energy and mechanical vibration energy

is a new method that has emerged in the removal of water pollution. Combined bicatalysis is always expected to have a higher degradation rate than single catalysis. According to a study <sup>56</sup>, piezo photo bicatalysis showed a much higher degradation rate than individual photocatalysis and piezocatalysis, exhibiting a great synergy enhancement as shown in Figure 1.12 <sup>56</sup>.

Chemical catalytic reactions induced by vibration were named mechano-catalysis or piezocatalysis in 1998 <sup>57</sup>. Due to its non-toxicity and good chemical stability, it is also used in various applications such as the vibration separation of water for hydrogen production <sup>58</sup>. Some of the piezoelectric materials reported to use for dye degradation were BaTiO<sub>3</sub>, LiNbO<sub>3</sub>, BiFeO<sub>3</sub>, etc. <sup>59-61</sup>. In addition, piezocatalysts in particulate form have also been worked in some reports. However, they have low stability, difficult recovery, agglomeration, a toxic nature, and recyclability difficulties. Due to these problems and limitations associated with piezo-catalyst, polymer based flexible films such as PVDF started to be used <sup>62</sup>.

### **1.5.1. Mechanisms of Piezocatalytic Effect**

Piezocatalysis, like other frequently used methods, does not change the composition, content, and quality of the contaminated water. It is simple, practical, and worth researching, also is a trend research field today. Essentially, piezoelectric materials can generate electron-hole separation in response to external vibration, which considerably promotes the generation of various reactive oxygen species (ROS) and speeds up the rate at which pollutants degrade <sup>63</sup>.

More piezoelectricity produces more field of polarization. So, it increases the separation of charge carriers (h<sup>+</sup> and e<sup>-</sup>) in opposite directions under this field. Due to piezoelectric potential, migration of charge carrier can be easy and fast. It means that good piezoelectricity increases the piezocatalytic activity <sup>64</sup>.

There are two main piezocatalysis mechanisms available in the literature up to now. One is energy band theory; another is screening charge effect. In energy band theory, the theory inspired by photocatalysis, piezocatalytic process is mainly depends on energy band level (valence and conduction bands). In this theory, the piezopotential adjusts the band structure. It acts as a gate to initiate the reaction. It controls the flow of "internal charge carrier" to the catalyst surface. The second mechanism, which is named as

screening charge effect, is associated with external screening charges (for example, surface charged adsorbates from an outside system). In other words, piezopotential, which is the driving force, must reach or exceed the Gibbs free energy change of the system reaction. In addition, another important difference is that the charges involved in redox reactions are internal charges in the material in energy band theory, but in the screening charge effect theory these charges are surface-adsorbed charges <sup>65</sup>.

According to the “Energy Band Theory”, the main characteristics that control the catalytic activities are the band configuration and electronic states of piezocatalysts. Since this theory was inspired by photocatalysis, the processes that take place can be attributed to photocatalysis. In photocatalysis, the excitation of electrons occurs with a photon. Electrons are excited from the valence band to the conduction band and holes are formed in the valence band. Depending on the energy band level, photogenerated carrier electrons and holes initiate redox reactions. However, in piezocatalysis, the source of carriers is mechanical excitation (e.g., ultrasonication) or intrinsic free charges. For example, since the cavitation bubbles produced by ultrasonication have high pressure (up to  $10^8$  Pa), they cause the transition from the valence band to the conduction band by exciting the electrons <sup>65</sup>. When ultrasound is applied to the fluid, the acoustic pressure will spread in waveform. Cavitation bubbles are created and expand as a result of the extrusion of water molecules during the positive phase of pressure change and their disintegration during the negative phase. The impact force on the catalyst can be extremely high ( $10^8$ - $10^9$  Pa), when the cavitation bubbles collapse at a critical size (in general several tens  $\mu\text{m}$ ) <sup>66</sup>.

Free or unpaired charges resulting from the defect nature of materials are another important charge carrier for piezocatalysis. For example, oxygen, selenium, and sulfur vacancies, which are common anion defects in a material, create free electrons and provide to maintain a neutral internal charge. In this way, piezocatalytic activity can be increased by increasing the concentration of these free charges. The schematic representation of these two possible charge carriers arising from mechanical excitation and materials defects can be seen from the Figure 1.13.

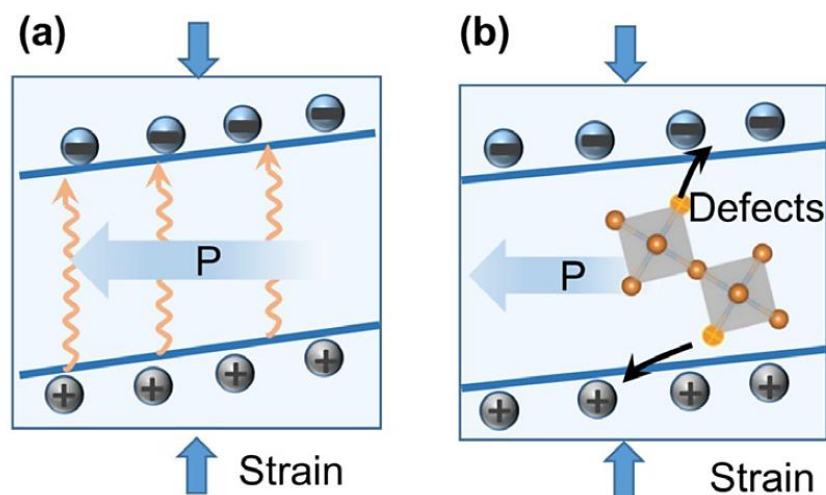


Figure 1.13. Possible charge carriers arising from mechanical excitation and materials defects<sup>65</sup>.

In some cases, the catalytic formation of radicals may not be thermodynamically favorable. This is due to the mismatch of the band level of the material and the potential required for the redox reaction. However, by tilting the band structure with strain, the necessary positions for the valence band and conduction band can be provided. Generally, the band tilting degree depends on the piezopotential magnitude. The schematic representation of such a situation is given in the Figure 1.14 below.

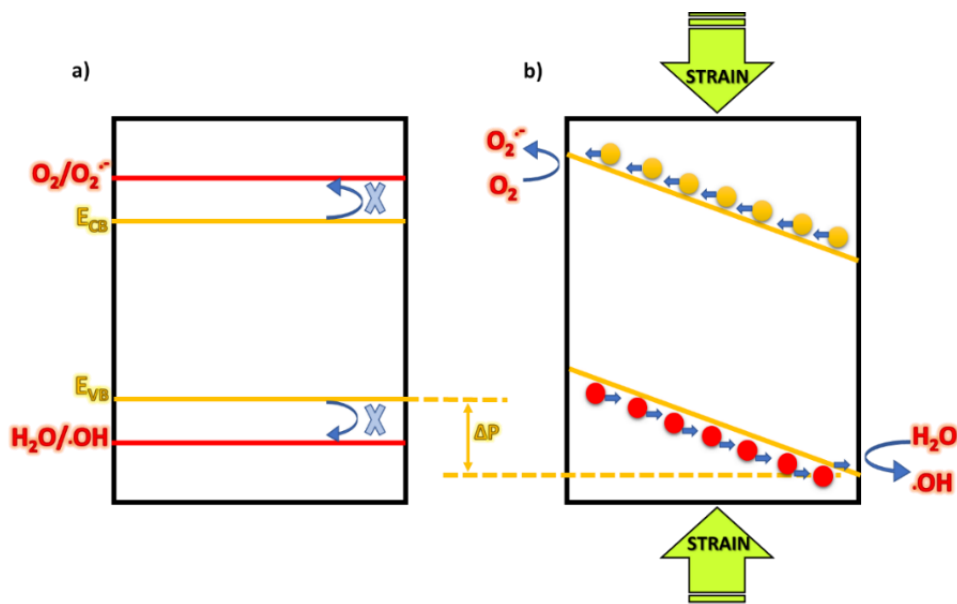


Figure 1.14. Schematic illustration of a material band structure and accompanied redox potentials of ROS generation under a) static states and b) applied strain.

If the intensity of the mechanical vibration is increased, the electronic conduction resistance is gradually reduced. This supports the charge mobility of the stronger piezopotential field. In addition, when comparing the relatively weak spontaneous polarization field with the stronger piezoelectric polarization field, the stronger polarization is advantageous for piezocatalysis process <sup>65</sup>.

According to the “Screening Charge Effect” theory, in order to be compatible with electrocatalysis and determine the ability of the piezocatalyst to realize a certain chemical reaction, the magnitude of the piezopotential should entirely match the necessary redox level. More importantly, the piezocatalytic process is controlled by the surface screening behavior driven on by polarization.

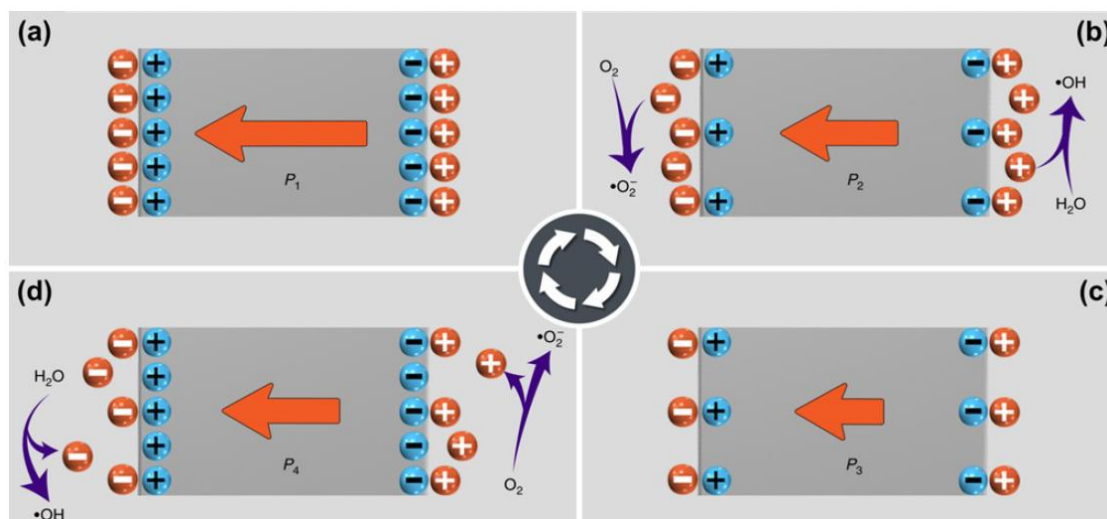


Figure 1.15. Working principle of piezocatalysis based on the screening charge effect.

In order to explain the mechanism, the BaTiO<sub>3</sub> example can be used. This material is electrically neutral because after the charges are induced by polarization, they are balanced by external charges on both polar surfaces (Figure 1.15.a). After a mechanical action such as vibration, this temporary charge balance is disturbed, and the polarization loses its strength. Thus, extra screening charges are released from the surface (Figure 1.15.b). These free charges initiate redox reactions, and this process continues until a new electrical balance is reached (Figure 1.15.c). After the applied mechanical treatment is removed, the polarization is restored and with more polarization, more charge is produced. That is, the space charges from the electrolyte will be adsorbed on the surface

again. Thus, it will leave these charges of opposite polarity (to adsorbed charges) in the electrolyte to participate in the reactions (Figure 1.15.d) <sup>65</sup>.

To summarize, the concept of piezopotential is very important in terms of piezocatalysis for both theories. The only difference is how piezopotential contributes to catalytic processes. In energy band theory, the piezopotential field acts indirectly. It performs band tilting manipulation and provides driving force for separation and conduction of charge carriers. The advantages of this feature are that it reduces the activation energy and prevents reverse combination of electron-hole pairs. However, in screening charge effect, energies of the charge carriers are directly determined by piezopotential. Consequently, under the theory of screening charge effects, the piezopotential controls a piezocatalyst's ability to influence a chemical reaction, while the catalysts' energy band levels control the kinetics of reaction (energy band theory) <sup>65</sup>.

In addition, in both mechanisms, the source of reactive charges is different. In energy band theory, the main source of internal charges may be a mechanical excitation or defect structures in the material. But screening charge effect indicates that the redox processes, which are entirely dependent on the surface screening phenomena, are induced by the external screening charges that have been released. According to energy band theory, high conductivity in piezocatalyst is often desired. However, for screening theory, it can be negative effect because of the accelerating the surface mobile charge dissipations and suppressing their retention on surface <sup>65</sup>. The Table 1.4 below gives the most basic differences between the theories.

Table 1.4. Difference between energy band theory and screening charge effect.

<b>Energy Band Theory</b>	<b>Screening Charge Effect</b>
Material internal charges	External screening charges
Mechanical excitation	Change in polarization
Band level determines catalytic capacity	Piezopotential determines catalytic capacity

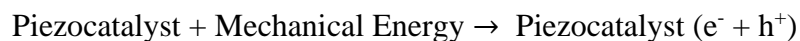
In other words, piezoelectric crystals exist in a neutral state under typical conditions. In some situations, the atoms in their structures may not be symmetrical every time. Despite it is non-centrosymmetric, an electric dipole in a crystal is neutral because a positive charge cancels out a nearby negative charge. The structure of the crystal deforms when it is compressed, disrupting the balance of the positive and negative

charges. In addition, the band structures can also change. As a result, the electrons and holes move to the crystal's opposite sides, creating an electric field there. The materials' HOMO and LUMO electrical energy levels are also altered by the piezo potential. The conduction band (CB) is lowered to a point below its highest occupied molecular orbital (HOMO). The HOMOs will therefore transfer their electrons to the CB. Electrons will move from the valence band (VB) to the lowest empty molecular orbital on the opposite side (LUMO).

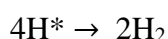
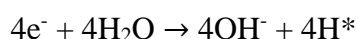
One of the approaches to increase the efficiency of electrochemical processes by taking advantage of the strain state of a material is piezocatalysis: the interaction of the native electronic state of the piezoelectric material, a strain-induced piezoelectric potential, and the composition of the surrounding medium results in piezocatalysis. When a piezoelectric material is mechanically deformed, a high electric field is generated, increasing the energetics of both free and bound charges throughout the material. The electrochemical potential difference between the charges on the surface of the piezoelectric material and in the surrounding medium has a significant impact on the thermodynamic stability and kinetics of electrochemical reactions that take place there<sup>63</sup>.

Furthermore, the electron-hole pairs that came from the mechanically deformed catalysts migrate (in the opposing direction) and gather at the catalysts' surface. With external piezoelectric stimulation, enough electron-hole pairs are accumulated at the surface to start redox reactions.

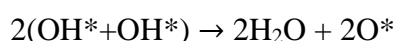
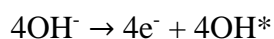
Piezo-sourced electrons on the surface of the catalyst capture H<sub>2</sub> molecules from the water and form hydrogen radicals. Thus, H<sub>2</sub> gas and OH radicals are formed. At the cathode, these OH radicals (hydroxyl radical) are released from the holes and trap the electrons in this hydroxyl group. The degradation of the dyestuff/or pollutants is basically caused by such OH\* radicals in the aqueous medium<sup>63</sup>. Basic schematic representation of piezocatalytic degradation can be seen from the Figure 1.16.

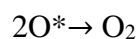


Anodic reactions:



Cathodic reactions:





Pollutant degradation:

$OH^* + \text{pollutant} \rightarrow \text{degradation product of the pollutant.}$

$e^- + \text{pollutant} \rightarrow \text{degradation product of the pollutant.}$

$h^+ + \text{pollutant} \rightarrow \text{degradation product of the pollutant.}$

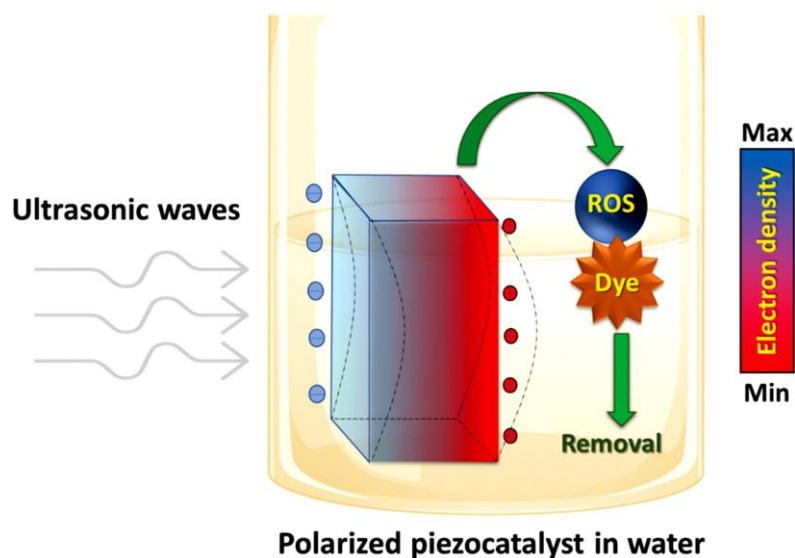


Figure 1.16. Mechanism of the piezocatalytic degradation <sup>63</sup>.

## 1.6. Literature Review

The piezocatalytic dye-degradation studies about homopolymer and copolymer, and their ceramic-added composites increases nowadays. This area is relatively new, environmentally friendly, and promising. Common aims of these types of studies are to increase the efficiency of removing the dyestuffs/impurities/pollution in water by creating a piezoelectric effect by ultrasonic vibration and generating radicals from the polymer. In this part, several studies about this area which is about piezocatalytic dye-degradation will be explained.

Sharma et al.<sup>64</sup> synthesized ferroelectric  $Ba_{0.85}Ca_{0.15}Zr_{0.1}Ti_{0.9}O_3$ /polyvinylidene difluoride (PVDF) composite film for the treatment of water using the piezocatalysis process. The BCZTO ( $Ba_{0.85}Ca_{0.15}Zr_{0.1}Ti_{0.9}O_3$ ) content in composite films was 0, 5, and 10 wt. % of PVDF. The most efficient dye degradation was obtained in 10 wt. % BCZTO/PVDF composite films, The degradation of methylene blue (MB), Rhodamine

B, and methyl orange dyes were approximately 91%, 86%, and 90% for 180 minutes, respectively. According to this study, hydroxyl radical ( $\cdot\text{OH}$ ) is the main species for piezocatalytic dye degradation. In addition, with increasing sonication power, dye degradation performance increased.

The piezocatalytic activity of all the films was determined using sonication treatment and dye degradation. From UV-visible spectroscopy, the characteristic spectrum peak was recorded as 664 nm. Sharma et. al. obtained promising piezocatalytic activity as seen in Figure 1.17 and Figure 1.18. It can be concluded that MB dye degradation was  $\sim 37\%$  for bare PVDF,  $\sim 70\%$  for 5 wt. % BCZTO/PVDF and  $\sim 91\%$  in case of 10 wt. % BCZTO/PVDF film. It can be said that increase in BCZTO content helped to improve the piezocatalytic dye degradation performance due to increasing piezoelectric charge on the surface of the piezoelectric film<sup>64</sup>. More polarization fields are created by increased piezoelectricity, and as a result, more free charge carriers ( $h^+$  and  $e^-$ ) are able to separate from one another by moving in opposing directions in response to field forces.

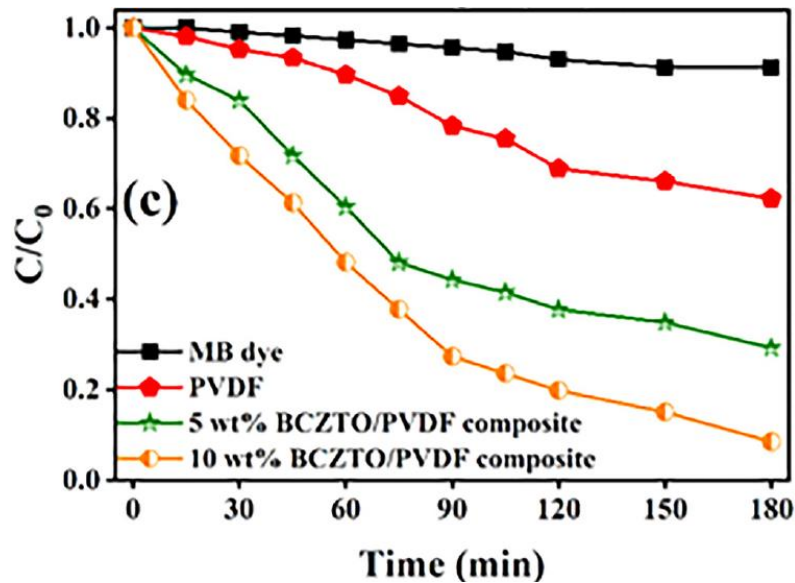


Figure 1.17. Piezocatalytic dye degradation performance in terms of  $C/C_0$  vs  $t$  plots for composite films<sup>64</sup>.

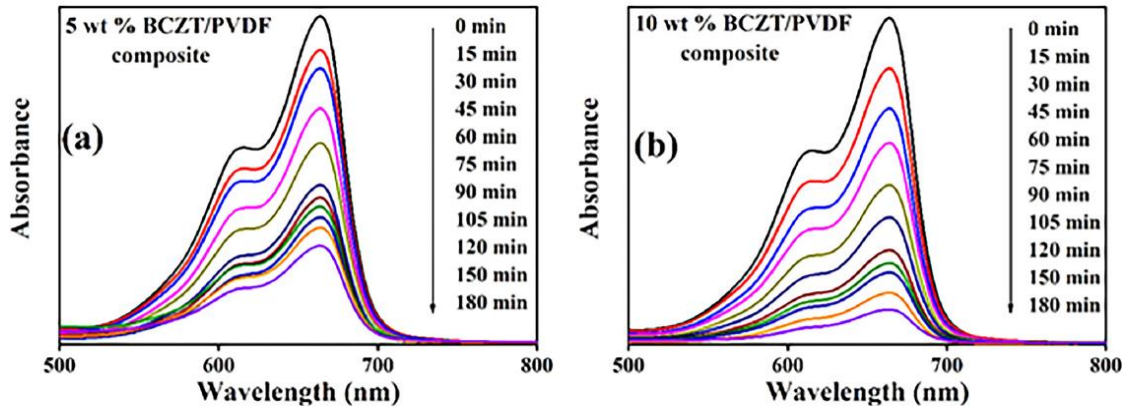


Figure 1.18. UV-visible spectrum peaks at 664 nm with sonication time during piezocatalytic MB dye degradation experiments using 5 and 10 wt.% BCZTO/PVDF composite films <sup>64</sup>.

Wan et. al. <sup>67</sup>, studied BaTiO<sub>3</sub> nanocubes embedded in piezoelectric PVDF polymeric membrane. They synthesized pre-modified controlled oxygen vacancies in ceramic barium titanate (BTO-OVs) to enhance reactive species/radicals' generation. Piezocatalytic performances of composites were investigated by degradation of BPA (Bisfenol A) in ultrasonic cleaner. The use of nanocubes created more free charge by increasing the surface area, and as a result, it increased degradation by generating more radicals. The degradation of pristine PVDF obtained as almost negligible. According to the results, HPVDF/BTO-OVs can degrade 98% of BPA, as shown in Figure 1.19. As it is well-known, PVDF's piezoelectricity is dependent on the  $\beta$  phase content. The addition of BTO-OVs nanocubes improved  $\beta$ -phase formation in PVDF.

The addition of pre-modified controlled oxygen vacancies in ceramic barium titanate improves their piezoelectric properties. Creating oxygen vacancies can activate and adsorb oxygen (O<sub>2</sub>) in water. Also, porous structure can provide channel for oxygen (O<sub>2</sub>) input more rapid, and further generating more active oxygen species. Therefore, more piezoelectric potential was created. Then more charge carriers accumulated. Thus, PVDF/BTO-OVs had enhanced BPA degradation.

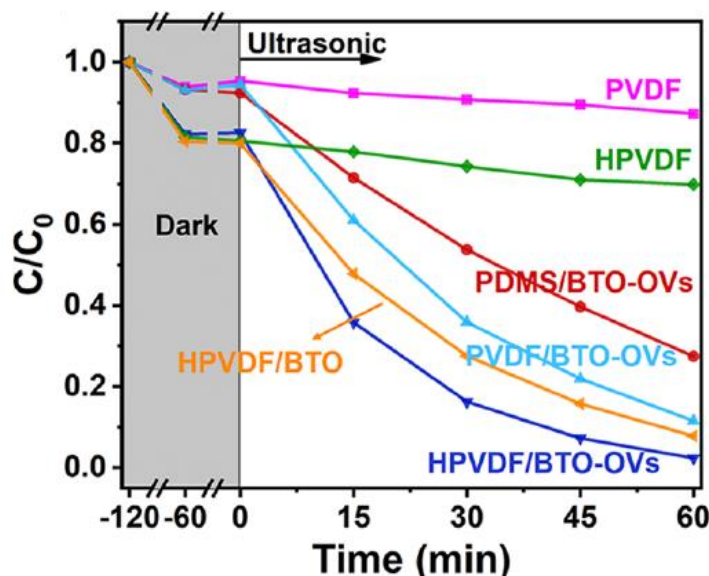


Figure 1.19. Piezocatalytic degradation curves for polymer/ceramic composites <sup>67</sup>.

These hydrophilic porous composite membranes had good piezocatalytic activity due to their hydrophilicity and porosity formed by surface modifications. Piezoelectric property of barium titanates and high  $\beta$ -phase contents of PVDF polymers provided the superior activity. According to this study, polymer-ceramic composites were deformed under ultrasonic vibration. Polarized charges are induced on the surfaces of the polymer and ceramics. So, internal polarization electric fields are created. Due to this field, electrons and holes are separated. Then, they migrate to the surface of the ceramic. OH radicals form and degradation occurs <sup>67</sup>.

Singh et al. <sup>62</sup> studied on flexible PVDF-LiNbO<sub>3</sub> composite films to investigate piezocatalytic dye degradation, pharmaceutical degradation, and bacterial disinfection. They used the solution casting method to synthesize polymers and the solid-state reaction method for ceramics. Dye degradation efficiency was recorded using UV-visible spectroscopy. Experimental results are given in Figure 1.20. Both LN-PVDF and Ag/LN-PVDF showed remarkable degradation of dye after 120 minutes. Degradation efficiency of Ag/LN-PVDF samples was 89%, LN-PVDF was 67%, and bare PVDF was 37%. So, piezocatalytic performance increased in this order: PVDF < LN-PVDF < Ag/LN-PVDF films. As mentioned earlier <sup>67</sup>, piezoelectric nature of LiNbO<sub>3</sub> and piezoelectricity present in the  $\beta$ -phase of PVDF can enhance the degradation efficiency. In addition, loading of Ag metal on ceramics can increase electron-hole pair separation. It can be said that Ag can be an electron trap. For these reasons, more free charges can be created, and more

reactive oxygen species are produced. So, efficient degradation occurs. As noted in every study, species OH is responsible for dye degradation in this study as well.

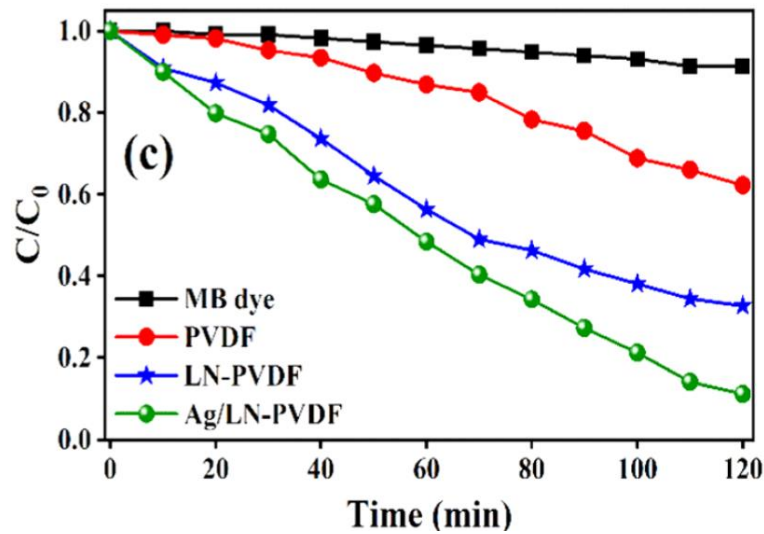


Figure 1.20. Piezocatalytic dye degradation performances of PVDF, LN-PVDF and Ag/LN-PVDF composite films. in terms of  $C/C_0$  with vibration time <sup>62</sup>.

Jiang Wu et. al. (2018) <sup>68</sup> used BaTiO<sub>3</sub> (BTO) nanoparticles which annealed at different temperatures (BTO-200, BTO-400, BTO-600, BTO-800, BTO-1000, and BTO1200). BTO samples were used to degrade methyl orange (MO) dye under ultrasonic vibration (40 kHz, 80 W). Experiments were carried out in the dark environment to prevent photocatalytic effect. According to the experimental results, the graphs of the relative concentration ratios  $C/C_0$  of MO over different piezocatalysts were given in Figure 1.21 as a function of degradation time. The experiments in the absence of ultrasonic vibration and BTO catalyst showed negligible degradation of methyl orange. Jiang Wu et. al. concluded from this result that piezoelectric effect is required for piezocatalysis.

From the piezocatalytic experimental results <sup>68</sup>, if the annealing temperature is below 800 °C, in the crystalline property there is no notable change. With increasing annealing temperature of BTOs, piezocatalytic efficiency of ceramic particles increased, then decreased. This can be due to the stronger tetragonal distortion in the sample which enhances piezoelectricity and the maintenance of the single particle morphology <sup>68</sup>.

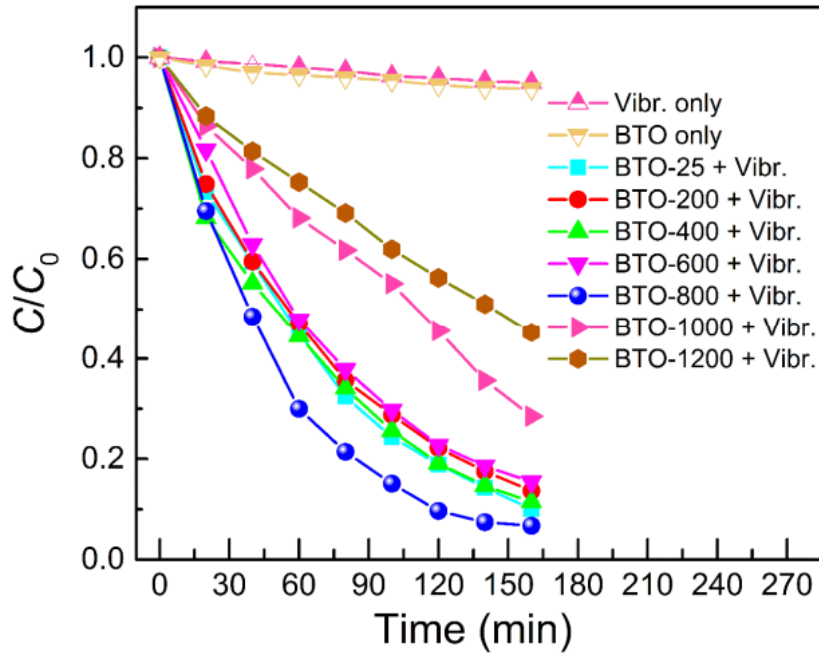


Figure 1.21. Piezocatalytic degradation of methyl orange with ultrasonic vibration in the presence of BaTiO<sub>3</sub> samples <sup>68</sup>.

## 1.7. Research Objectives

In this study, homopolymer PVDF, copolymer P(VDF-TrFE) (55/45) and (50/50), and terpolymer P(VDF-TrFE-CTFE) were studied. Their piezoelectric and piezocatalytic properties were investigated and compared. The main purposes of this thesis study are to produce polymers with good and efficient piezoelectric and piezocatalytic properties, to remove impurities and dyestuffs in water, and to observe how these properties change by adding 2nd and 3rd monomers to the homopolymer. It is also aimed to be a comparative study comparing the piezoelectric and piezocatalytic properties of both homopolymer, copolymer and terpolymer. In addition, it was desired to observe whether the piezocatalytic property would increase with increasing piezoelectric property.

In order to achieve all these purposes, that is, to strengthen the piezoelectric properties, the most suitable process parameters were selected in the synthesis stage. The  $\beta$ -phase of the polymer was desired to be increased as much as possible and annealing temperatures etc. optimized accordingly. Optimum annealing temperature for copolymers were selected according to the XRD data. Also, for terpolymer and homopolymer, optimal annealing temperatures were decided according to the literature. The synthesis was completed based on the most commonly used process parameters.

In the literature, piezoelectric-piezocatalytic studies of polymer-ceramic composites have been found in general. Polymer used in the composites is PVDF or P(VDF-TrFE) but not P(VDF-TrFE-CTFE). For this reason, as a different study, we aim to compare the piezoelectric and piezocatalytic properties of the terpolymer with homo and copolymer of PVDF. By using piezocatalysis as a relatively new, environmentally friendly promising method, it is aimed to increase the efficiency of removing the RhB dyestuff in water by ultrasonic vibration and generating radicals from the polymer.

## CHAPTER 2

### EXPERIMENTAL

#### 2.1. Fabrication of Polymer Thick Films

Solution casting method was used for the synthesis of polymers. Polymers were manufactured in the form of thick films. The paths followed in the synthesis method used for homopolymer, copolymer and terpolymer are given in Figure 2.1 below.

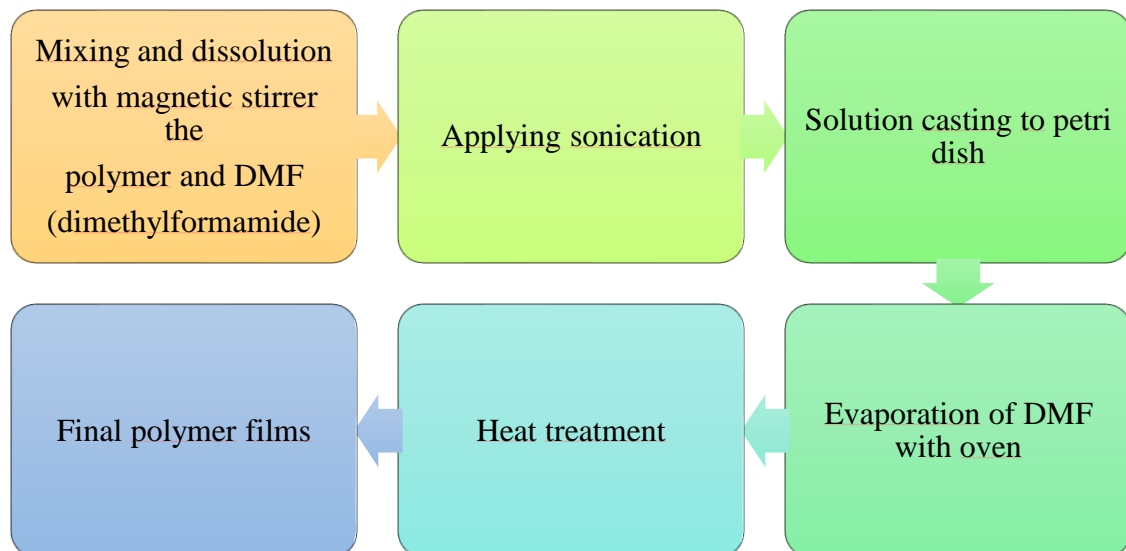


Figure 2.1. Diagram of synthesis method used for homopolymer, copolymer and terpolymer.

##### 2.1.1. Fabrication of PVDF Homopolymer Thick Films

Solution casting method was used for the synthesis of homopolymer PVDF thick films. To synthesize PVDF thick film, 0.25 gram of PVDF polymer powder (PolyK Technologies, USA) was dissolved in 4 ml DMF (Dimethylformamide). This solution was mixed for 24 h at 35 °C using a magnetic stirrer at 500 rpm. Then, the solution was sonicated for an hour in an ultrasonic cleaner (ISOLAB). During sonication, ice was

placed in the sonicator to keep the temperature constant, and any possible degradation of the polymer was prevented. Final mixture was cast in a petri dish. The top of the petri dish was covered with aluminum foil and perforated to ensure homogeneous heat distribution and evaporation while being placed in the oven. In this way, it was transferred to the oven. DMF was evaporated at 50 °C during 1 day in the oven. After, it was annealed at 80 °C for 30 minutes to improve crystallinity and  $\beta$ -phases. Final form of PVDF homopolymer film was obtained.

### **2.1.2. Fabrication of PVDF-TrFE Copolymers Thick Films**

Solution casting method was used for the synthesis of copolymer P(VDF-TrFE) with the composition of 55/45 and 50/50 mol%. To synthesize copolymer thick films, 0.25 gram of P(VDF-TrFE) polymer powders (PolyK Technologies, USA) were dissolved in 4 ml DMF (Dimethylformamide). Same procedure with homopolymer synthesis was applied for mixing and sonication. Only difference is drying and annealing temperature and time. DMF was evaporated at 70 °C during 1 day in an oven. After evaporation/drying, these films were annealed at 140 °C for 3 hours to remove residual solvent and to improve the crystallinity. 140 °C annealing temperature were selected according to the XRD data between 130, 135, and 140 °C according to the intensity of  $\beta$ -phase peak.

### **2.1.3. Fabrication of PVDF-TrFE-CTFE Terpolymer Thick Films**

Solution casting method was used for the synthesis of terpolymer P(VDF-TrFE-CTFE) with the composition of 62/31/7 mol%. To synthesize terpolymer thick film, 0.25 gram of P(VDF-TrFE-CTFE) polymer powders (PolyK Technologies, USA) were dissolved in 4 ml DMF (Dimethylformamide). Same procedure with homopolymer synthesis was applied for mixing and sonication. Only difference is drying and annealing temperature and time. DMF was evaporated at 70 °C during 1 day with oven. After evaporation/drying, these films were annealed at 110 °C for 4 hours to remove residual solvent and to improve the crystallinity.

## **2.2. Characterization of Materials**

The characterization methods used to understand and compare the physical, electrical, and structural properties of homopolymers, copolymers and terpolymers are discussed in this section.

### **2.2.1. X-Ray Diffraction (XRD)**

To determine the crystal structure and phases of the material, X-Ray Diffraction experiments were conducted. These experiments were done at IZTECH Center for Materials Research using a Philips X'pert Pro Diffractometer with Cu-K $\alpha$  XRD patterns were obtained between 10-70° scanning range, and with the 0.02 °/sec (~ 65 min) scanning speed.

### **2.2.2. Scanning Electron Microscopy (SEM)**

To determine the thickness and microstructure of the homopolymer, copolymer and terpolymers, scanning electron microscope was used. Analysis was conducted at IZTECH Center for Materials Research using FEI Quanta 250 FEG. In order to better determine the thickness of the thick films, all films were broken by immersion in liquid nitrogen because if it had been cut with scissors, the thickness would not have been measured accurately due to curling and structural deterioration. In the presence of liquid nitrogen, the polymers are aged for 7-8 seconds and freeze to become more brittle, and the thickness can be accurately determined. And SEM photos were taken with the broken surfaces facing up. In order to obtain clearer images, the broken thick films were coated with gold by sputter coating.

### **2.2.3. Differential Scanning Calorimetry (DSC)**

Differential Scanning Calorimetry (TA Instruments Q10) was used to carry out thermal analysis of the samples. Differential Scanning Calorimetry (DSC) measures the amount of energy absorbed or released as the sample is heated, cooled, or kept at a

constant temperature. In this technique, the temperature difference between the reference and the sample is shown depending on temperature or time. The degree of crystallinity of the materials as well as other thermal parameters like specific heat capacity, phase transition temperature, reaction, and conversion kinetics, are all determined with this analysis.

In this study, DSC measurements were used to determine the melting temperatures, Curie temperatures and degree of crystallinity. The measurement was done between 25-175 °C and 2 °C/min heating rate, and it was cooled to 25 °C with the same rate after waiting at 175 °C for 5 minutes.

#### **2.2.4. Dielectric Measurements**

Dielectric measurements were conducted to determine the electrical properties of the synthesized polymers. Several steps were required for the electrical measurements. First, thick polymer films were cut into small pieces with a length of about 0.5 cm. Silver paste was applied to the center of the pieces in a circle shape (2.5 mm\*2.5 mm) , both on the bottom and on the top, leaving the edges blank. In order to dry the silver paste, it was kept in the oven at 50 °C for 15 minutes, both for the bottom and the top. An example for this prepared polymer sample for measurements is shown in Figure 2.2.



Figure 2.2. Polymer sample with silver paste for electrical measurements.

Dielectric measurements were performed at four different frequencies as 0.1 kHz, 1 kHz, 10 kHz, 100 kHz and between 25- 135 °C and under 1 V AC voltage using LCR

meter (Keysight, E4980AL). All polymers were placed in a sample holder (Aixacct piezo sample holder TFA 423-7) for measurement.

Using a LCR meter, inductance (L), capacitance (C), and resistance (R) of components and circuits at various frequencies can be measured. A change in a conductor's current causes a corresponding change in the conductor's voltage as well as the conductors around it. This feature is referred to as inductance. Capacitance is the ability of a dielectric to store electrical charge. Resistance is the barrier that a conductor makes to the flow of an electric current through it. The impedance of the component or circuit at its terminals is measured by the LCR meter. To do this, a sinusoidal waveform is applied at a certain frequency, and the phase difference between the applied voltage and the resulting current is then measured as shown in Figure 2.3. Following these measurements, this meter determines the impedance. The impedance components can be used to calculate further electrical properties [LCR]. Dielectric constant can be calculated using parallel plate capacitance equation as given in below using the measured capacitance.  $\epsilon_r$ : dielectric constant of material (also called relative permittivity), C: parallel plate capacitance (F), d: distance between two plates (mm), A: surface area of plate(mm<sup>2</sup>),  $\epsilon_0$ : vacuum permittivity/ dielectric constant of free space ( $8.854 \times 10^{-12}$  F/m).

$$\epsilon_r = \frac{C \cdot d}{\epsilon_0 \cdot A} \quad (2.1)$$

In this study, the surface area of the covered silver paste was calculated in mm before the measurement with the help of the ImageJ program. The images were recorded using an USB microscope. The thickness was taken from the SEM analysis determined before the measurement.

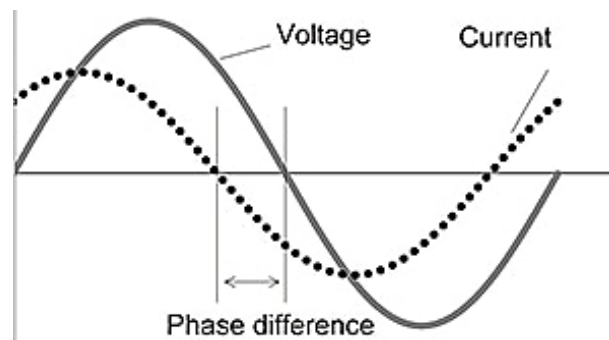


Figure 2.3. Phase difference between the applied voltage and the resulting current <sup>69</sup>

### **2.2.5. Ferroelectric Hysteresis Loop Measurements**

A plot of the charge or polarization (P) created against the field (E) applied to that device/material at a specific frequency is known as a P-E loop. Analyses on the behavior, shape, and polarization values ( $P_S$ ,  $P_R$ ) of the hysteresis loops were done in order to describe the ferroelectric characteristics of the polymers. These Hysteresis loops were measured by using an Aixacct TF Analyzer 1000 connected to TREK 610E High Voltage Amplifier. The measurements were carried out at room temperature with the samples contained in a sample holder that had silicone oil in it. Sample polymers were cut into small pieces with a length of about 2 mm, same as for dielectric measurements. Silver paste was applied to the center of the pieces, both on the bottom and on the top, leaving the edges blank. In order for the silver paste to dry, it was kept in the oven at 50 °C for 15 minutes, both for the bottom and the top.

The surface area of the silver-coated polymer thick films was measured. Thickness and surface area values of the silver-coated samples were used during measurements. The magnitude of the applied voltage to the samples was increased gradually until polarization reaches to saturation. During analysis, temperature was kept constant, at room temperature.

### **2.2.6. Strain Measurements**

A plot of the electric field induced-strain (%) created against the electric field (E) applied to that device/material at a specific frequency is known as a S-E loop for a device or material. These S-E butterfly-shaped plots were determined by using Aixacct TF Analyzer 1000 connected to TREK 610E High Voltage Amplifier. Strain analyzes are carried out using the same instruments simultaneously as piezoelectric hysteresis measurements. The measurements were carried out at room temperature with the samples contained in a sample holder that had silicone oil in it. Sample polymers were cut into circles with a diameter of about 2 mm, same as for piezoelectric hysteresis loop and dielectric measurements.

### 2.2.7. Piezocatalytic Property Measurements

Piezocatalytic experiments were performed to evaluate the removal and degradation efficiency of polymers on aqueous solutions containing Rhodamine B, a dyestuff in water. Rhodamine B is a dye and chemical compound. It is used as a tracer dye to determine the transfer, flow direction and velocity in water.

A total of three devices were used for this experiment. Sonicator with probe tip with 25 kHz frequency and 200 W power (Nanolinker Ultrasonic Homogenizer NL650) is used to carry out the degradation reaction. UV-Visible Spectrophotometer (Thermoscientific Genesys 150) is used to determine piezocatalytic degradation performance and absorption spectrum of dye solution. Finally, the centrifuge device (Nuve NF800) was used so that the polymers degraded after sonication would not interfere with the measurement in the UV-Visible Spectroscopy. This set up was used at the laboratory established by Dr. Aziz Genç during his work at IZTECH.

In piezocatalytic property analysis, Rhodamine B solution about 40 ml at a concentration of 0.01 mg/mL was prepared and taken into a beaker. About 20 mg of polymer was cut into a rectangular shape (approximately 1 cm x 2 cm), and this polymer-RodB solution was put into a magnetic stirrer. In the first step, to reach adsorption-desorption equilibrium, the glass beaker was left in the dark box for 30 minutes. Then, the probe tip of the sonicator was immersed in this beaker for about 2 cm in order to provide controlled ultrasonic wave propagation, and the degradation processes were started. Starting from minute 0, 4 ml samples were taken every 15 minutes for approximately 90 minutes and sent to the centrifuge. The sample taken from the centrifuge was analyzed in the UV-Visible Spectrophotometer. Experiments on the sonicator were performed in a dark environment for 90 minutes to avoid influence from outside light. In order to prevent the solution from heating up during the experiment, a pumped circulation system was set up using ice cubes and water as shown in the Figure 2.4 below and the temperature of the solution was tried to be kept constant at room temperature ( $25\text{ }^{\circ}\text{C} \pm 3\text{ }^{\circ}\text{C}$ ).

According to the results obtained from the UV-Visible Spectrophotometer, the degradation rate (%) or dye degradation achieved (%) can be calculated using the following formulas.

$$\text{dye degradation (\%)} = \left(1 - \frac{C}{C_0}\right) \times 100 = \left(1 - \frac{A}{A_0}\right) \times 100 \quad (2.2)$$

where  $A$  and  $A_0$  is the absorbance peak intensity values,  $C$  and  $C_0$  is the concentration values of the dye solution at the time “ $t = t \text{ min}$ ” and “ $t = 0 \text{ min}$ ”, respectively, during the piezocatalytic experiment.



Figure 2.4. Experimental water circulation set-up for the sonicator.

## CHAPTER 3

### RESULTS AND DISCUSSION

#### 3.1. X-Ray Diffraction (XRD) of PVDF, P(VDF-TrFE) and P (VDF-TrFE-CTFE)

The XRD patterns of homopolymer, copolymers and terpolymer were obtained at room temperature. In order to compare the polymers easily, all of XRD patterns were represented in a graph. According to the patterns, some characteristic peaks for the polymers were obtained. These peaks are at  $2\theta$ :  $19^\circ$  and  $18.68^\circ$  belonging to (110) and (200) planes. (110) planes indicate  $\beta$  (polar) phase which has ferroelectric property, while (200) planes indicate alpha (non-polar) phase <sup>70</sup>. So, in these experiments,  $\beta$  crystalline phase was predominantly obtained.

The data in Figure 3.1 and Figure 3.2 show that the interchain lattice distance of terpolymer is larger than that of the copolymer. The d spacing value for a plane can be calculated by using Bragg's Law:  $\lambda=2d\sin\theta$ . For copolymers, interchain distance concluded from (200,110) reflection is about 4.60 Å, while the space for terpolymer is 4.84 Å. So, it can be explained as that the ferroelectric domains are interrupted by the addition of a third monomer with a larger size, which increases inter-chain distance and reduces the size of the ferroelectric domains. So, third monomer acts as a defect for copolymers. As a result of the introduction of CTFE monomer, loosely packed helical chains with TGTG and TTTG conformations were obtained from the closely packed planar all-trans conformations in the  $\beta$  phase <sup>71</sup>. In addition, with decrease of VDF content from 55 to 50 mol%, the characteristic peak which is (200,110), shifts from  $19.3^\circ$  to  $19^\circ$ . It can be attributed that increasing d spacing with TrFE content <sup>72</sup>.

For homopolymer, while peak at  $18.8^\circ$  indicates alpha phase of polymer, the peak at  $20.87^\circ$  indicates the  $\beta$ -phase. The homopolymer consisted predominantly of the  $\beta$ -phase with the method used as can be seen from the XRD patterns for homopolymer. This is because that DMF solvent, which was used in synthesis for polymers, has dipole moment. These dipole moments are responsible for producing  $\beta$ -phase for pristine PVDF

<sup>73,74</sup>. Moreover, peaks at  $37.16^\circ$  and  $39.87^\circ$  corresponds to gamma phase (Figure 3.1 and Figure 3.2). These XRD results indicates that PVDF homopolymer film was formed mixed with alpha,  $\beta$ - and  $\gamma$ - phases.  $\alpha$ ,  $\beta$  and  $\gamma$  phase distribution may differ from process to process because of the viscosity of the solution, polarity of the solvent and the induced thermal energy, etc. <sup>36</sup>.

In addition, peak splitting was observed for copolymers. More peak splitting was observed in copolymer 50/50 mol% compared to the 55/45 mol% copolymer. These obtained results are consistent with the results in the literature. According to the literature, copolymers containing less VDF than 55 mol%, these types of peak splitting were observed. Such behavior can be attributed to the trans-planar phases at a high  $2\theta$  diffraction angle and to the 3/1-helical phase at a low  $2\theta$  <sup>38</sup>.

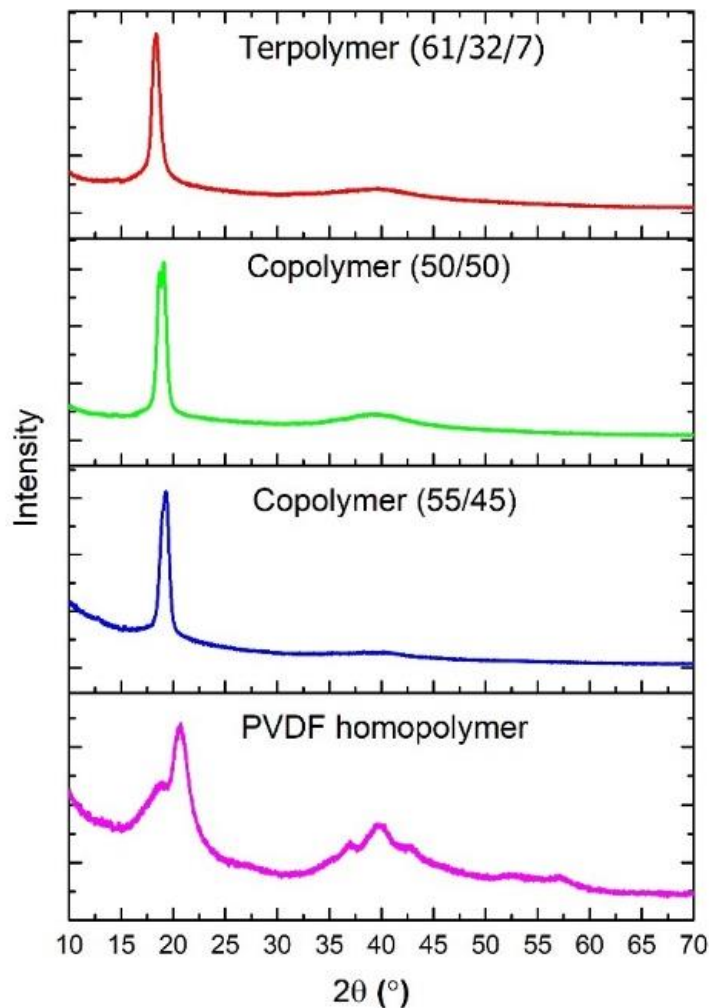


Figure 3.1. X-ray diffraction patterns of homopolymer, copolymers and terpolymer.

Moreover, annealing temperatures for copolymers were selected according to the condition in which the peak of the  $\beta$  had the highest intensity because the piezoelectric properties increase in the  $\beta$ -phase. XRD data for copolymers synthesized at the annealing temperatures of 130, 135, 140 °C, is given in Figure 3.3. As can be seen at 140 °C annealing temperature,  $\beta$ -phase intensity was higher compared to other annealing temperatures. In addition, it was observed that increasing annealing temperature also increased the gamma-phase. So, in this study, copolymers 55/45 and 50/50 were annealed at 140 °C to improve the crystallinity.

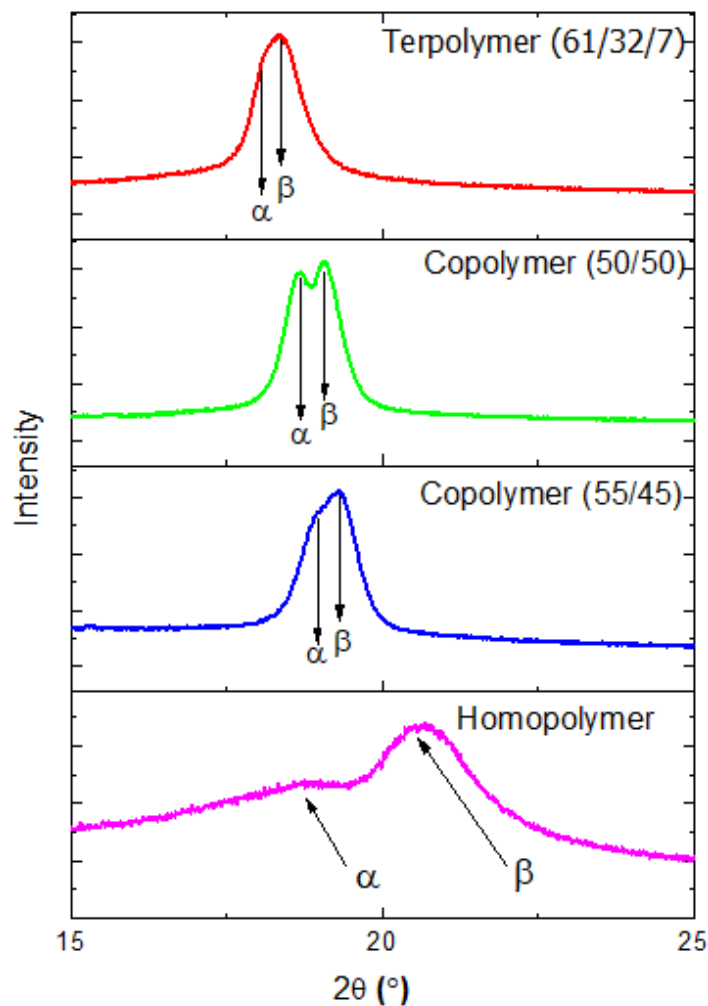


Figure 3.2. X-ray diffraction patterns of homopolymer, copolymers and terpolymer between 15-25°.

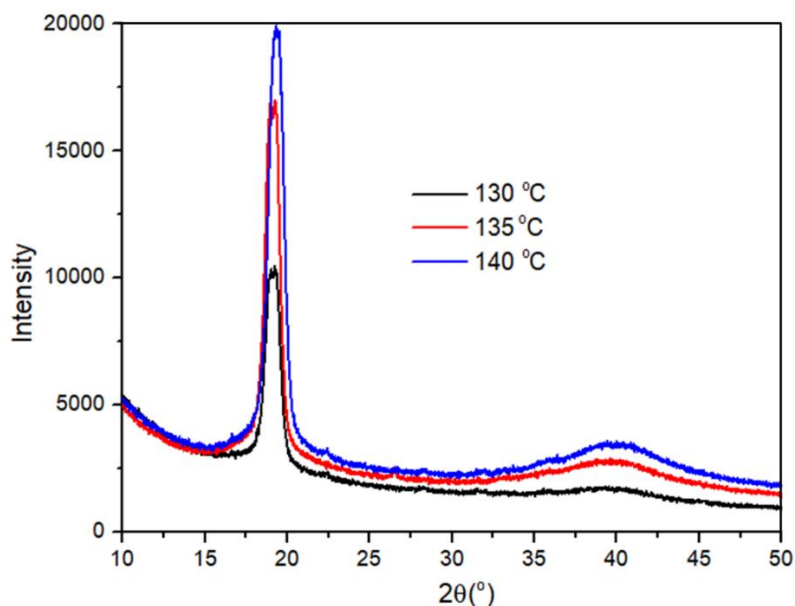


Figure 3.3.  $\beta$ -phase intensity comparison at different annealing temperatures copolymers.

### 3.2. Scanning Electron Microscopy (SEM) of PVDF, P(VDF-TrFE) and P(VDF-TrFE-CTFE)

SEM images of four types of polymers were used to determine morphology and microstructure. To measure the thickness of the polymer films, cross section images also were taken. The Everhart-Thornley Detector (ETD) (secondary electron detector) was used for SEM image acquisition for PVDF-homopolymer (Figure 3.4). Circular Backscatter Detector (CBS) was used for image acquisition for terpolymer and copolymers. Because in this way, clearer images were obtained (Figure 3.5, Figure 3.6, and Figure 3.7). For example, when ETD was used in the terpolymer, their network-like structure could not be clearly observed at the same magnification.

While homopolymer PVDF had about 62  $\mu\text{m}$  thickness, terpolymer and copolymers had approximately 33  $\mu\text{m}$  and 40  $\mu\text{m}$  thickness, respectively. Copolymer (55/45) mol% and (50/50) mol% can be considered as having almost the same thickness. All polymers have a homogeneous thickness distribution across the cross section. Cross section images of polymer thick films can be seen from the Figure 3.8.

An orderly structure can be observed from all the polymers. The amount of crystallization appears to be quite sufficient for all polymers compared to the literature<sup>75</sup>.

Terpolymer and copolymers had elongated fibrillar-like crystallites, as shown in Figure 3.5 and Figure 3.6, Figure 3.7 respectively. These polymer networks are fibre-like. Especially terpolymer looks like a honeycomb. The honeycomb-like appearance is created by the retraction of the fibrils in the direction parallel to the substrate during solvent evaporation <sup>76</sup>.

In addition, while all polymers have a dense structure, homopolymer has a more porous structure compared to other polymers, as shown in Figure 3.4, PVDF homopolymer film composed of many fused particles, a porous structure between the fused particles, with an average particle size of 7  $\mu\text{m}$  and average pores size of 10  $\mu\text{m}$ .

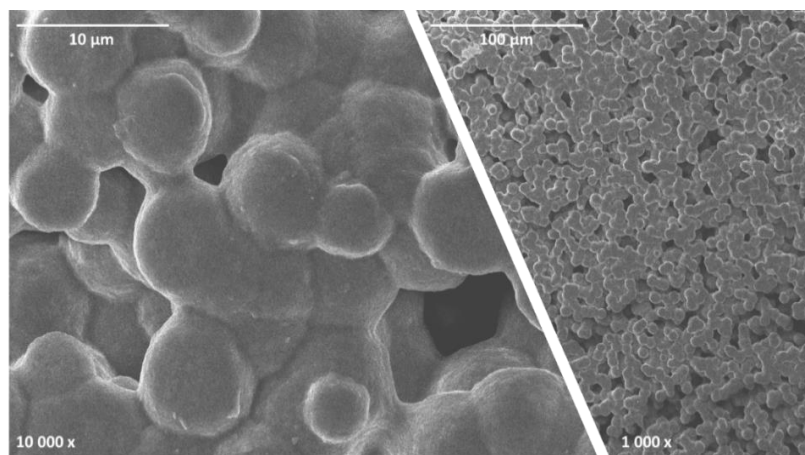


Figure 3.4. SEM images of homopolymer PVDF.

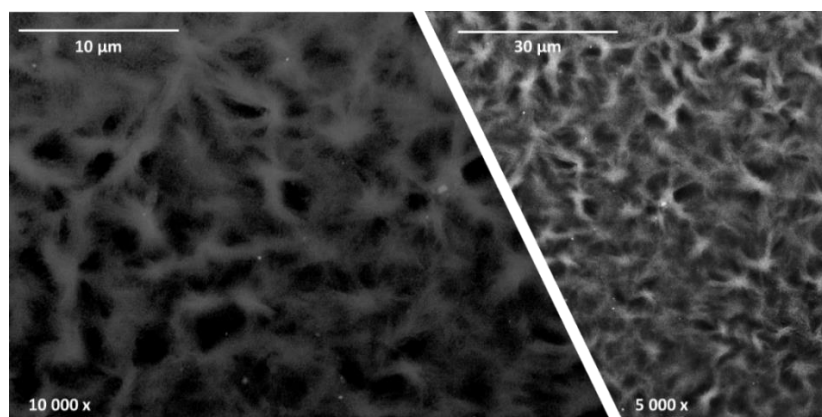


Figure 3.5. SEM images of terpolymer P(VDF-TrFE-CTFE) (61/32/7).

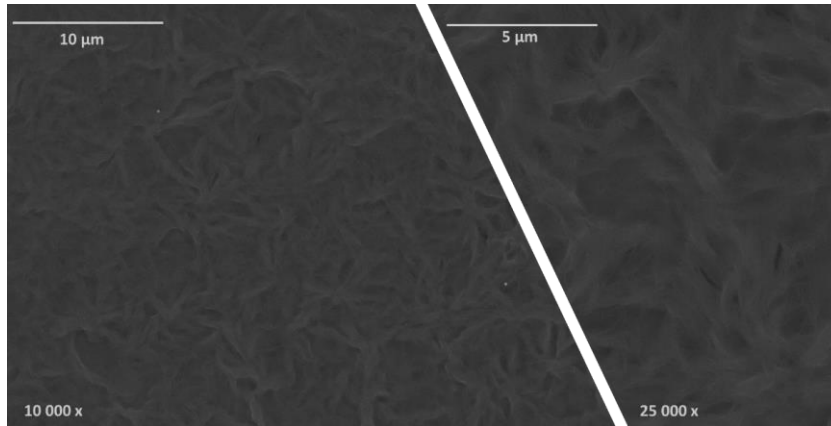


Figure 3.6. SEM images of copolymer P(VDF-TrFE) (55/45).

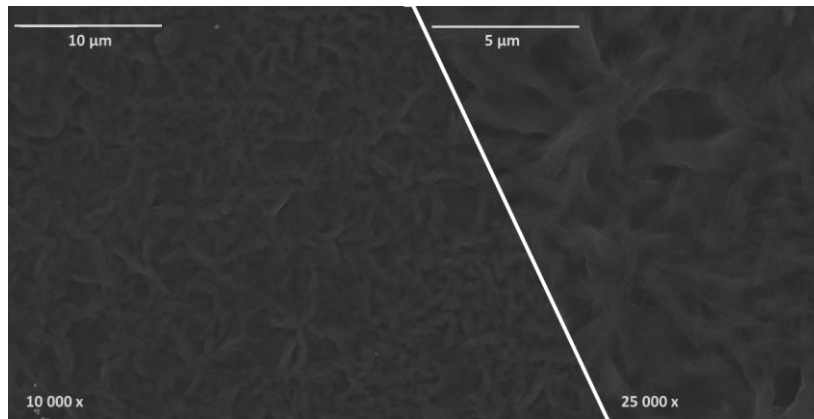


Figure 3.7. SEM images of copolymer P(VDF-TrFE) (50/50).

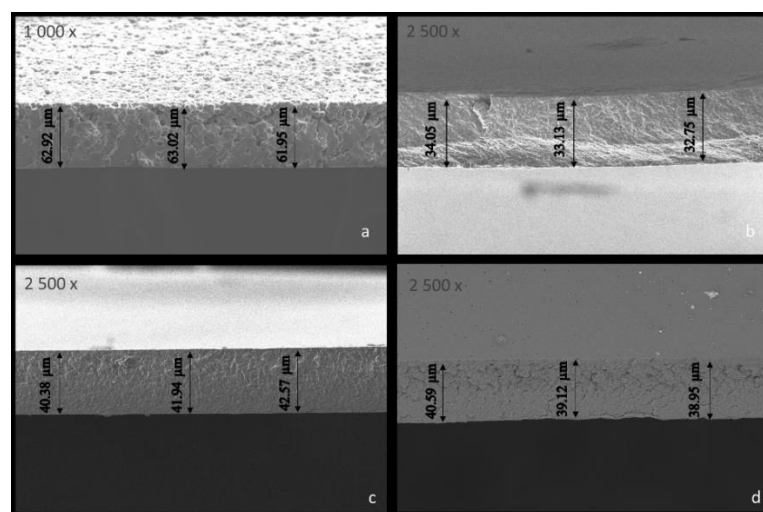


Figure 3.8. Cross section SEM images of a) homopolymer, b) terpolymer, c) 55/45 copolymer, d) 50/50 copolymer.

### 3.3. Differential Scanning Calorimetry (DSC) of PVDF, P(VDF-TrFE) and P(VDF-TrFE-CTFE)

Differential Scanning Calorimetry (DSC) measures the amount of energy absorbed or released as the sample is heated, cooled, or kept at a constant temperature. The degree of crystallinity and phase transition temperature can be determined with the help of the DSC analysis. In our experiments, the higher temperature and lower temperature peaks can be attributed to the melting point of the crystallites and the ferroelectric-to-paraelectric phase transition (Curie transition), respectively.

The DSC curves of homopolymer, terpolymer and copolymers can be seen from the Figure 3.9. The addition of TrFE into PVDF affects the thermal stability of the polymers. For copolymers with the composition of 55/45 and 50/50 mol%, melting temperature,  $T_m$ , increased from 156.8 °C to 160.3 °C, respectively. However, with increasing TrFE content, Curie point ( $T_C$ ) decreased from 64.6 °C to 59 °C for copolymers with the composition of 55/45 and 50/50 mol%, respectively. Phase transition (ferroelectric-to-paraelectric) was not observed for homopolymer and terpolymer as expected, because the homopolymer melts before ferroelectric-to-paraelectric phase transition and terpolymer shows relaxor ferroelectric behavior with no ferroelectric-paraelectric phase transition. Moreover, the lowest  $T_m$  was observed in terpolymer, and it is usually induced due to smaller crystalline size of the terpolymers<sup>77</sup>.

Considering all these obtained data, it was seen that similar results were obtained with those in the literature. According to the literature, melting points of copolymers are between 150-160 °C<sup>38,78-80</sup> which is close to melting temperature of our copolymers. For homopolymer PVDF, melting points are between 165-170 °C<sup>79,81-83</sup>. In addition, the same similarity with the literature was observed for the terpolymer melting point. As in our study, values in the literature were between 120-130 °C<sup>84-86</sup>.

If it is desired to obtain an experimental crystallization percentage ( $X_c$ ) from DSC curves, the following formula can be used<sup>87-89</sup>:

$$X_c \% = \frac{\Delta H_f}{\Delta H_{100}} \times 100 \quad (3.1)$$

where  $\Delta H_f$  is the enthalpy of the melting and  $\Delta H_{100}$  is the is enthalpy of the fully crystallized polymer.  $\Delta H_f$  values were determined experimentally from the DSC curves (area under melting peaks).  $\Delta H_{100}$  values were taken from the literature. For homopolymer and terpolymer enthalpy values were taken directly. Copolymer enthalpies were estimated according to the contents of VDF and TrFE. Respective values of 100% crystalline PVDF and PTrFE were given as 104.6 J/g and 66.3 J/g, respectively <sup>90</sup>. From these data, enthalpy of 55/45 and 50/50 mol% P(VDF-TrFE) copolymers were calculated approximately. Using all these data and the above formula, the approximate estimated crystallinity percentage for each polymer are listed in the Table 3.1 below.

Table 3.1. Approximate estimated crystallinity percentage for each polymer.

Polymers	$\Delta H_{100}$ , J/g (From literature)	$\Delta H_f$ , J/g	$X_c$
Copolymer (50/50)	86.45 <sup>91</sup>	23.8	27%
Copolymer (55/45)	88.43 <sup>91</sup>	28.4	32%
Homopolymer	104.6 <sup>90</sup>	18.7	18%
Terpolymer	42 <sup>88</sup>	4.4	10%

The estimated crystallization amounts calculated were in agreement with the literature <sup>92</sup>. For copolymers, with increasing TrFE content, crystallinity decreases. It can be understood also from the sharpness of the DSC curve peaks. The 55/45 copolymer had a sharper melting point than that of 50/50 <sup>93,94</sup>. In terpolymers, as can be seen again from the DSC curves, terpolymer had more broad melting peak than other polymers. The addition of CTFE does not affect the crystallinity of the sample much in terpolymers. Thinner crystalline lamellae are produced because of CTFE units acting as defects to restrict extent of crystallization <sup>95</sup>.

There is a lot of literature supporting this situation. Qing Liu et al. (2016) <sup>96</sup> states that with the addition of bulky ternary monomer CTFE, the crystallinity will decrease. Claude Richard et al. (2017) <sup>97</sup> suggested that the crystal fraction would be greatly reduced in the presence of CTFE in the PVDF-TrFE backbone. Additionally, Sudarshan et al. (2023) <sup>98</sup> states that optical transmission is increased in the terpolymer, which is a result of low crystallization. François Bargain et al. (2020) <sup>99</sup> obtained a DSC curve very close to ours, which is indicative of low crystallinity in the terpolymer. So, according to

the experimental crystallization percentages ( $X_c$ ) from DSC curves, terpolymer crystallization was found very low. This can also be because of the  $\Delta H_{100}$  values which taken from literature, which may not be very reliable.

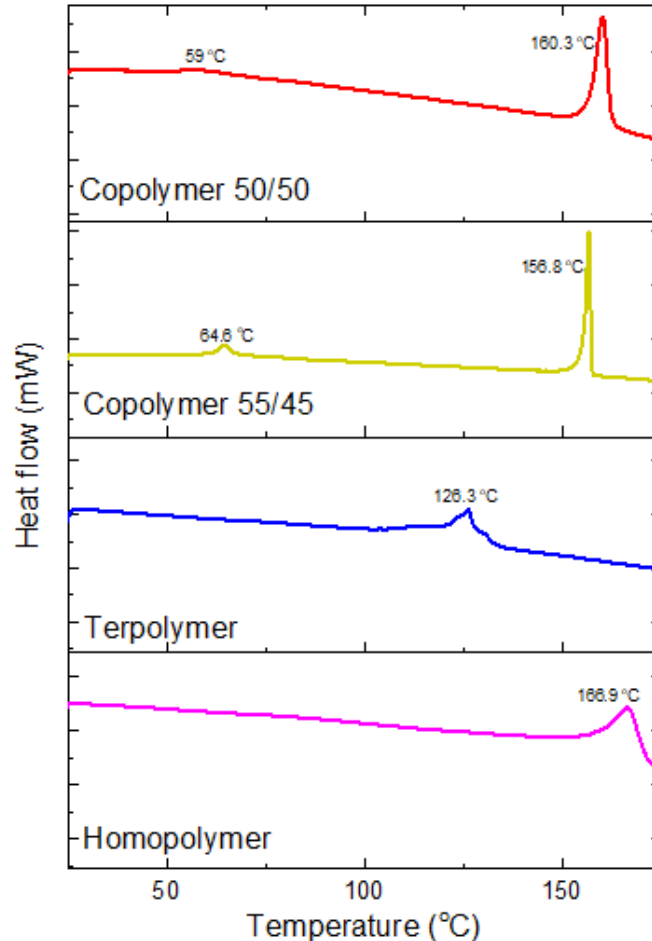


Figure 3.9. The DSC heating curves of homopolymer, terpolymer and copolymers.

### 3.4. Dielectric Properties of PVDF, P(VDF-TrFE) and P(VDF-TrFE CTFE)

To determine electrical properties of polymers, dielectric measurements were conducted. Dielectric measurements were performed at four different frequencies as 0.1 kHz, 1 kHz, 10 kHz, 100 kHz and between 25- 125 °C. Dielectric constants of polymers were calculated using parallel plate capacitor equation as given in previous sections. The thickness was obtained from the SEM analysis determined before the measurement.

Figure 3.11 shows dielectric constant versus temperature graphs for each polymer at 0.1 kHz, 1 kHz, 10 kHz, 100 kHz. Copolymers (55/45 and 50/50 compositions) and terpolymer had a net phase transition from ferroelectric to paraelectric at Curie temperature.  $T_c$  (Curie temperature) of 55/45 mol% copolymer was determined approximately as 73 °C from where dielectric constant maximum. Since dielectric behavior of 50/50 mol% copolymer is frequency dependent, it has no net  $T_c$  point. Its  $T_c$  value was determined between 68-74 °C.

55/45 copolymer transition temperature does not shift with increasing frequency. So, it can be said that 55/45 copolymer is normal ferroelectric and not relaxor ferroelectric. However, an increasing frequency dependent behavior was observed in the terpolymer as indicated by the arrow in the Figure 3.11. Therefore, the terpolymer showed relaxor properties as expected. In addition, the 50/50 copolymer exhibited a behavior between the terpolymer and 55/45 copolymer behavior. In other words, a behavior between normal ferroelectric and relaxor ferroelectric. Rather than in the amorphous regions, the dielectric response around  $T_m$  is caused by molecular movements in the crystalline regions. Consequently, within the transition region ( $49 \text{ mol}\% \leq C_{\text{VDF}} \leq 55 \text{ mol}\%$ ) of P(VDF-TrFE), both normal-ferroelectric and relaxor characteristics can be observed<sup>38</sup>, as shown in Figure 3.10 below.

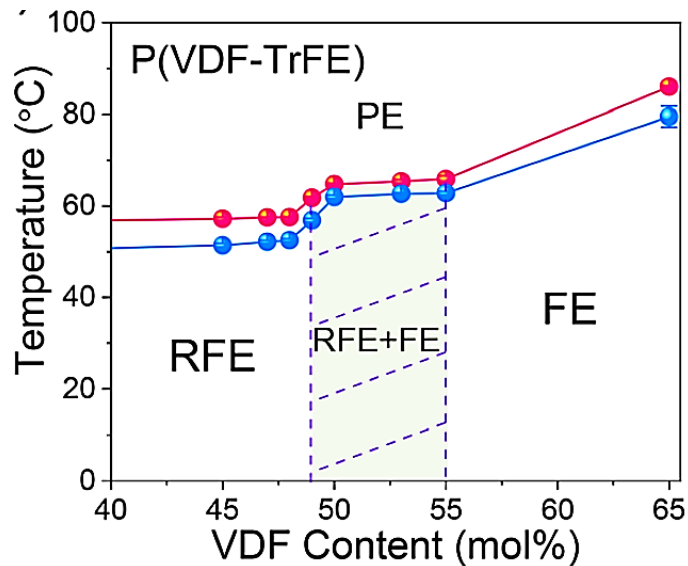


Figure 3.10. Relaxor ferroelectricity (RFE)/ ferroelectricity (FE) with VDF content<sup>30</sup>.

Moreover, the dielectric constant versus temperature graph drawn for the terpolymer showed a broad peak close to the room temperature. Because in the experimental setup we used, it was not possible to go down to negative temperatures. If it could be reduced to negative temperatures, a curve like that of copolymers would be obtained.

Maximum dielectric constant is obtained at Curie temperature region. Generally speaking, the polymer with the highest maximum dielectric constant was obtained as a terpolymer as shown in Figure 3.11 and Figure 3.12. As already mentioned, smaller crystallite size would improve the dielectric properties of terpolymer. After the terpolymer, the dielectric constant value of the 50/50 copolymer was highest. In agreement with the literature, the dielectric constant of the 55/45 copolymer is lower than that of 50/50. As the VDF content increases, the dielectric constant decreases after a point<sup>30</sup>. In homopolymer PVDF, Curie temperature is higher than the melting point of PVDF<sup>30</sup>. So that, maximum dielectric constant peak was not observed in homopolymer. It melts before the ferroelectric-paraelectric phase transition occurs.

T<sub>c</sub> (Curie temp.), which is the ferroelectric-paraelectric phase transition point, is determined from the point where the dielectric constant is maximum and the peak occurring at low temperature of the DSC graphs. From DSC, T<sub>c</sub> of 50/50 and 55/45 copolymer were found as 61.3 °C and 65 °C, respectively. From dielectric constant versus temperature graph T<sub>c</sub> of 50/50 and 55/45 were about 68-74 °C and 73 °C, respectively. It is normal to have two different T<sub>c</sub> values which very close to each other from these two different characterizations. It was noticed that obtaining different results from such different characterization techniques is a common situation in the literature<sup>79,80</sup>.

In addition, dielectric loss versus temperature graphs in Figure 3.13 is given. Above the Curie temperature, dielectric loss increased for 0.1 kHz and 1 kHz. At higher frequency range, dielectric loss remains constant and approximately was zero.

Considering all these obtained data, it was seen that similar and close results were obtained with those in the literature. For homopolymer PVDF, dielectric constant was not change with temperature as in the literature. The dielectric constant at room temperature for the homopolymer PVDF was found to be about 20. However, according to a paper, the PVDF dielectric constant (~5) was lower than that obtained in our study<sup>79</sup> This difference may be due to differences in process parameters. There isn't much of a difference anyway. According to another research paper, its dielectric constant (~25)

which is larger than the dielectric constant obtained from this study. <sup>36</sup>. For copolymers 50/50 and 55/45, dielectric constants at room temperature were found as (@10 kHz) ~ 30 and ~27, respectively. According to one study, the PVDF-TrFE copolymer with a composition of 52/48 had a value of 20 <sup>80</sup>, while in other studies, the dielectric constants of the copolymer at room temperature with a composition of 50/50 was 15 <sup>79</sup>, 49/51 was 20 <sup>38</sup>.

In addition, Tc values for 50/50 and 55/45 copolymers in the literature were approximately the same (~70 °C) <sup>38</sup>. According to another research, Tc for 50/50 copolymer was (~80 °C) <sup>79</sup>. Therefore, our experimental results are in agreement with the literature. It can be thought that the minor differences might originate from the process parameters.

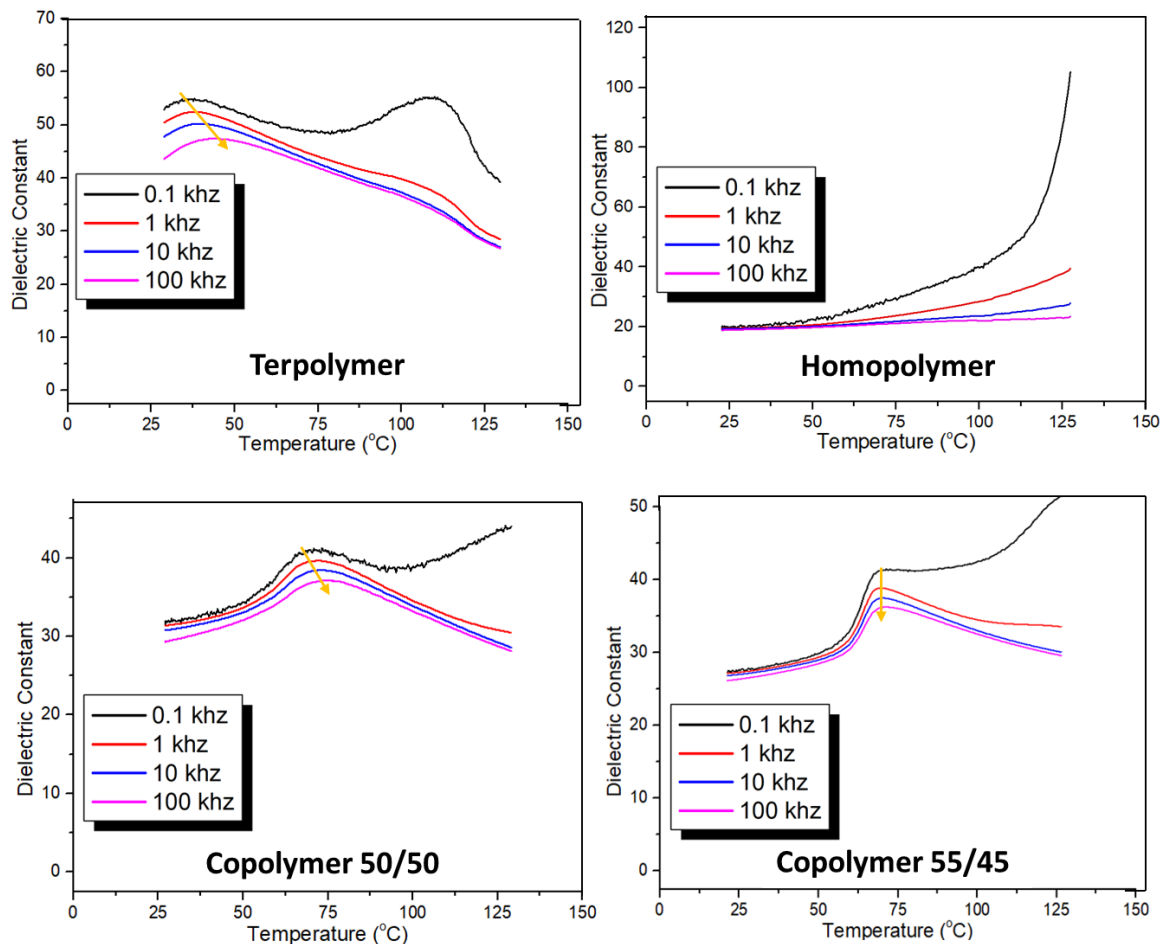


Figure 3.11. Dielectric constant versus temperature at different frequencies for all polymers.

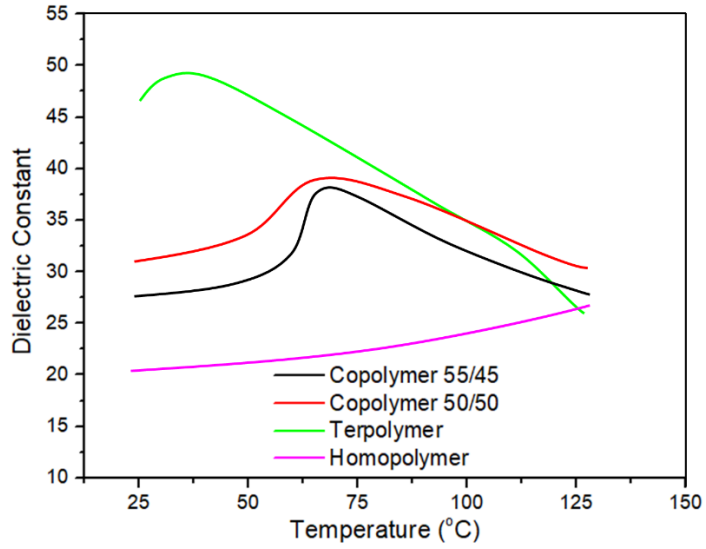


Figure 3.12. Comparison of dielectric constant for homopolymer, terpolymer and copolymers at 10 kHz.

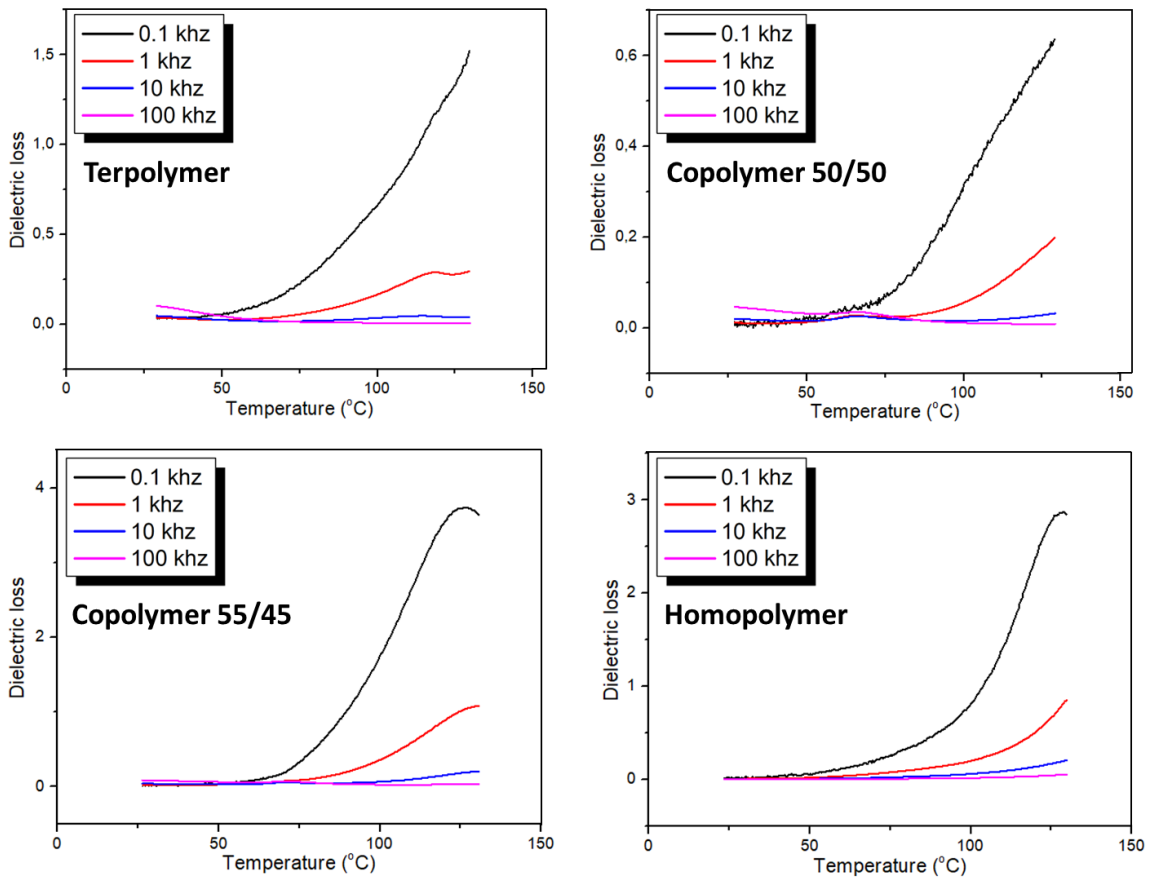


Figure 3.13. Dielectric loss versus temperature graphs for synthesized polymers.

### 3.5. Ferroelectric and Piezoelectric Properties of PVDF, P(VDF-TrFE) and P(VDF-TrFE-CTFE)

P-E graphs (hysteresis loops) measured at room temperature are shown in Figure 3.14. Clearly, a slim hysteresis loop which has very low remanent polarization and low coercive field was observed as expected for the terpolymer. Its maximum polarization was relatively high  $11 \mu\text{C}/\text{cm}^2$ . At the place of purchase of the polymers (PolyK/USA), according to the information provided <sup>100</sup>, saturation polarization value of terpolymer were given as  $10 \mu\text{C}/\text{cm}^2$  at the same electric field. According to another research, saturation polarization was approximately  $6 \mu\text{C}/\text{cm}^2$  <sup>77</sup> and  $8 \mu\text{C}/\text{cm}^2$  <sup>101, 102</sup>. As mentioned earlier, difference between synthesis processes can cause these differences. According to the results of this study, the obtained hysteresis loops are not fully saturated. This condition is also similar to most results in the literature <sup>100</sup>.

As we know, the terpolymer has a smaller crystalline size. The terpolymer is a semicrystalline and the polarization response of the terpolymer is mainly due to its crystalline phase. Smaller crystal size can reduce the energy barrier for dipole orientation in the terpolymer, resulting in greater polarization <sup>77</sup>. This feature can also cause a higher EC (electrocaloric) effect in low electric fields.

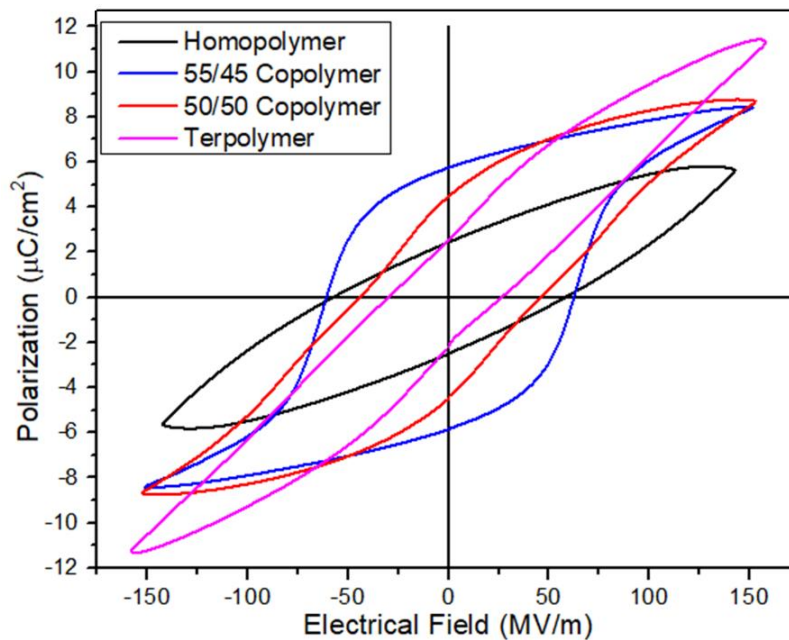


Figure 3.14. Hysteresis loops (P-E) for homopolymer, terpolymer and copolymers.

The P-E loops for both copolymers are saturated. Copolymer 50/50 mol% and 55/45 mol% had the polarization values of  $9 \mu\text{C}/\text{cm}^2$  and  $8.3 \mu\text{C}/\text{cm}^2$ . In other studies, in the literature, 50/50 mol% copolymer polarization values are close to our results. Liu Y. et al (2018) were obtained a value of maximum polarization  $6 \mu\text{C}/\text{cm}^2$ <sup>38</sup>, while  $7 \mu\text{C}/\text{cm}^2$  was obtained according to another research<sup>103</sup>. In addition, 55/45 mol% copolymer polarization values were found as similar to those in the literature<sup>38,103</sup>. In general, when compared under the same electric field, the polarization values obtained from our experimental results were slightly higher than those in the literature.

While the saturation polarization of the 50/50 mol% copolymer was just a little higher, the polarization values of both copolymers were very close to each other. However, the coercive field of the 50/50 mol% copolymer was found much lower ( $\pm 25.5 \text{ kV}/\text{cm}$ ). This value had the same coercive field value as the terpolymer. 50/50 mol% copolymer had similar properties with the terpolymer, such as coercive field values and frequency dependence in dielectric measurements. From this point of view, if the VDF content falls below 50%, the transition from normal ferroelectricity to relaxor begins. In addition, the pure homopolymer PVDF was measured as having the lowest polarization value,  $5.75 \mu\text{C}/\text{cm}^2$ .

Results showed that the composition of TrFE affects ferroelectric/piezoelectric properties of the polymers. Increasing the TrFE content caused the increase in the polarization because bulky TrFE group provides the larger interchain distance in copolymer and dipole moments can more easily rotate in copolymers<sup>28</sup>.

In Figure 3.15 and Figure 3.16, electric field, and frequency dependent polarization hysteresis loops of the terpolymer are shown, respectively. According to the graph in Figure 3.15, at 90 Hz, maximum polarization increased non-linearly with increasing applied electric field during measurements. This is to be expected and shows domain wall motion<sup>104</sup>.

In Figure 3.16, terpolymer hysteresis loops are shown at different frequencies, at a fixed voltage of 3 kV. At high frequencies, it was observed that the coercive field and remanent polarization decreased. In the graph comparing all the polymers, the graph obtained at 150 Hz was used for the terpolymer. Because as the frequency increases, the frequency dependence of the terpolymer decreases, which indicates that the potential conductivity contribution decreases<sup>105</sup>. For example, it can be seen that the shape of the

graph does not change much when going from 70 Hz to 90 Hz. From here, we observe the intrinsic behavior of the terpolymer.

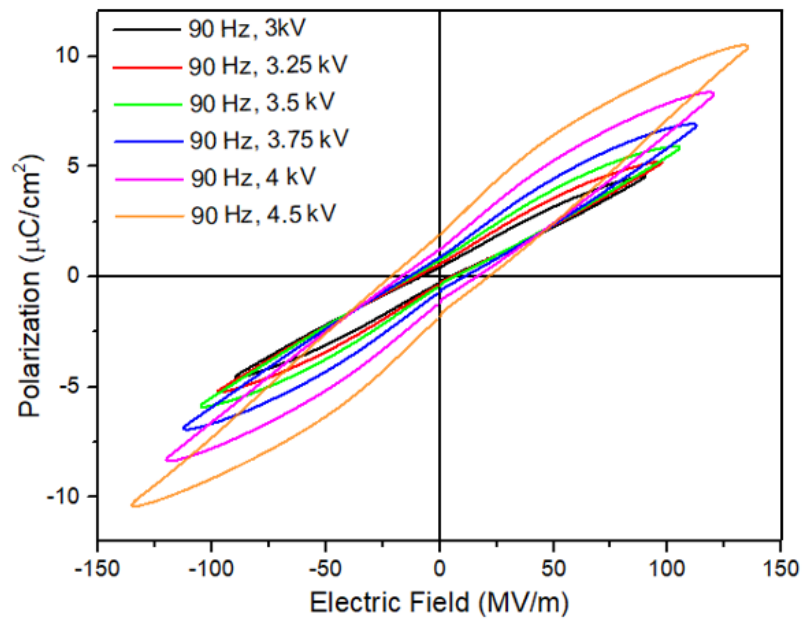


Figure 3.15. Terpolymer hysteresis loops at 90 Hz, and between 3 kV and 4.5 kV electric fields.

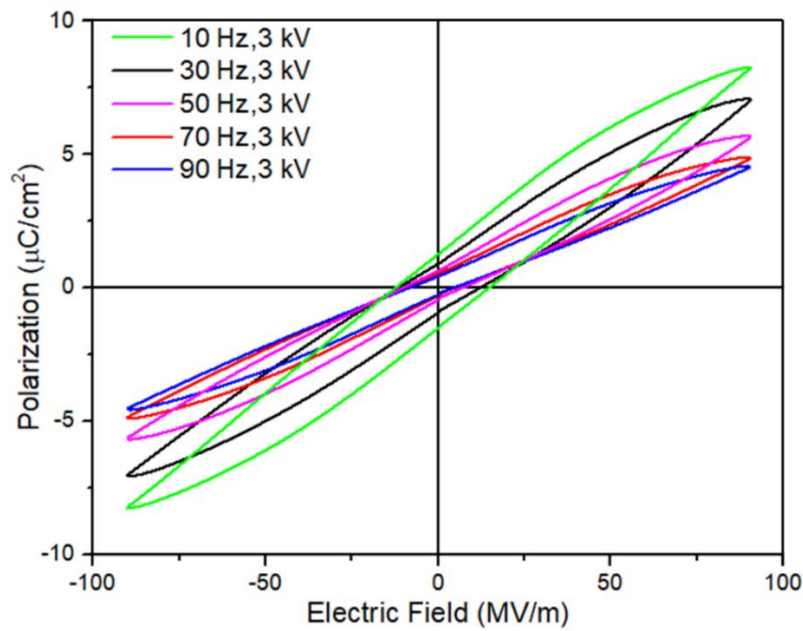


Figure 3.16. Terpolymer hysteresis loops at 3 kV, between 10 Hz and 90 Hz.

### 3.6. Strain Characteristics of PVDF, P(VDF-TrFE) and P(VDF-TrFE-CTFE)

Since it was not possible to use specific type of poling process for the polymers called corona poling,  $d_{33}$  of the polymers could not be measured. Therefore, to assess and compare the piezoelectric response of the polymers, field-induced strain curves were measured. Before discussing the results, the origin of the inverse butterfly shaped strain curves will be introduced first. As a result of the strain measurements, all polymers showed inverse butterfly shaped curves. A strain cycle with a butterfly-like shape is a result of three main factor: normal converse piezoelectric effect of the lattice, due to switching and domain walls movement. In butterfly shape, with applied field, strain starts to increase and get saturated. After that, applied electrical field is gradually decreased, so the strain cannot follow the same curve/line. Strain remains in the material when electric field is zero. The strain is zero at a specific negative electric field if the electric field is increased in the opposite direction. The strain increases and reaches saturation if the electric field is now increased in the same direction. As a result, converse butterfly symmetric curve is obtained <sup>4,14</sup>, as can be seen in the graph in Figure 3.17 below, based on the experimental results.

From Figure 3.17, terpolymer P(VDF-TrFE-CTFE) has the highest strain and only negative strain. The addition of termonomer to the copolymer was shown to cause increased strain in the negative direction in the literature <sup>106</sup>. The high strain of terpolymers is associated with their relaxor ferroelectric nature. Decrease in crystalline domain size causes this relaxor characteristic which leads to the frequency dependent dielectric maxima. It can be said that the impact of CTFE is a decrease in ferroelectricity and increase in relaxor behavior. So, introducing defects (CTFE) improves properties e.g., electromechanical response (strain characteristics). The difference in lattice between the two conformations would cause the phase transition to generate a strain in the material <sup>107,108</sup>.

Homopolymer has the lowest strain while copolymers and terpolymer have higher strain values respectively. So, the addition of TrFE and CTFE monomers enhanced the strain as in the literature <sup>106</sup>. The homopolymer had strain values of 0.05%, while the copolymer 50/50 mol% had strain value of 3% and 55/45 mol% had strain value of 1%. The strain value of the terpolymer is 5.6%.

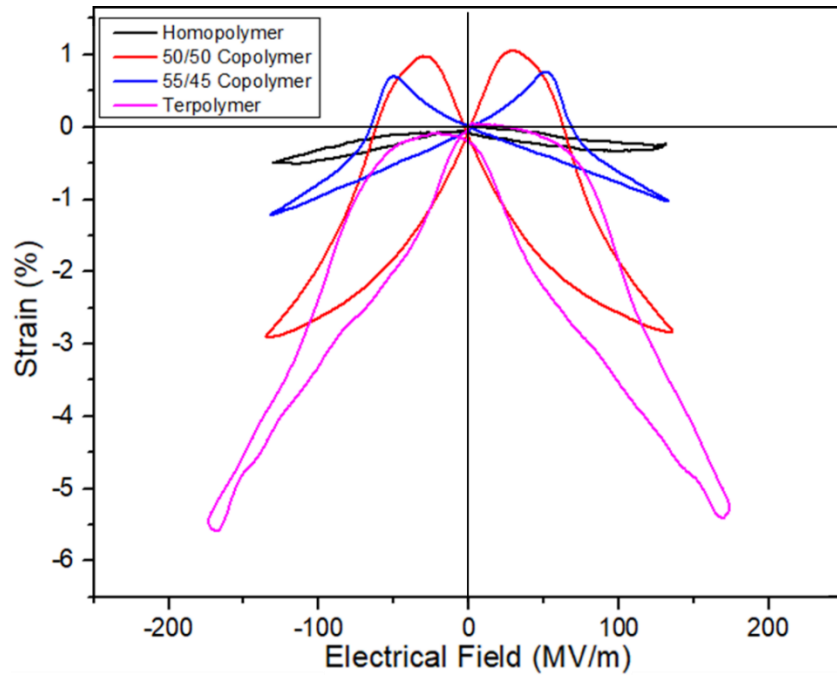


Figure 3.17. Strain characteristics (S-E) of homopolymer, terpolymer and copolymers.

In summary, when CTFE contents increase, polymers' molecular chain distance and molecular chain flexibility also increase. As a result, ferroelectric domain size decreases and the dipole orientation is facilitated. So, large strain is obtained under the lower electric field <sup>109</sup>.

In addition, as mentioned before, although piezoelectric coefficients are positive for all piezoelectric ceramics, PVDF and its copolymer/terpolymer exhibit negative piezoelectric coefficient. This is due to contraction with applied electric field of both the crystalline and the amorphous part of the semicrystalline polymers because there is an electromechanical connection between intermixed crystal lamellae and amorphous regions. In other words, the situation is due to the composite internal microstructure of polymers <sup>24</sup>. Because of these reasons, while piezoelectric ceramics have positive normal butterfly-shape strain graph, PVDF and its copolymer/terpolymer have converse butterfly-shape strain graph.

### 3.7. Piezocatalytic Properties of PVDF, P(VDF-TrFE) and P(VDF-TrFE-CTFE)

The piezocatalytic performances of polymer samples were evaluated by removal and degradation of Rhodamine B in water solution under ultrasonic vibration. Decrease in dye concentrations in the dye solutions were monitored in the UV-Visible Spectrophotometer to determine piezocatalytic degradation performance and absorption spectrum. The dye degradation efficiency of each polymer was determined according to the formula given in the “Experimental” section.

The characteristic peak, 554 nm, was recorded. According to the results, the comparative piezocatalytic dye degradation performance of polymer films in terms of  $\left(\frac{C}{C_0}\right)$  versus time can be seen from the Figure 3.18 below. It can be concluded from this Figure that dye degradation of homopolymer solution at 105 min was 27%, 55/45 copolymer solution dye degradation was 40%, 50/50 copolymer solution dye degradation was 47% and terpolymer solution dye degradation was 54%. The dye degradation performance of the homopolymer was found to be lower compared to the copolymer and terpolymer. The addition of the second and third monomers to the homopolymer improves the piezocatalytic dye degradation performance.

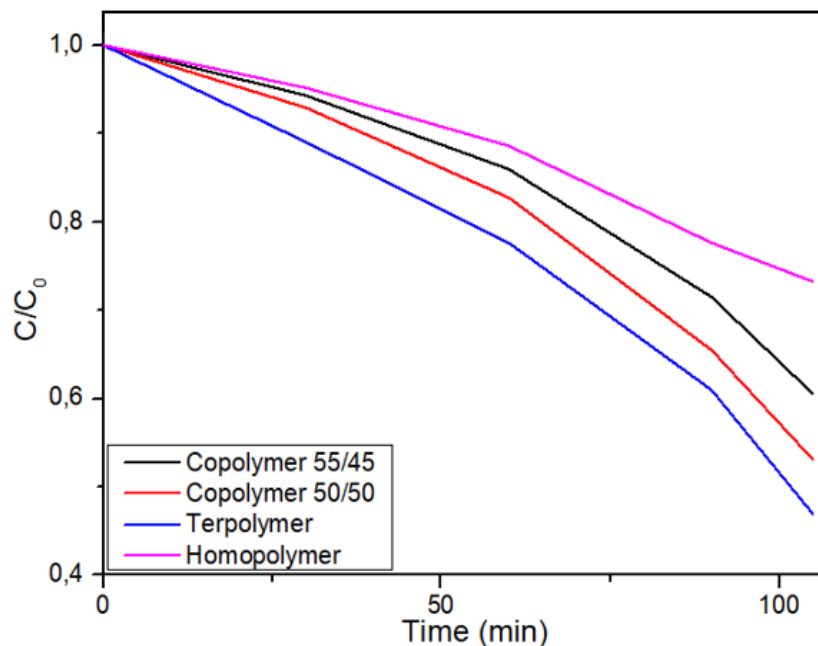


Figure 3.18. Dye degradation performance (%) of polymers.

Figure 3.19 shows that dye degradation rate and rate constants for polymers. Since it is degradation, first order reaction kinetics is observed in this situation. The rate constants and degradation rates were calculated from the equation  $\ln\left(\frac{C}{C_0}\right) = kxt$ . According to the results, terpolymer has  $0.068 \text{ min}^{-1}$  rate constants, which is the highest rate constant. Thus, terpolymer has promising performance for piezocatalytic dye degradation for water pollution.

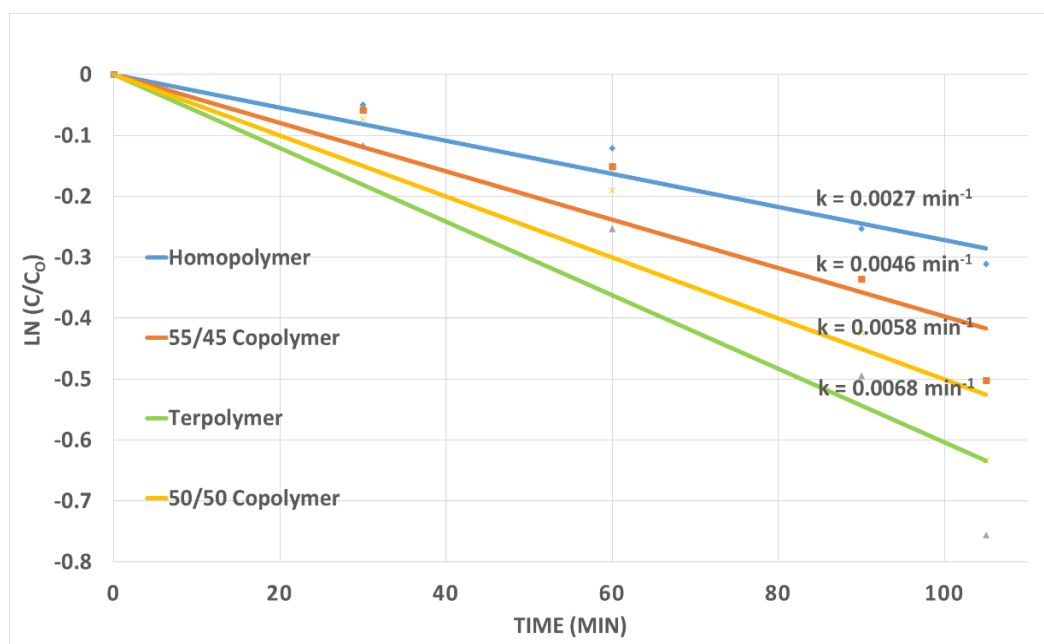


Figure 3.19. Piezocatalytic dye degradation kinetic rate and rate constants.

In addition, Figure 3.20 shows the decrease in 554 nm peak intensity at the end of 105 min of sonication treatments of each solution. Since significant dye degradation was achieved at 105 min, the experiments continued until this time. The degradation performance of the Rhodamine B dyestuff under ultrasonic vibration of the homopolymer was found to be the lowest at the end of the 105th minute. It was the terpolymer that exhibited the highest and most efficient piezocatalytic performance. It can be said that more polarization fields are created by increased piezoelectricity, and as a result, more free charge carriers ( $h^+$  and  $e^-$ ) are able to separate from one another by moving in opposing directions in response to field forces.

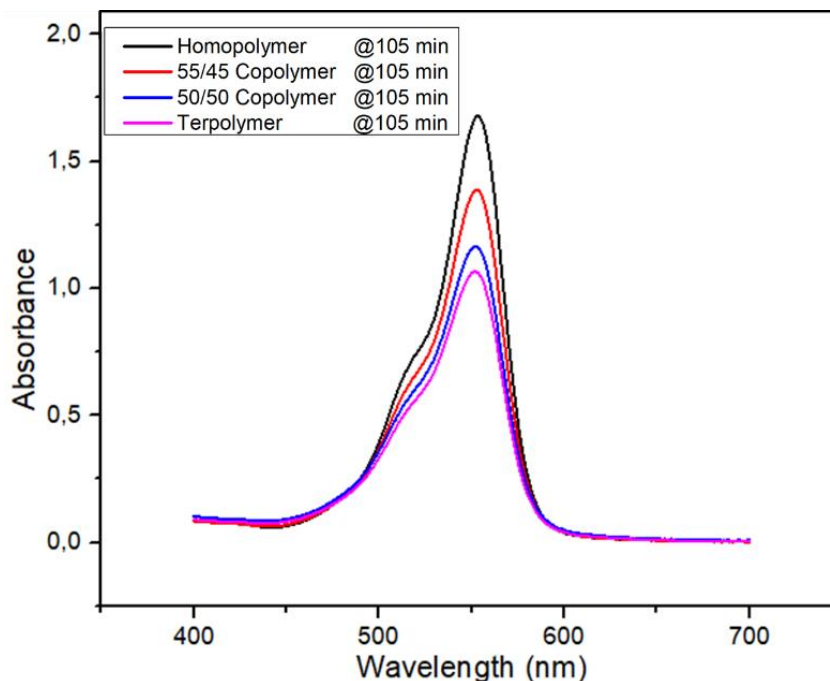


Figure 3.20. Absorbance-wavelength graphs of RhB solutions at the end of 105 min.

The spectrum curves of the dye degradation performances of each polymer solution at certain time intervals can be examined from the graphs in Figure 3.21 given below. For example, at the end of half an hour, the homopolymer has the lowest degradation performance, while the terpolymer has the highest degradation performance.

If the piezocatalytic experimental results are evaluated according to the "Energy Band Theory", since the band tilting depends on the piezopotential magnitude, it is expected that the polymer with the best piezoelectricity, namely the terpolymer, will have the best piezocatalytic performance. Because in some parts the formation of radicals is not thermodynamically favorable. This is due to the mismatch of the band level and the potential required for redox reactions. However, by tilting the band structure with strain, the necessary positions for the valence band and conduction band can be provided. According to the results, the band tilting degree of terpolymer was higher than other polymers<sup>65</sup>.

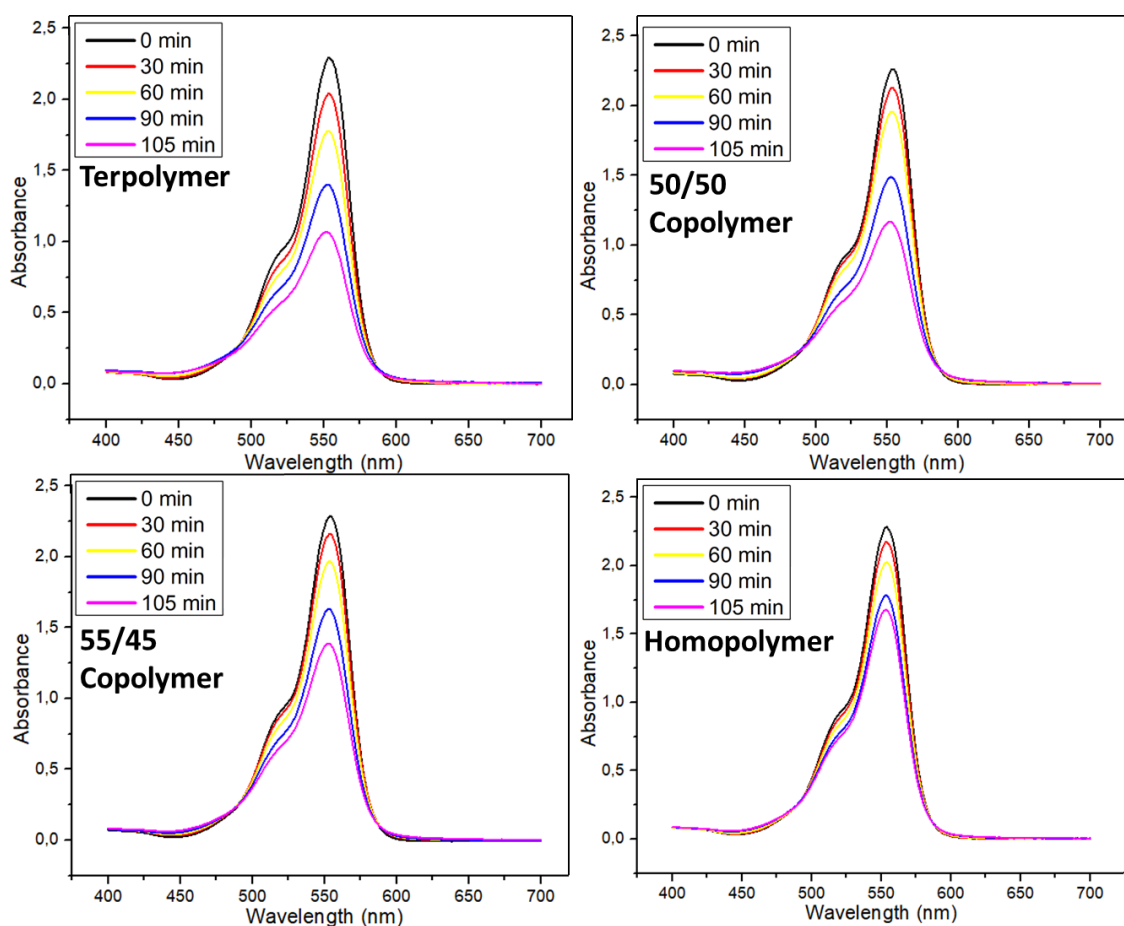


Figure 3.21. Absorbance versus wavelength graphs of RhB solutions.

According to the "Screening Charge Effect", energies of the charge carriers are directly determined by piezopotential. The piezopotential controls a piezocatalyst's ability to influence a chemical reaction. While mechanical excitation is important in energy band theory, change in polarization is important for screening charge effect. So, since change in polarization for terpolymer is higher than other polymers, it performed more efficient dye degradation<sup>65</sup>.

If this study is compared with other studies in literature, Table 3.2 can be a good summary. The PVDF in this study performed better than a bare PVDF in the literature<sup>67</sup>, while it performed worse than another study<sup>64</sup>. Although high power ultrasonic vibration was used in the study in which "Bisphenol A" was degraded<sup>67</sup>, an efficiency of 10% was observed. This may be due to the short degradation time<sup>67</sup>. In "Methylene Blue" degradation, the power is relatively lower, but the degradation time is long<sup>64</sup>. From this point of view, assuming that the parameters of our study are average, its efficiency is compatible with the literature.

Table 3.2. Piezocatalytic performance for different materials from literature.

Piezo-catalysis	Targeted effluent	Degradation time (min)	Efficiency (%)	Power and Frequency	Reference
PVDF homopolymer	Rhodamine -B	105	27	25 kHz, 200 W	This study
55/45 PVDF-TrFE	Rhodamine -B	105	40	25 kHz, 200 W	This study
50/50 PVDF-TrFE	Rhodamine -B	105	47	25 kHz, 200 W	This study
PVDF-TrFE-CTFE	Rhodamine -B	105	54	25 kHz, 200 W	This study
Bare PVDF	Methylene Blue	180	37	40 kHz, 70 W	<sup>64</sup>
5 wt. % BCZTO/PVDF	Methylene Blue	180	70	40 kHz, 70 W	<sup>64</sup>
Bare PVDF	Bisphenol A	60	10	40 kHz, 300 W	<sup>67</sup>
Poly(dimethylsiloxane) (PDMS)-BTO	Bisphenol A	60	70	40 kHz, 300 W	<sup>67</sup>
BNT nanofiber	Rhodamine -B	180	60	45 kHz, 200 W	<sup>110</sup>
BNT/PVDF	Rhodamine -B	180	80	45 kHz, 200 W	<sup>110</sup>
BiFeO <sub>3</sub> /TiO <sub>2</sub>	Methyl Violet	120	45	40 kHz, 300 W	<sup>111</sup>
ZnO	Acid orange	100	32	45 kHz, 150 W	<sup>112</sup>
ZnO/PVDF	Rhodamine -B	100	90	40 kHz, 300 W	<sup>113</sup>
BTO	4-chlorophenol	120	71	40 kHz, 80 W	<sup>114</sup>
P(VDF-TrFE)/BiFeO <sub>3</sub>	Rhodamine -B	30	92	-	<sup>115</sup>

Polymer-ceramic composites in the literature generally showed high efficiency. For example, PVDF polymer-ceramic composites with 5% wt. BCZTO doped have high piezocatalytic efficiency due to contribution of ceramic particles <sup>64</sup>. Likewise, it was observed that the BNT-doped PVDF composites <sup>110</sup> had similar performance with the BCZTO-doped. This shows that the high piezoelectric property of ceramic is an advantage for the piezocatalytic property. However, when ZnO, BNT and BTO were used alone, they did not show a higher efficiency than polymer-ceramic composites. In this

context, making a composite or copolymer/terpolymer may be more advantageous in a piezocatalytic sense.

In short, PVDF-based copolymers and terpolymers in this study also showed very good properties, although they did not have as strong piezocatalytic performance as ceramic/polymer-ceramic composites. Obtained piezocatalytic measurement results were as expected, because piezoelectric properties would be strengthened when the second and third monomers were added to PVDF, it was expected that the piezocatalytic properties would also increase. For piezocatalytic experiments, process parameters were observed to be a very sensitive variable. All parameters from the amount of ultrasonic probe tip immersion into the solution to the ambient temperature can affect the test results. For this reason, even if the same ambient conditions are tried to be provided for each polymer, experimental errors or deviations may certainly occur. In addition, other experimental parameters differ in the literature, and this might also affect the results. It was shown that frequency and power of the sonication are critical parameters that control the piezocatalytic efficiency. Moreover, sonication alone without a piezocatalyst can also be effective if the correct sonication power and frequency is used. Therefore, it might be necessary to differentiate between the effects of sonication and piezocatalyst <sup>116</sup>.

### **3.8. Discussion of Results**

According to the experimental results, due to the increase in piezoelectricity, a noticeable increase in piezocatalytic properties was observed. The 2nd and 3rd comonomer and termonomer added to the homopolymer enhance the properties of the polymers. Piezoelectric and strain properties also increased with increasing TrFE content in the copolymer. Terpolymer exhibited the highest and most efficient piezocatalytic performance. It can be said that more polarization fields mean increase in piezoelectricity, and as a result, more free charge carriers (h<sup>+</sup> and e<sup>-</sup>) are able to separate from one another by moving in opposing directions in response to polarization field.

According to the "Energy Band Theory", if the piezocatalytic experimental results are discussed, it is expected that the terpolymer with the best piezoelectricity will have the best piezocatalytic performance since the band tilting depends on the size of the piezopotential. In some cases, since radical formation is not thermodynamically favorable, the band structure can be bent with strain to provide the necessary positions

for the valence band and conduction band. According to the results obtained in this experiment, it was observed that the band bending degree of the terpolymer was higher than the other polymers.

According to the results obtained from the XRD data, the desired  $\beta$ -phase of the polymer, which is mainly responsible from the piezoelectric properties, was obtained in all polymers. According to the SEM images, it was observed that all polymers had a homogeneous thickness distribution throughout the cross section. The amount of crystallization appears to be quite sufficient for all polymers compared to the literature<sup>75</sup>. From DSC results, the addition of TrFE into PVDF affects thermal stability of the polymers. For copolymers with the composition of 55/45 and 50/50 mol%, melting temperature,  $T_m$ , increased. However, with increasing TrFE content, Curie point ( $T_C$ ) decreased for copolymers. For copolymers, with increasing TrFE content, crystallinity decreases. In addition, the estimated crystallization amounts were calculated. For copolymers, with increasing TrFE content, crystallinity decreases. It can be understood also from the sharpness of the DSC curve peaks. Broader peak was observed in terpolymers.

From the dielectric measurements, within the transition region ( $49 \text{ mol}\% \leq C_{\text{VDF}} \leq 55 \text{ mol}\%$ ) of P(VDF-TrFE), both normal-ferroelectric and relaxor characteristics were observed<sup>38</sup>. As the VDF content increases, the dielectric constant decreases after a point. Terpolymer showed relaxor properties as expected. According to the hysteresis loops of polymers, increasing the composition of TrFE caused the increase in polarization because bulky TrFE group provides the larger interchain distance in copolymer and dipole moments can easily rotate in copolymers. As a result of the strain measurements, all of the polymers had inverse butterfly shapes. Homopolymer has the lowest strain while copolymers and terpolymer have higher strain values. The addition of TrFE and CTFE monomers enhanced the strain.

To sum up, as intended, efficient piezoelectric and piezocatalytic properties were observed. With these advanced properties, removal of impurities and dyestuffs in water were achieved by adding the 2nd and 3rd monomers to the homopolymer as desired. In general, as expected it was observed that piezocatalytic property would increase with increasing piezoelectric property.

## CHAPTER 4

### CONCLUSION

In this thesis study, piezocatalytic and piezoelectric properties of P(VDF) based homopolymer, copolymer and terpolymers were investigated. P(VDF) homopolymer films, P(VDF-TrFE) copolymers (55/45 and 50/50 mol%) films, and P(VDF-TrFE-CTFE) terpolymer films with 62/31/7 mol% were synthesized. It was intended to observe the change in piezoelectric and piezocatalytic properties and dye degradation efficiency with the addition of comonomer and termonomer and compare them.

According to the results obtained from the XRD data, the desired  $\beta$ -phase of the polymer, which is mainly responsible from the piezoelectric properties, was obtained in all polymers. Annealing temperatures for copolymers were selected according to the condition in which the XRD peak of the  $\beta$ -phase was most visible and of high intensity was the most suitable condition which was determined as 140 °C.

From the DSC graphs, the estimated crystallization amounts were calculated using enthalpy values of the fully crystallized polymer and enthalpy of the melting peak. For copolymers, with increasing TrFE content, crystallinity decreases. It can be understood also from the sharpness of the DSC curve peaks. Broader peak was observed in terpolymers, this confirms estimated crystallization amount of terpolymer which is approximately 10%.

It was observed that the 2nd and 3rd monomer added to the homopolymer enhanced the properties of the polymers, as expected. Piezoelectric properties and strain characteristics improved with the addition of TrFE to the copolymer. According to the hysteresis loops of polymers, increasing the composition of TrFE caused the increase in polarization because bulky TrFE group. Maximum polarization of terpolymer was observed as 11  $\mu\text{C}/\text{cm}^2$ . Due to the increase in piezoelectricity, a remarkable increase in piezocatalytic properties was observed. Terpolymer had the most efficient piezocatalytic performance with the efficiency of 54%. P(VDF) homopolymer was reached 27% dye degradation efficiency. For copolymers with mol% 55/45 and 50/50, dye degradation efficiencies were 40% and 47%, respectively.

In addition, both normal-ferroelectric and relaxor characteristics were observed from the dielectric measurements, within the transition region ( $49 \text{ mol}\% \leq C_{\text{VDF}} \leq 55 \text{ mol}\%$ ) of P(VDF-TrFE). Terpolymer showed relaxor properties as expected. As a result of the strain measurements, all the polymers had inverse butterfly shapes. Homopolymer has the lowest strain while copolymers and terpolymer have higher strain values. The addition of TrFE and CTFE monomers enhanced the strain.

## REFERENCES

1. R. K. Pandey. *Fundamentals of Electroceramics: Materials, Devices, and Applications* - R. K. Pandey - Google Kitaplar; 2019.
2. Cross, L. E. Relaxor Ferroelectrics. *Springer Series in Materials Science* 2008, *114*, 131–155. [https://doi.org/10.1007/978-3-540-68683-5\\_5/COVER](https://doi.org/10.1007/978-3-540-68683-5_5/COVER).
3. Khanbareh Hamideh. Expanding the Functionality of Piezo-Particulate Composites, Delft University of Technology, 2016.
4. Damjanovic, D. Ferroelectric, Dielectric and Piezoelectric Properties of Ferroelectric Thin Films and Ceramics. *Rep. Prog. Phys* 1998, *61*, 1267–1324.
5. Kamel, T. M. Poling and Switching of PZT Ceramics : Field and Grain Size Effects, Eindhoven University of Technology, 2007.
6. Ohsato, H. Origin of Piezoelectricity on Langasite. 2012, 15–40.
7. Li, J.-Feng. *Lead-Free Piezoelectric Materials*; Wiley-VCH, 2021.
8. Jiang, H.; Yang, J.; Xu, F.; Wang, Q.; Liu, W.; Chen, Q.; Wang, C.; Zhang, X.; Zhu, G. VDF-Content-Guided Selection of Piezoelectric P(VDF-TrFE) Films in Sensing and Energy Harvesting Applications. *Energy Convers Manag* 2020, *211*. <https://doi.org/10.1016/j.enconman.2020.112771>.
9. Mishra, S.; Unnikrishnan, L.; Kumar Nayak, S.; Mohanty Mishra, S. S.; Unnikrishnan, L.; Nayak, S. K.; Mohanty, S. Advances in Piezoelectric Polymer Composites for Energy Harvesting Applications: A Systematic Review . *Macromol Mater Eng* 2019, *304* (1). <https://doi.org/10.1002/mame.201800463>.
10. Kwon, D. S.; Ko, H. J.; Kim, M. O.; Oh, Y.; Sim, J.; Lee, K.; Cho, K. H.; Kim, J. Piezoelectric Energy Harvester Converting Strain Energy into Kinetic Energy for Extremely Low Frequency Operation. *Appl Phys Lett* 2014, *104* (11). <https://doi.org/10.1063/1.4869130>.

11. Usher, T. D.; Cousins, K. R.; Zhang, R.; Ducharme, S. The Promise of Piezoelectric Polymers Introduction and Theory. *Polym Int* 2018, 7 (67), 790–798. <https://doi.org/10.1002/pi.5584>.
12. Kim, H.; Kim, J. A Review of Piezoelectric Energy Harvesting Based on Vibration. *International journal of precision engineering and manufacturing* 2011, 6 (12), 1129–1141.
13. Caliò, R.; Rongala, U. B.; Camboni, D.; Milazzo, M.; Stefanini, C.; de Petris, G.; Oddo, C. M. Piezoelectric Energy Harvesting Solutions. *Sensors* 2014, 14 (3), 4755–4790. <https://doi.org/10.3390/S140304755>.
14. Vijaya, M. S. *Piezoelectric Materials and Devices: Applications in Engineering and Medical Sciences*; 2013.
15. Santhya, M.; Kulkarni, S. M.; Rao, M.; Mohith, S.; Upadhya, A. R.; Navin, K. P. Recent Trends in Piezoelectric Actuators for Precision Motion and Their Applications: A Review. *Smart Mater Struct* 2020, 1 (30). <https://doi.org/10.1088/1361-665X/abc6b9>.
16. Smith, M.; Kar-Narayan, S. Piezoelectric Polymers: Theory, Challenges and Opportunities. *International Materials Reviews* 2022, 67 (1), 65–88. <https://doi.org/10.1080/09506608.2021.1915935>.
17. Furukawa, T.; Date, M.; Fukada, E. Hysteresis Phenomena in Polyvinylidene Fluoride under High Electric Field. *J Appl Phys* 1980, 51 (2), 1141. <https://doi.org/10.1063/1.327723>.
18. Wu, T.; Jin, H.; Dong, S.; Xuan, W.; Xu, H.; Lu, L.; Fang, Z.; Huang, S.; Tao, X.; Shi, L.; Liu, S.; Luo, J. A Flexible Film Bulk Acoustic Resonator Based on  $\beta$ -Phase Polyvinylidene Fluoride Polymer. *Sensors* 2020, 20 (5), 1346. <https://doi.org/10.3390/S20051346>.
19. Xia, W.; Zhang, Z. PVDF-Based Dielectric Polymers and Their Applications in Electronic Materials. *Iet Nanodielectrics* 2018, 1 (1), 17–31. <https://doi.org/10.1049/iet-nde.2018.0001>.

20. Persano, L.; Catellani, A.; Dagdeviren, C.; Ma, Y.; Guo, X.; Huang, Y.; Calzolari, A.; Pisignano, D. Shear Piezoelectricity in Poly(Vinylidene fluoride-Co-Trifluoroethylene): Full Piezotensor Coefficients by Molecular Modeling, Biaxial Transverse Response, and Use in Suspended Energy-Harvesting Nanostructures. *2016*, *28* (35), 7633–7639. <https://doi.org/10.1002/adma.201506381>.
21. Bystrov, V. S.; Paramonova, E. V.; Bdikin, I. K.; Bystrova, A. V.; Pullar, R. C.; Kholkin, A. L. Molecular Modeling of the Piezoelectric Effect in the Ferroelectric Polymer Poly(Vinylidene Fluoride) (PVDF). *J Mol Model* 2013, *19*, 3591–3602. <https://doi.org/10.1007/s00894-013-1891-z>.
22. Broadhurst, M. G.; Davis, G. T. Physical Basis for Piezoelectricity in PVDF. *Ferroelectrics* 1984, *60* (1), 3–13. <https://doi.org/10.1080/00150198408017504>.
23. Broadhurst, M. G.; Davis, G. T.; McKinney, J. E.; & Collins, R. E. Piezoelectricity and Pyroelectricity in Polyvinylidene Fluoride - A Model. *J Appl Phys* 1978, *49* (10), 4992–4997.
24. Ilias Katsouras, B.; Asadi, K.; Li, M.; van Driel, T. B.; Kjaer, K. S.; Zhao, D.; Lenz, T.; Gu, Y.; Blom, P. W.; Damjanovic, D.; Nielsen, M. M.; de Leeuw, D. M. *The Negative Piezoelectric Effect of the Ferroelectric Polymer Poly(Vinylidene-Fluoride)*.
25. Furukawa, T.; Date, M.; Fukada, E.; Tajitsu, Y. Ferroelectric Behavior in the Copolymer of Vinylidene fluoride and Trifluoroethylene. *Jpn J Appl Phys* 1980.
26. Yagi, T.; Tatemoto, M.; Sako, J.-I. Transition Behavior and Dielectric Properties in Trifluoroethylene and Vinylidene Fluoride Copolymers. *Polym J* 1980, *12* (4), 209–223.
27. Lheritier, P.; Noel, S.; Vaxelaire, N.; Domingues Dos Santos, F.; Defay, E. Actuation Efficiency of Polyvinylidene Fluoride-Based Co- and Ter-Polymers. *Polymer (Guildf)* 2018, *156*, 270–275. <https://doi.org/10.1016/j.polymer.2018.10.003>.
28. Sun, Q.; Xia, W.; Liu, Y.; Ren, P.; Tian, X.; Hu, T. The Dependence of Acoustic Emission Performance on the Crystal Structures, Dielectric, Ferroelectric, and

- Piezoelectric Properties of the P(VDF-TrFE) Sensors. *IEEE Trans Ultrason Ferroelectr Freq Control* 2020, 67 (5), 975–983. <https://doi.org/10.1109/TUFFC.2019.2959353>.
29. Wang, S.; Li, Q. Design, Synthesis and Processing of PVDF-Based Dielectric Polymers. *IET Nanodielectrics*. Institution of Engineering and Technology 2018, pp 80–91. <https://doi.org/10.1049/iet-nde.2018.0003>.
  30. Liu Yang; Chen Xin; Han Zhubing; Zhou Huamin; Wang Qing. Defects in Poly(Vinylidene Fluoride)-Based Ferroelectric Polymers from a Molecular Perspective. *Applied Physics Review* 2022, 9 (3).
  31. Bauer, F. Review on the Properties of the Ferrorelaxor Polymers and Some New Recent Developments. *Applied Physics A: Materials Science and Processing*. June 2012, pp 567–573. <https://doi.org/10.1007/s00339-012-6831-8>.
  32. Ou-Yang, W., Weis, M., Chen, X., Manaka, T., & Iwamoto, M. (2009). Study of phase transition of two-dimensional ferroelectric copolymer P (VDF-TrFE) Langmuir monolayer by Maxwell displacement current and Brewster angle microscopy. *The Journal of Chemical Physics*, 131(10).
  33. Zhang, Q. M.; Bhart Vivek. Giant Electrostriction and Relaxor Ferroelectric in Electron-Irradiated Poly(Vinylidene-Trifluoroethylene) Copolymer. *Science (1979)* 1998, 280.
  34. Cheng, Z.; Li, H.; Xia, F.; Huang, C.; Kavarnos, G. J. Electromechanical Properties and Molecular Conformation in P (VDF-TrFE)-Based Terpolymer. . *In Smart Structures and Materials 2002: Electroactive Polymer Actuators and Devices (EAPAD) 2002*, 167–175.
  35. Yang, L.; Li, X.; Allahyarov, E.; Taylor, P. L.; Zhang, Q. M.; Zhu, L. Novel Polymer Ferroelectric Behavior via Crystal Isomorphism and the Nanoconfinement Effect. *Polymer*. Elsevier Ltd March 22, 2013, pp 1709–1728. <https://doi.org/10.1016/j.polymer.2013.01.035>.

36. Tiwari, V.; Srivastava, G. Effect of Thermal Processing Conditions on the Structure and Dielectric Properties of PVDF Films. *Journal of Polymer Research* 2014, 21 (11). <https://doi.org/10.1007/s10965-014-0587-0>.
37. Gomes, J.; Nunes, J. S.; Sencadas, V.; Lanceros-Mendez, S. Influence of the  $\beta$ -Phase Content and Degree of Crystallinity on the Piezo-and Ferroelectric Properties of Poly(Vinylidene Fluoride). *Smart Mater Struct* 2010, 19 (6). <https://doi.org/10.1088/0964-1726/19/6/065010>.
38. Liu, Y.; Aziguli, H.; Zhang Bing; Xu Wenhan; Lu Wenchang. Ferroelectric Polymers Exhibiting Behaviour Reminiscent of a Morphotropic Phase Boundary. *Nature* 2018, No. 562, 96–100.
39. Prateek; Thakur, V. K.; Gupta, R. K. Recent Progress on Ferroelectric Polymer-Based Nanocomposites for High Energy Density Capacitors: Synthesis, Dielectric Properties, and Future Aspects. *Chemical Reviews*. American Chemical Society April 27, 2016, pp 4260–4317. <https://doi.org/10.1021/acs.chemrev.5b00495>.
40. Qing, L. *Development of Electrostrictive P(VDF-TrFE-CTFE) Terpolymer for Inkjet Printed Electromechanical Devices*. <http://theses.insa-lyon.fr/publication/2016LYSEI126/these.pdf>.
41. Lu, S.; Zhang, X.; Xue, Y. Application of Calcium Peroxide in Water and Soil Treatment: A Review. *Journal of Hazardous Materials*. Elsevier B.V. 2017, pp 163–177. <https://doi.org/10.1016/j.jhazmat.2017.04.064>.
42. Shah Maulin; Banerjee Aditi. *Combined Application of Physico-Chemical & Microbiological Processes for Industrial Effluent Treatment Plant*; Springer Singapore, 2020. <https://doi.org/10.1007/978-981-15-0497-6>.
43. Saigl, Z. M. Various Adsorbents for Removal of Rhodamine b Dye: A Review. *Indonesian Journal of Chemistry*. Gadjah Mada University 2021, pp 1039–1056. <https://doi.org/10.22146/ijc.62863>.
44. Warang, T.; Patel, N.; Fernandes, R.; Bazzanella, N.; Miotello, A. Co<sub>3</sub>O<sub>4</sub> Nanoparticles Assembled Coatings Synthesized by Different Techniques for

- Photo-Degradation of Methylene Blue Dye. *Appl Catal B* 2013, 132–133, 204–211. <https://doi.org/10.1016/j.apcatb.2012.11.040>.
45. Duarte, F.; Maldonado-Hódar, F. J.; Madeira, L. M. New Insight about Orange II Elimination by Characterization of Spent Activated Carbon/Fe Fenton-like Catalysts. *Appl Catal B* 2013, 129, 264–272. <https://doi.org/10.1016/j.apcatb.2012.09.037>.
46. N. Amenaghawon, A.; A. Asegame, P.; O. Obahiagbon, K. Potential Application of Urea and NPK 15:15:15 Fertilizers as Biostimulants in the Bioremediation of Domestic Wastewater. *American Journal of Environmental Protection* 2013, 1 (4), 91–95. <https://doi.org/10.12691/env-1-4-3>.
47. Chen, Y. P.; Wu, C.; Ma, W. X.; Li, Y.; Chen, Y. Research Progress of Sewage Treatment Technology. In *Advanced Materials Research*; 2013; Vol. 726–731, pp 2576–2579. <https://doi.org/10.4028/www.scientific.net/AMR.726-731.2576>.
48. Mushtaq, F.; Chen, X.; Hoop, M.; Torlakcik, H.; Pellicer, E.; Sort, J.; Gattinoni, C.; Nelson, B. J.; Pané, S. Piezoelectrically Enhanced Photocatalysis with BiFeO<sub>3</sub> Nanostructures for Efficient Water Remediation. *iScience* 2018, 4, 236–246. <https://doi.org/10.1016/j.isci.2018.06.003>.
49. Qu, Y.; Duan, X. Progress, Challenge and Perspective of Heterogeneous Photocatalysts. *Chem Soc Rev* 2013, 42 (7), 2568–2580. <https://doi.org/10.1039/c2cs35355e>.
50. Tu, S.; Huang, H.; Zhang, T.; Zhang, Y. Controllable Synthesis of Multi-Responsive Ferroelectric Layered Perovskite-like Bi<sub>4</sub>Ti<sub>3</sub>O<sub>12</sub>: Photocatalysis and Piezoelectric-Catalysis and Mechanism Insight. *Appl Catal B* 2017, 219, 550–562. <https://doi.org/10.1016/j.apcatb.2017.08.001>.
51. Lin, J. H.; Tsao, Y. H.; Wu, M. H.; Chou, T. M.; Lin, Z. H.; Wu, J. M. Single- and Few-Layers MoS<sub>2</sub> Nanocomposite as Piezo-Catalyst in Dark and Self-Powered Active Sensor. *Nano Energy* 2017, 31, 575–581. <https://doi.org/10.1016/j.nanoen.2016.12.013>.

52. Dutta, D. P.; Singh, A.; Tyagi, A. K. Ag Doped and Ag Dispersed Nano ZnTiO<sub>3</sub>: Improved Photocatalytic Organic Pollutant Degradation under Solar Irradiation and Antibacterial Activity. *J Environ Chem Eng* 2014, 2 (4), 2177–2187. <https://doi.org/10.1016/j.jece.2014.09.015>.
53. Lan, S.; Feng, J.; Xiong, Y.; Tian, S.; Liu, S.; Kong, L. *Performance and Mechanism of Piezo-Catalytic Degradation of 4-Chlorophenol: Finding of Effective Piezo-Dechlorination Performance and Mechanism of Piezo-Catalytic Degradation of 4-Chlorophenol: Finding of Effective Piezo-Dechlorination 2*; 2017. <http://pubs.acs.org>.
54. Xu, X.; Jia, Y.; Xiao, L.; Wu, Z. Strong Vibration-Catalysis of ZnO Nanorods for Dye Wastewater Decolorization via Piezo-Electro-Chemical Coupling. *Chemosphere* 2018, 193, 1143–1148. <https://doi.org/10.1016/j.chemosphere.2017.11.116>.
55. Feng, Y.; Ling, L.; Wang, Y.; Xu, Z.; Cao, F.; Li, H.; Bian, Z. Engineering Spherical Lead Zirconate Titanate to Explore the Essence of Piezo-Catalysis. *Nano Energy* 2017, 40, 481–486. <https://doi.org/10.1016/j.nanoen.2017.08.058>.
56. Liu, X.; Wang, T.; Li, G.; Liu, G.; Qiu, J.; Guo, Z.; Hao, H.; Dong, J.; Liu, H.; Xing, J. Cooperation or Competition between Piezocatalysis and Photocatalysis of Bi<sub>4</sub>Ti<sub>3</sub>O<sub>12</sub> Nanoflakes. *J Alloys Compd* 2023, 936. <https://doi.org/10.1016/j.jallcom.2022.168367>.
57. Ikeda, S.; Takata, T.; Kondo, T.; Hitoki, G.; Hara, M.; Kondo, J. N.; Domen, K.; Hosono, H.; Kawazoe, H.; Tanaka, A. Mechano-Catalytic Overall Water Splitting. *Chemical Communications* 1998, No. 20, 2185–2186. <https://doi.org/10.1039/a804549f>.
58. Vedadi, M. H.; Haas, S. Mechano-Chemical Pathways to H<sub>2</sub>O and CO<sub>2</sub> Splitting. *Appl Phys Lett* 2011, 99 (15). <https://doi.org/10.1063/1.3650695>.
59. Mushtaq, F.; Chen, X.; Hoop, M.; Torlakcik, H.; Pellicer, E.; Sort, J.; Gattinoni, C.; Nelson, B. J.; Pané, S. Piezoelectrically Enhanced Photocatalysis with BiFeO<sub>3</sub>

- Nanostructures for Efficient Water Remediation. *iScience* 2018, 4, 236–246. <https://doi.org/10.1016/j.isci.2018.06.003>.
60. Wu, J.; Qin, N.; Bao, D. Effective Enhancement of Piezocatalytic Activity of BaTiO<sub>3</sub> Nanowires under Ultrasonic Vibration. *Nano Energy* 2018, 45, 44–51. <https://doi.org/10.1016/j.nanoen.2017.12.034>.
61. Singh, G.; Sharma, M.; Vaish, R. Exploring the Piezocatalytic Dye Degradation Capability of Lithium Niobate. *Advanced Powder Technology* 2020, 31 (4), 1771–1775. <https://doi.org/10.1016/j.appt.2020.01.031>.
62. Singh, G.; Sharma, M.; Vaish, R. Flexible Ag@LiNbO<sub>3</sub>/PVDF Composite Film for Piezocatalytic Dye/Pharmaceutical Degradation and Bacterial Disinfection. *ACS Appl Mater Interfaces* 2021, 13 (19), 22914–22925. <https://doi.org/10.1021/acsami.1c01314>.
63. Mondal, D.; Roy, S.; Bardhan, S.; Roy, J.; Kanungo, I.; Basu, R.; Das, S. Recent Advances in Piezocatalytic Polymer Nanocomposites for Wastewater Remediation. *Dalton Transactions* 2022, 51 (2), 451–462. <https://doi.org/10.1039/d1dt02653d>.
64. Sharma, M.; Singh, G.; Vaish, R. Piezocatalysis in Ferroelectric Ba<sub>0.85</sub>Ca<sub>0.15</sub>Zr<sub>0.1</sub>Ti<sub>0.9</sub>O<sub>3</sub>/Polyvinylidene Difluoride (PVDF) Composite Film. *J Appl Phys* 2021, 130 (8). <https://doi.org/10.1063/5.0060106>.
65. Wang, K.; Han, C.; Li, J.; Qiu, J.; Sunarso, J.; Liu, S. The Mechanism of Piezocatalysis: Energy Band Theory or Screening Charge Effect? *Angewandte Chemie - International Edition*. John Wiley and Sons Inc February 1, 2022. <https://doi.org/10.1002/anie.202110429>.
66. Wu, J.; Xu, Q.; Lin, E.; Yuan, B.; Qin, N.; Thatikonda, S. K.; Bao, D. Insights into the Role of Ferroelectric Polarization in Piezocatalysis of Nanocrystalline BaTiO<sub>3</sub>. *ACS Appl Mater Interfaces* 2018, 10 (21), 17842–17849. <https://doi.org/10.1021/acsami.8b01991>.
67. Wan, L.; Tian, W.; Li, N.; Chen, D.; Xu, Q.; Li, H.; He, J.; Lu, J. Hydrophilic Porous PVDF Membrane Embedded with BaTiO<sub>3</sub> Featuring Controlled Oxygen

- Vacancies for Piezocatalytic Water Cleaning. *Nano Energy* 2022, 94. <https://doi.org/10.1016/j.nanoen.2022.106930>.
68. Wu, J.; Xu, Q.; Lin, E.; Yuan, B.; Qin, N.; Thatikonda, S. K.; Bao, D. Insights into the Role of Ferroelectric Polarization in Piezocatalysis of Nanocrystalline BaTiO<sub>3</sub>. *ACS Appl Mater Interfaces* 2018, 10 (21), 17842–17849. <https://doi.org/10.1021/acsami.8b01991>.
69. LCR Meter Guide. *E-Journal Menara Perkebunan* 2014, 82 (1).
70. Jiang, Z. Y.; Zheng, X. C.; Zheng, G. P. The Enhanced Electrocaloric Effect in P(VDF-TrFE) Copolymer with Barium Strontium Titanate Nano-Fillers Synthesized via an Effective Hydrothermal Method. [www.rsc.org/advances](http://www.rsc.org/advances).
71. Li, H.; Tan, K.; Hao, Z.; He, G. Preparation and Crystallization Behavior of Poly(Vinylidene Fluoride-Ter-Chlorotrifluoroethylene- Ter-Trifluoroethylene). *J Appl Polym Sci* 2011, 122 (5), 3007–3015. <https://doi.org/10.1002/app.34114>.
72. Tajitsu, Y.; Chiba, A.; Bair, H. E. Ferroelectric Phase Transition in a Copolymer of Vinylidene Fluoride and Trifluoroethylene. *Ferroelectrics* 1981, 32 (1), 61–67. <https://doi.org/10.1080/00150198108238674>.
73. Martins, P.; Lopes, A. C.; Lanceros-Mendez, S. Electroactive Phases of Poly(Vinylidene Fluoride): Determination, Processing and Applications. *Progress in Polymer Science*. Elsevier Ltd 2014, pp 683–706. <https://doi.org/10.1016/j.progpolymsci.2013.07.006>.
74. Benz, M.; Euler, W. B.; Gregory, O. J. The Role of Solution Phase Water on the Deposition of Thin Films of Poly(Vinylidene Fluoride). *Macromolecules* 2002, 35 (7), 2682–2688. <https://doi.org/10.1021/ma011744f>.
75. Li, Y.; Feng, W.; Meng, L.; Tse, K. M.; Li, Z.; Huang, L.; Su, Z.; Guo, S. Investigation on In-Situ Sprayed, Annealed and Corona Poled PVDF-TrFE Coatings for Guided Wave-Based Structural Health Monitoring: From Crystallization to Piezoelectricity. *Mater Des* 2021, 199. <https://doi.org/10.1016/j.matdes.2020.109415>.

76. Fung, Y. K.; Yang, D. K.; Ying, S.; Chien, L. C.; Zumer, S.; Doane, J. W. Polymer Networks Formed in Liquid Crystals. *Liq Cryst* 1995, 19 (6), 797–801. <https://doi.org/10.1080/02678299508031102>.
77. Qian, J.; Jiang, J.; Shen, Y. Enhanced Electrocaloric Strength in P(VDF-TrFE-CFE) by Decreasing the Crystalline Size. *Journal of Materiomics* 2019, 5 (3), 357–362. <https://doi.org/10.1016/j.jmat.2019.04.001>.
78. Genchi, G. G.; Ceseracciu, L.; Marino, A.; Labardi, M.; Marras, S.; Pignatelli, F.; Bruschini, L.; Mattoli, V.; Ciofani, G. P(VDF-TrFE)/BaTiO<sub>3</sub> Nanoparticle Composite Films Mediate Piezoelectric Stimulation and Promote Differentiation of SH-SY5Y Neuroblastoma Cells. *Adv Healthc Mater* 2016, 5 (14), 1808–1820. <https://doi.org/10.1002/adhm.201600245>.
79. Pipertzis, A.; Asadi, K.; Floudas, G. P(VDF-TrFE) Copolymer Dynamics as a Function of Temperature and Pressure in the Vicinity of the Curie Transition. *Macromolecules* 2022, 55 (7), 2746–2757. <https://doi.org/10.1021/acs.macromol.2c00280>.
80. Ullah, S.; Wang, H.; Liu, B.; Cheng, J.; Shan, G.; Zheng, G. P. The Effects of Additions of Two-Dimensional Graphitic-C<sub>3</sub>N<sub>4</sub> on the Negative Electro-Caloric Effects in P(VDF-TrFE) Copolymers. *RSC Adv* 2019, 9 (28), 15917–15925. <https://doi.org/10.1039/c9ra02428j>.
81. Michot, T.; Nishimoto, A.; Watanabe, M. *Electrochemical Properties of Polymer Gel Electrolytes Based on Poly(Vinylidene Fluoride) Copolymer and Homopolymer*; 2000; Vol. 45. [www.elsevier.nl/locate/electacta](http://www.elsevier.nl/locate/electacta).
82. Low, Y. K. A.; Tan, L. Y.; Tan, L. P.; Boey, F. Y. C.; Ng, K. W. Increasing Solvent Polarity and Addition of Salts Promote  $\beta$ -Phase Poly(Vinylidene Fluoride) Formation. *J Appl Polym Sci* 2013, 128 (5), 2902–2910. <https://doi.org/10.1002/app.38451>.
83. Ma, W.; Zhang, J.; Chen, S.; Wang, X. Crystalline Phase Formation of Poly(Vinylidene Fluoride) from Tetrahydrofuran/N,N-Dimethylformamide Mixed

- Solutions. *Journal of Macromolecular Science, Part B: Physics* 2008, 47 (3), 434–449. <https://doi.org/10.1080/00222340801954811>.
84. Pedroli, F.; Marrani, A.; Le, M. Q.; Froidefond, C.; Cottinet, P. J.; Capsal, J. F. Processing Optimization: A Way to Improve the Ionic Conductivity and Dielectric Loss of Electroactive Polymers. *J Polym Sci B Polym Phys* 2018, 56 (16), 1164–1173. <https://doi.org/10.1002/polb.24636>.
85. Sigamani, N. *Effect Of Processing Conditions on the Microstructure and Electromechanical Response of PvdF Trfe Ctfe Terpolymers*, 2014-7696. <https://www.researchgate.net/publication/265846807>.
86. Cho, Y.; Ahn, D.; Park, J. B.; Pak, S.; Lee, S.; Jun, B. O.; Hong, J.; Lee, S. Y.; Jang, J. E.; Hong, J.; Morris, S. M.; Sohn, J. I.; Cha, S. N.; Kim, J. M. Enhanced Ferroelectric Property of P(VDF-TrFE-CTFE) Film Using Room-Temperature Crystallization for High-Performance Ferroelectric Device Applications. *Adv Electron Mater* 2016, 2 (10). <https://doi.org/10.1002/aelm.201600225>.
87. Deng, S.; Yuan, J.; Lin, Y.; Yu, X.; Ma, D.; Huang, Y.; Ji, R.; Zhang, G.; Yang, N. *Electric-Field-Induced Modulation of Thermal Conductivity in Poly(Vinylidene Fluoride)*.
88. Ren, X.; Meng, N.; Yan, H.; Bilotti, E.; Reece, M. J. Remarkably Enhanced Polarizability and Breakdown Strength in PVDF-Based Interactive Polymer Blends for Advanced Energy Storage Applications. *Polymer (Guildf)* 2019, 168, 246–254. <https://doi.org/10.1016/j.polymer.2019.02.054>.
89. Jain, A.; Kumar, S.; Mahapatra, D. R.; Rathod, V. T. Development of P (VDF-TrFE) Films and Its Quasi-Static and Dynamic Strain Response. *Int J Eng Res Technol* 2013, 2, 2598–2605.
90. Meng, N.; Zhu, X.; Mao, R.; Reece, M. J.; Bilotti, E. Nanoscale Interfacial Electroactivity in PVDF/PVDF-TrFE Blended Films with Enhanced Dielectric and Ferroelectric Properties. *J Mater Chem C Mater* 2017, 5 (13), 3296–3305. <https://doi.org/10.1039/c7tc00162b>.

91. Roggero, A.; Dantras, E.; Lacabanne, C. Poling Influence on the Mechanical Properties and Molecular Mobility of Highly Piezoelectric P(VDF-TrFE) Copolymer. *J Polym Sci B Polym Phys* 2017, 55 (18). <https://doi.org/10.1002/polb.24396i>.
92. Teyssède, G.; Lacabanne, C. Study of the Thermal and Dielectric Behavior of P(VDF-TrFE) Copolymers in Relation with Their Electroactive Properties. *Ferroelectrics* 1995, 171 (1), 125–144. <https://doi.org/10.1080/00150199508018427>.
93. Tencé-Girault, S.; Lebreton, S.; Bunau, O.; Dang, P.; Bargain, F. Simultaneous SAXS-WAXS Experiments on Semi-Crystalline Polymers: Example of PA11 and Its Brill Transition. *Crystals (Basel)* 2019, 9 (5). <https://doi.org/10.3390/cryst9050271>.
94. Schick, C. Differential Scanning Calorimetry (DSC) of Semicrystalline Polymers. *Analytical and Bioanalytical Chemistry*. November 2009, pp 1589–1611. <https://doi.org/10.1007/s00216-009-3169-y>.
95. Venkatesan, T. R.; Wübbenhorst, M.; Gerhard, R. Structure-Property Relationships in Three-Phase Relaxor-Ferroelectric Terpolymers. *Ferroelectrics* 2021, 586 (1), 60–81. <https://doi.org/10.1080/00150193.2021.2014260>.
96. Liu, Q.; Yin, X.; Richard, C.; Capsal, J. F. Influence of the Crystallization on the Molecular Mobility and Ionic DC Conductivity Behaviors of Relaxor Ferroelectric P(VDF-TrFE-CTFE) Terpolymers. *J Polym Sci B Polym Phys* 2016, 54 (16), 1645–1657. <https://doi.org/10.1002/polb.24068>.
97. Liu, Q.; Richard, C.; Capsal, J. F. Control of Crystal Morphology and Its Effect on Electromechanical Performances of Electrostrictive P(VDF-TrFE-CTFE) Terpolymer. *Eur Polym J* 2017, 91, 46–60. <https://doi.org/10.1016/j.eurpolymj.2017.03.046>.
98. Kalel, S.; Wang, W. C. Optical Properties of PVDF-TrFE and PVDF-TrFE-CTFE Films in Terahertz Band. *Mater Res Express* 2023, 10 (4). <https://doi.org/10.1088/2053-1591/acca69>.

99. Bargain, F.; Thuau, D.; Hadziioannou, G.; Domingues dos Santos, F.; Tencé-Girault, S.; Domingues Dos Santos, F. Phase Diagram of Poly(VDF-Ter-TrFE-Ter-CTFE) Copolymers: Relationship between Crystalline Structure and Material Properties. *Polymer (Guildf)* 2020, 123203. <https://doi.org/10.1016/j.polymer.2020.123203>.
100. PolyK Technologies, U. *P(VDF-TrFE-CTFE) Terpolymer Film*. <https://piezopvdf.com/CTFE07-terpolymer-film/>.
101. Xu, H.; Cheng, Z. Y.; Olson, D.; Mai, T.; Zhang, Q. M.; Kavarnos, G. Ferroelectric and Electromechanical Properties of Poly(Vinylidene-Fluoride-Trifluoroethylene-Chlorotrifluoroethylene) Terpolymer. *Appl Phys Lett* 2001, 78 (16), 2360–2362. <https://doi.org/10.1063/1.1358847>.
102. Bae, I.; Park, Y. J.; Park, C.; Kim, R. H. *Epitaxially Grown Field-Activated Electroactive Polymers for High Performance Organic Electronics*; 2013; Vol. 10.
103. Zhu, Z.; Rui, G.; Li, Q.; Allahyarov, E.; Li, R.; Soulestin, T.; Domingues Dos Santos, F.; He, H.; Taylor, P. L.; Zhu, L. Electrostriction-Enhanced Giant Piezoelectricity via Relaxor-like Secondary Crystals in Extended-Chain Ferroelectric Polymers. *Matter* 2021, 4 (11), 3696–3709. <https://doi.org/10.1016/j.matt.2021.09.008>.
104. Li, S.; Bjormander, C.; Cao, W.; Cross, L. E. *Magnetic Recording Heads View Project in Situ Oxide Growth by Radio Frequency-Magnetron Sputtering View Project The Extrinsic Nature of Nonlinear Behavior Observed in Lead Zirconate Titanate Ferroelectric Ceramic*. <http://ojps.aip.org/japo/japcr.jsp>.
105. Jin, L.; Li, F.; Zhang, S. Decoding the Fingerprint of Ferroelectric Loops: Comprehension of the Material Properties and Structures. *Journal of the American Ceramic Society* 2014, 97 (1), 1–27. <https://doi.org/10.1111/jace.12773>.
106. Liu, Y.; Wang, Q. Ferroelectric Polymers Exhibiting Negative Longitudinal Piezoelectric Coefficient: Progress and Prospects. *Advanced Science*. John Wiley and Sons Inc. March 1, 2020. <https://doi.org/10.1002/advs.201902468>.

107. Lheritier, P. *Study of PVDF Derivatives for Actuation Purpose*. <https://theses.hal.science/tel-02963638>.
108. Ullah, A.; Ur Rahman, A.; Won Ahn, C.; Rahman, M. U.; Ullah, A.; Rehman, Z. U.; Javid Iqbal, M.; Kim, I. W. Enhancement of Dielectric and Energy Density Properties in the PVDF-Based Copolymer/Terpolymer Blends. *Polym Eng Sci* 2015, 55 (6), 1396–1402. <https://doi.org/10.1002/pen.24083>.
109. Gong, H.; Wang, X.; Sun, M.; Zhang, Y.; Ji, Q.; Zhang, Z. Tuning the Ferroelectric Phase Transition of P(VDF-TrFE) through a Simple Approach of Modification by Introducing Double Bonds. *ACS Omega* 2022, 7 (47), 42949–42959. <https://doi.org/10.1021/acsomega.2c05172>.
110. Zhou, X.; Sun, Q.; Xiao, Z.; Luo, H.; Zhang, D. Three-Dimensional BNT/PVDF Composite Foam with a Hierarchical Pore Structure for Efficient Piezo-Photocatalysis. *J Environ Chem Eng* 2022, 10 (5). <https://doi.org/10.1016/j.jece.2022.108399>.
111. Liu, Y. L.; Wu, J. M. Synergistically Catalytic Activities of BiFeO<sub>3</sub>/TiO<sub>2</sub> Core-Shell Nanocomposites for Degradation of Organic Dye Molecule through Piezophototronic Effect. *Nano Energy* 2019, 56, 74–81. <https://doi.org/10.1016/j.nanoen.2018.11.028>.
112. Ma, J.; Ren, J.; Jia, Y.; Wu, Z.; Chen, L.; Haugen, N. O.; Huang, H.; Liu, Y. High Efficiency Bi-Harvesting Light/Vibration Energy Using Piezoelectric Zinc Oxide Nanorods for Dye Decomposition. *Nano Energy* 2019, 62, 376–383. <https://doi.org/10.1016/j.nanoen.2019.05.058>.
113. Wu, W.; Yin, X.; Dai, B.; Kou, J.; Ni, Y.; Lu, C. Water Flow Driven Piezo-Photocatalytic Flexible Films: Bi-Piezoelectric Integration of ZnO Nanorods and PVDF. *Appl Surf Sci* 2020, 517. <https://doi.org/10.1016/j.apsusc.2020.146119>.
114. Lan, S.; Feng, J.; Xiong, Y.; Tian, S.; Liu, S.; Kong, L. *Performance and Mechanism of Piezo-Catalytic Degradation of 4-Chlorophenol: Finding of Effective Piezo-Dechlorination*; 2017. <http://pubs.acs.org>.

115. Amdouni, W.; Fricaudet, M.; Otoničar, M.; Garcia, V.; Fusil, S.; Kreisel, J.; Maghraoui-Meherzi, H.; Dkhil, B. BiFeO<sub>3</sub> Nanoparticles: The “Holy-Grail” of Piezo-Photo-Catalysts? *Advanced Materials* 2023. <https://doi.org/10.1002/adma.202301841>.
116. Bößl, F.; Menzel, V. C.; Jeronimo, K.; Arora, A.; Zhang, Y.; Comyn, T. P.; Cowin, P.; Kirk, C.; Robertson, N.; Tudela, I. Importance of Energy Band Theory and Screening Charge Effect in Piezo-Electrocatalytical Processes. *Electrochim Acta* 2023, 462. <https://doi.org/10.1016/j.electacta.2023.142730>.